

Disturbed, diffuse, or just missing?

A global study of the H I content of Hickson compact groups

M. G. Jones^{1,2,*}, L. Verdes-Montenegro¹, J. Moldon¹, A. Damas Segovia^{1,3}, S. Borthakur⁴, S. Luna^{1,5}, M. Yun⁶,
A. del Olmo¹, J. Perea¹, J. Cannon⁷, D. Lopez Gutierrez^{7,8}, M. Cluver^{9,10}, J. Garrido¹, and S. Sanchez¹

¹ Instituto de Astrofísica de Andalucía (CSIC), Glorieta de la Astronomía, 18008 Granada, Spain

² Steward Observatory, University of Arizona, 933 North Cherry Avenue, Rm. N204, Tucson, AZ 85721-0065, USA

³ Max-Planck-Institut für Radioastronomie, Auf dem Hügel 69, D-53121 Bonn, Germany

⁴ School of Earth and Space Exploration, Arizona State University, 781 Terrace Mall, Tempe, AZ 85287, USA

⁵ EGI Foundation, Science Park 140, 1098 XG Amsterdam, Netherlands

⁶ Astronomy Department, University of Massachusetts, Amherst, MA 01003, USA

⁷ Department of Physics & Astronomy, Macalester College, 1600 Grand Avenue, Saint Paul, MN 55105, USA

⁸ Physics Department, Harvard University, 17 Oxford Street, Cambridge, MA 02138, USA

⁹ Centre for Astrophysics and Supercomputing, Swinburne University of Technology, John Street, Hawthorn 3122, Victoria, Australia

¹⁰ Department of Physics and Astronomy, University of the Western Cape, Robert Sobukwe Road, Bellville, South Africa

December 8, 2022

ABSTRACT

Context. Hickson compact groups (HCGs) are dense configurations of four to ten galaxies, whose H I morphology appears to follow an evolutionary sequence of three phases, with gas initially confined to galaxies, then significant amounts spread throughout the intra-group medium, and finally with almost no gas remaining in the galaxies themselves. It has also been suggested that several groups may harbour a diffuse H I component that is resolved out by interferometric observations.

Aims. The H I deficiency of HCGs is expected to increase as the H I morphological phase progresses along the evolutionary sequence. If this is the case, H I deficiency would be a rough proxy for the age and evolutionary state of a HCG. We aim to test this hypothesis for the first time using a large sample of HCGs and to investigate the evidence for diffuse H I in HCGs.

Methods. We performed a uniform reduction of all publicly available VLA H I observations (38 HCGs) with a purpose-built pipeline that also maximises the reproducibility of this study. The resulting H I data cubes were then analysed with the latest software tools to perform a manual separation of emission features into those belonging to galaxies and those extending into the intra-group medium. We thereby classified the H I morphological phase of each group as well as quantified their H I deficiency compared to galaxies in isolation.

Results. We find little evidence that H I deficiency can be used as a proxy for the evolutionary phase of a compact group in either of the first two phases, with the distribution of H I deficiency being consistent in both. However, for the final phase, the distribution clearly shifts to high H I deficiencies, with more than 90% of the expected H I content typically missing. Across all HCGs studied, we identify a few cases where there is strong evidence for a diffuse gas component in the intra-group medium, which might be detectable with improved observations. We also classify a new sub-phase where groups contain a lone H I-bearing galaxy, but are otherwise devoid of gas.

Conclusions. The new morphological phase we have identified is likely the result of an evolved, gas-poor group acquiring a new, gas-rich member. The large spread of H I deficiencies in the first two morphological phases suggests that there is a broad range of initial H I content in HCGs, which is perhaps influenced by large-scale environment, and that the timescale for morphological changes is, in general, considerably shorter than the timescale for the destruction or consumption of neutral gas in these systems.

Key words. Galaxies: evolution, Galaxies: groups, Galaxies: interactions, Galaxies: ISM, Radio lines: ISM

1. Introduction

Hickson (1982) catalogued 100 groups of four to ten members packed in extremely dense configurations, but located in relatively low density environments on a larger scale, which are commonly referred to as Hickson compact groups (HCGs). The high number density of HCGs is coupled with their relatively low velocity dispersions (Hickson et al. 1992). Together, this make them ideal sites for strong, frequent galaxy–galaxy interactions. These interactions are visible through a myriad of neu-

tral gas (H I) tails, bridges, and clumps (e.g. Verdes-Montenegro et al. 1997; Sulentic et al. 2001; Verdes-Montenegro et al. 2005a; Serra et al. 2013; Konstantopoulos et al. 2013; Jones et al. 2019), as well as line emission from shocks (Rich et al. 2010; Vogt et al. 2013; Cluver et al. 2013; Duarte Puertas et al. 2019), apparent rapid morphological transformations (Tzanavaris et al. 2010; Plauchu-Frayn et al. 2012; Alatalo et al. 2015; Eigenthaler et al. 2015; Zucker et al. 2016; Lisenfeld et al. 2017), and in some cases the presence of a diffuse hot intra-group medium (IGrM, Belsole et al. 2003; Desjardins et al. 2013; O’Sullivan et al. 2014).

* jonesmg@arizona.edu

Early single dish studies of HCGs revealed them to be deficient in H I gas (Williams & Rood 1987; Huchtmeier 1997), while the first interferometric maps began to reveal the complex morphologies of HCGs in neutral gas (Williams et al. 1991, 2002; Williams & van Gorkom 1995). These findings led Verdes-Montenegro et al. (2001) to pose the question: where is the neutral gas in HCGs? This seminal study of 72 HCGs observed with single dish telescopes confirmed and expanded on the initial findings that HCGs were H I-deficient. A subset (16 HCGs) of the sample was followed up with Very Large Array (VLA) observations, allowing for the spatial distribution and kinematics of the gas to be studied in detail. Based on this imaging of 16 groups, Verdes-Montenegro et al. (2001) proposed an evolutionary sequence for HCGs, with their phase assigned based on their H I morphology. In Phase 1 of the sequence, H I emission is predominantly confined to the discs of the galaxies in the group. In Phase 2 significant tidal features become evident and a significant fraction of the observed H I is seen outside of galaxies. Finally, in Phase 3 almost all the gas has been removed from the galaxies or is simply undetected.¹

If this morphological sequence tracks the evolution of a HCG, then it would be expected that the H I deficiency of the group would also generally increase with increasing morphological phase as gas (both atomic and molecular) is consumed or ionised and galaxies transform to earlier morphological types (Cluver et al. 2013; Lisenfeld et al. 2017). However, the validity of this proxy has never been verified for a larger sample of HCGs beyond the original sample used to formulate the proposed sequence. We note that although H I content is merely one aspect of these extremely complex systems, a viable proxy of evolutionary state based solely on total H I content, even if only approximate, would be a valuable tool for categorising compact groups identified in future surveys regardless of whether or not they are resolved in H I.

Borthakur et al. (2010) expanded on the work of Verdes-Montenegro et al. (2001) by following up on 22 HCGs with deep H I observations with the Green Bank Telescope (GBT). These observations recovered more flux than the previous VLA observations, somewhat reducing the estimated H I deficiency of certain groups. However, more important was the distribution of this additional gas, which in some cases suggested the existence of a diffuse H I component, spread over up to 1000 km s^{-1} and not recovered by the interferometer. Borthakur et al. (2015) performed GBT H I mapping for four HCGs with the richest IGrM content, revealing that the additional gas mostly traces the higher column density features mapped with the VLA, suggesting that its origin is also largely tidal.

In this work we return to the evolutionary sequence proposed by Verdes-Montenegro et al. (2001) in order to test the long-standing assumption that the H I evolutionary phase of HCGs is a proxy for their H I deficiency, and vice versa. To do this we have compiled all publicly available VLA H I observations of HCGs, 38 groups in total. These were reduced in as uniform a manner as possible, allowing revised H I deficiency measurements of 38 groups, and the H I morphological classification of 32. With this dataset we address the question of where the gas in HCGs has gone and discuss the pathways along which these groups likely evolve.

¹ The sequence of Verdes-Montenegro et al. (2001) originally included a Phase 3b for galaxies evolving within a common H I cloud. However, there are no longer any convincing example of this proposed phenomenon (e.g. Verdes-Montenegro et al. 2002), with the possible exception of HCG 49, and we do not consider this a valid separate phase.

In the following section we outline how these data were compiled and reduced. In Section 3 we discuss how H I features were manually separated in each group and present moment maps and spectra of all groups. In Section 4 we present our results, and comparisons to previous works. Finally, in Section 5 we discuss our revised H I morphological classification scheme, before presenting our conclusions in Section 6. In addition to scientific analysis of these data, the entire process from acquisition of the raw data, through their reduction and analysis, has been performed with the utmost attention paid to reproducibility and open science. Our efforts in this direction are discussed in detail in Appendix B.

2. Data compilation and reduction

The interferometric data used in this work were compiled using the (J)VLA² data archive and were originally observed as part of the projects AB651, AG645, AK580, AM559, AR251, AV206, AV221, AV227, AV230, AV275, AV285, AW234, AW272, AW351, AW500, AW568, AW601, AY155, AY160, AY86, AZ125, MYUN, and 13A-387. Together these projects observed 38 of the original 100 HCGs (HCG 2, 7, 10, 15, 16, 19, 22, 23, 25, 26, 30, 31, 33, 37, 38, 40, 47, 48, 49, 54, 56, 57, 58, 59, 61, 62, 68, 71, 79, 88, 90, 91, 92, 93, 95, 96, 97, 100) from Hickson (1982) in the H I line. The full list of target groups and a summary of their VLA observations are shown in Table 1.

The key goals of our methodology here is to create a data reduction process that is as uniform as possible across all these heterogeneous data sets and to make it as reproducible as possible (see Appendix B). To this end we developed a pipeline for the reduction of historical VLA H I data (but can also be used for JVLA data), which makes up the majority of the data for HCGs. In the following paragraphs we provide an overview of this pipeline. The code can be found on [github](https://github.com)³.

2.1. Pipeline and reduction overview

The majority of the VLA data was observed with channel resolutions of approximately 49 or 98 kHz, corresponding to velocity resolutions of about 10 and 20 km s^{-1} , respectively. The JVLA project (13A-387) used a channel resolution of 7.8 kHz ($\sim 1.6 \text{ km s}^{-1}$), however, we chose to average these data over three channels to expedite the reduction process and to make them more directly equivalent to the VLA data, without degrading their velocity resolution beyond $\sim 5 \text{ km s}^{-1}$.

Our data reduction pipeline is based in CASA (Common Astronomy Software Applications, v5.4, McMullin et al. 2007) and Python and is designed specifically to reduce H I spectral line data, particularly for historical VLA data sets. It provides a consistent and uniform data calibration, but allows manually tuned parameters to be adapted when needed. These are input as a parameters file with separate parameters for each section of the reduction process. The pipeline is designed so that each step can be run individually or the full pipeline run end-to-end (for a given set of observations). There is also an interactive mode where the pipeline will pause and query the user for any missing parameters rather than failing. The pipeline has been encoded using CGAT-core (Cribbs et al. 2019) workflow management system, which allows defining the dependencies between

² We note that in this work we endeavour to use ‘VLA’ to refer to historical data from the Very Large Array and ‘JVLA’ for data from the upgraded Karl G. Jansky Very Large Array.

³ https://github.com/AMIGA-IAA/hcg_hi_pipeline

Table 1. HCG H I sample

HCG	N_{mem}	RA deg	Dec deg	cz_{\odot} km s^{-1}	Dist. Mpc	VLA Config.	Δv_{chan} km s^{-1}	σ_{rms} mJy beam^{-1}	Beam Size arcsec	$N_{\text{HI}} (4\sigma)$ cm^{-2}
2	3	7.87517	8.43126	4326	50	D	10.3	0.74	69.3×51.4	1.9×10^{19}
7	4	9.84960	0.87818	4224	50	C,D	20.6	0.3	35.0×28.0	4.0×10^{19}
10	4	21.53076	34.69095	4761	50	DnC	20.6	0.39	61.6×49.7	1.7×10^{19}
15	6	31.91244	2.13827	7042	96	DnC	20.6	0.48	60.7×47.5	2.2×10^{19}
16	5	32.38881	-10.16298	3977	49	C,D	20.6	0.41	38.9×31.7	4.3×10^{19}
19	3	40.68807	-12.41181	4253	53	C,D	10.3	0.47	41.0×27.0	3.9×10^{19}
22	4	45.88027	-15.67570	2626	37	CnB,D	20.6	0.56	50.9×36.8	3.9×10^{19}
23	5	46.77701	-9.58547	4921	65	C	20.6	0.54	25.3×20.0	13.9×10^{19}
25	4	50.18220	-1.05192	6343	82	DnC	20.6	0.5	65.4×56.6	1.7×10^{19}
26	7	50.47584	-13.64586	9618	130	C	10.3	0.63	25.5×16.8	13.5×10^{19}
30	4	69.11918	-2.83239	4645	61	DnC	20.6	0.51	57.9×44.8	2.6×10^{19}
31	5	75.40372	-4.25671	4068	53	CnB	10.3	0.65	14.6×12.1	33.6×10^{19}
33	4	77.69969	18.03465	7795	107	C	20.6	0.82	17.5×15.4	39.4×10^{19}
37	5	138.39859	30.01417	6741	97	DnC	20.6	0.74	49.5×47.4	4.1×10^{19}
38	3	141.91194	12.28081	8652	123	D	4.9	1.24	85.6×57.6	1.6×10^{19}
40	5	144.72717	-4.85196	6628	99	DnC	20.6	0.33	58.8×44.8	1.6×10^{19}
47	4	156.45175	13.73157	9508	136	C,D	4.9	0.49	31.0×20.0	5.0×10^{19}
48	2	159.44020	-27.08746	2352	34	DnC	20.6	0.78	54.3×37.4	5.0×10^{19}
49	5	164.15204	67.17920	9939	139	DnC	10.3	0.4	47.4×37.1	2.1×10^{19}
54	5*	172.31364	20.57852	1412	27	C	10.3	0.46	20.8×16.9	11.9×10^{19}
56	5	173.13297	52.94860	8110	116	C,D	4.9	0.49	23.5×19.6	6.8×10^{19}
57	8	174.46054	21.98504	9032	135	C	4.9	0.62	23.7×18.9	8.8×10^{19}
58	5	175.54908	10.31703	6138	85	DnC,D	20.6	0.25	65.8×57.0	0.9×10^{19}
59	4	177.10671	12.72623	4008	60	C,D	4.9	0.63	24.0×16.0	10.4×10^{19}
61	3	183.09972	29.17781	3956	60	C	4.9	0.35	26.2×18.8	4.6×10^{19}
62	4	193.28399	-9.22410	4239	60	C	4.9	0.62	24.8×14.9	10.8×10^{19}
68	5	208.42036	40.32794	2401	35	D	10.3	0.68	58.3×54.8	2.0×10^{19}
71	5	212.76906	25.48492	9199	131	C,D	4.9	0.44	26.0×20.0	5.4×10^{19}
79	4	239.80365	20.75163	4369	59	C	10.3	0.5	20.8×17.4	12.5×10^{19}
88	4	313.09503	-5.75790	6032	74	C	20.6	0.3	22.6×17.2	10.1×10^{19}
90	4	330.52343	-31.96680	2635	33	DnC	41.2	0.55	49.1×39.9	5.1×10^{19}
91	4	332.30172	-27.77593	7195	92	DnC	20.6	0.66	51.3×47.0	3.5×10^{19}
92	4	339.00215	33.96577	6614	87	B,C,D	20.6	0.06	15.0×15.0	3.7×10^{19}
93	4	348.85099	18.98311	5136	64	DnC	20.6	0.4	59.7×53.3	1.6×10^{19}
95	4	349.88240	9.49185	11615	153	CnB	20.6	0.32	21.4×19.3	10.1×10^{19}
96	4	351.99291	8.77408	8725	116	C	20.6	0.21	26.9×18.3	5.4×10^{19}
97	5	356.86224	-2.30542	6579	85	DnC	20.6	0.44	63.2×49.5	1.8×10^{19}
100	5	0.33654	13.13256	5461	67	DnC	20.6	0.47	58.7×50.5	2.1×10^{19}

Notes. Columns: (1) HCG ID number, (2) number of group members considered in this work, (3 & 4) group coordinates (J2000), (5) heliocentric radial velocity (re-calculated as the mean velocity of the group members), (6) group distance calculated via the Cosmicflows-3 model (Tully et al. 2016; Kourkchi et al. 2020), which have uncertainties of ~ 3 Mpc, (7) VLA configurations the target group was observed with, (8) channel width, (9) rms noise, (10) synthesised beam size, (11) 4σ column density sensitivity (over 20 km s^{-1}).

* The five ‘members’ of HCG 54 are now thought to be clumps all associated with a single merging system.

the pipeline steps by using Python decorators. If previous steps or parameters are altered then the pipeline will know that it must re-run these steps before subsequent steps can be executed. The pipeline also performs automatic logging, recording every command that CASA executes, flagging errors automatically and halting the workflow when it is required. Subsequent steps cannot be executed without the successful completion of the prerequisite steps in the pipeline.

The reduction pipeline begins by reading in the data and applying any manual flags that the user has defined in a separate file. It then proceeds with standard flagging procedures, which were typically to remove antennae with more than 5.0 m of shad-

owing, and to remove the first 5 s of each scan (although in general these value can be modified in the pipeline parameters file). The CASA algorithm `tfcrop` is then typically run on all target fields, for example science targets and all calibrators. Again this can be, and was in a few cases, disabled in the parameters file. The pipeline then queries the user to identify the purpose of each target field (i.e. the science target, and the flux, band-pass and phase calibrators), which are not stored in the metadata of historical VLA observations. The pipeline can then proceed with standard calibration steps to calibrate the gains, phases, and absolute flux scale.

After the first round of calibration the `rflag` algorithm is run to remove any remaining radio frequency interference (RFI). Although caution is advised when using this algorithm on spectral line data, typically for H I observations the line is sufficiently weak that it is not apparent in the visibilities data, and this is not a concern. However, this step was disabled for all the JVLA data as the RFI required careful manual removal in many of these observations, as well as for a selection of the VLA data. If `rflag` is run then the pipeline repeats a second round of calibration, if not then it proceeds to split the data and perform continuum subtraction. When the science targets are split from the rest of the data the pipeline automatically identifies overlapping spectral windows and merges them together (this option can be disabled).

Before proceeding with the continuum subtraction the pipeline queries the user to define a line-free range of channels. Single dish spectra in the literature, in particular Borthakur et al. (2010), were used whenever available to identify genuinely emission free channels for each group. In some cases this required a 0th order fit to the continuum because line-free channels only existed on one side of the band as the bandwidths of the historical VLA data were narrow. However, for the JVLA data the bandwidth was sufficiently broad that an identical range of channels could be used in most cases without the risk of impinging on the groups' H I line emission. Once the line-free channel range was defined for each group the `uvcontsub` algorithm was used to subtract the continuum. In most cases a 1st order fit was used, however, in several of the VLA data sets only a 0th order fit can be made as very few of the channels are free from line emission, or the observation is made up of two separate spectral windows that only overlap where there is line emission. Using a 0th order fit often leads to minor continuum artefacts in the final cubes, which then must be manually excluded when generating the source masks and moment maps.

The final step of the CASA pipeline is to image data and generate the final cubes. The pipeline images the data from each project and target separately using the `tclean` task in CASA. In most cases automatic masking and multi-scale clean were used. However, in a few cases the sidelobes of the synthesised beam were not sufficiently suppressed for multi-scale clean to be used, while in a few other cases using a simple primary beam mask gave better results than automated masking. Typically the data were cleaned down to a threshold of 2.5σ within the mask. In most cases the Briggs' robust parameter was set to 2.0 in order to maximise the recovery of extended emission, at the expense of some angular resolution. This choice of weighting is likely non-optimal for many other science cases, but the robust parameter can be changed in the pipeline parameters files and the reduction repeated with a single command. In cases where a single target was observed in multiple projects a secondary script was used to combine the observations before following the same approach for the final imaging. The pipeline also generates simple moment zero maps using a simple threshold. However, these are only intended for quality control purposes and are not used in our analysis. There is also a "cleanup" function which can automatically remove unwanted files after execution in order to save disk space.

All the parameters files to re-execute or modify the steps of the pipeline on another machine, starting with the raw data from the VLA archive, are publicly available through Zenodo⁴. In addition, the final image cubes and moment zero maps are stored there.

2.2. Source masking

All source masking was performed using the SoFiA package (Serra et al. 2014, 2015). All SoFiA parameters files for each group are provided in the repository associated with this paper, which can be referred to for the exact details of the masking of any individual group. However, in general we used the smooth and clip algorithm within SoFiA with Gaussian smoothing kernels of approximately 0.5, 1.0, and 2.0 times the beam diameter. This was combined with boxcar smoothing in the spectral direction, but the number of channels smoothed over depended on the original resolution of the data. The historical VLA data with a resolution of $\sim 10 \text{ km s}^{-1}$ was smoothed over zero, two, and three channels, whereas the data with $\sim 20 \text{ km s}^{-1}$ resolution was only smoothed over zero and two channels. The newer, much higher spectral resolution, JVLA data were smoothed over zero, four, and six channels (roughly corresponding to 5.0, 20, and 30 km s^{-1} , after the initial three-channel averaging already performed). When constructing the masks typically a signal-to-noise ratio (S/N) threshold of 4.0 was used and a source reliability of over 95% was enforced. Sources within half a beam width and within two or three channels (six channels for the JVLA data) were merged and then the masks dilated to recover as much extended flux as possible. In some cases it was necessary to manually exclude certain regions of the cube to avoid residual continuum artefacts being falsely identified as sources.

The rationale behind this approach to source masking was not to separate out different features at this stage, indeed it is preferable to blend them into single SoFiA sources to recover as much extended flux as possible. The separation of features, described in Section 3, was performed after the mask generation using `SlicerAstro` (Punzo et al. 2016).

2.3. Distance estimates and uncertainties

Distances to all groups were calculated from their radial velocities and the flow model⁵ of the Cosmicflows-3 project (Graziani et al. 2019; Kourkchi et al. 2020). Although Kourkchi et al. (2020) do not provide uncertainty estimates for as part of the distance calculator, an approximate estimate can be made by assuming a typical peculiar velocity (not associated with large scale motions) of around 200 km s^{-1} . For a Hubble constant of $70 \text{ km s}^{-1} \text{ Mpc}^{-1}$, this equates to a minimum distance uncertainty of $\sim 3 \text{ Mpc}$. The distance estimates given in Table 1 should be considered accurate to approximately this level.

Generally the velocity of each group member was taken from Hickson et al. (1992) and the median velocity of the groups re-calculated after new members were added and false members removed. However, upon inspection of the H I emission in HCGs it became apparent that the published redshifts in Hickson et al. (1992) were erroneous for a number of galaxies. In these cases we adopted the redshift value given in the NASA/IPAC Extragalactic Database (NED). The galaxies that we identified with erroneous redshifts were: HCGs 19c, 22c, 48a, 48b, 57h, 71c, 91a, 95d, and 100d. After updating these redshifts we re-calculated the median redshift of each group and updated our distance estimate accordingly.

3. Separation of features

For each group with sources detected in the VLA observations we attempted to separate features into three broad classes: those

⁴ <https://doi.org/10.5281/zenodo.6366659>

⁵ <http://edd.ifa.hawaii.edu/CF3calculator/>

associated with and likely bound to a group member galaxy, extended features likely not bound to any galaxy, and finally galaxies and features outside the core group. The separation of features associated with galaxies from extended features is usually not a straightforward process in HCGs, and consideration of the full 3-dimensional spatial and kinematic information is often required. For example, HCG 92 contains a large tidal feature that overlaps (in projection) with multiple member galaxies, but is in fact not associated with any of them (Williams et al. 2002).

Each H I cube was displayed with the 2D and 3D visualisation tools in *SlicerAstro* and the *SoFiA* source mask was manually segmented into separate features. In cases with well resolved galaxies (spatially and in velocity) detected at high S/N, this process is quite robust as regions of emission that strongly deviate from the kinematic structure of each galaxy can be readily identified and excised. However, in many cases sources are marginally resolved, blended, and/or detected at low S/N. Wherever possible we attempt to perform this separation, but we note that in these cases the process can become quite subjective. However, as the purpose of this separation is to be able to broadly classify HCGs based on their H I morphology, a certain level of uncertainty and subjectivity can be tolerated.

There is also the issue that some HCGs originally had false members, which have since been excluded (making some groups triplets). Triplets are included in our analysis, but are distinguished from $N \geq 4$ groups wherever possible. Other groups have new members which were too low surface brightness (LSB) to be included in the original catalogue or were too separated from the other members (with no apparent connection in optical images), but are clearly connected in H I. The goal of this work is not to re-define or refine the HCG catalogue, hence we take the following simple approach: potential new members which are separated from the core (original) groups by more than ~ 100 kpc will not be included as new members, unless they have a definite connection in H I, indicating that they have already begun interacting with the core group. We note that in some cases such galaxies may be within (or entering for the first time) the DM halo of the CG, however, in this work we are seeking to characterise the H I morphology, content, and evolution of the core group members and therefore these peripheral members are tangential to our goals unless they have already begun interactions with the core group. Within the core of each group, galaxy-galaxy projected separations (for nearest neighbours) are almost always less than 100 kpc. Hence this represents a reasonable cut-off separation for considering new members.

A galaxy must contain H I for it to be detected in our observations, which clearly leads to some form of bias, as gas-poor galaxies in a similar configuration may not be considered members where gas-rich ones would be, in the absence of a uniform, deep, and highly complete redshift survey covering all HCGs, the introduction of such biases on some level is unavoidable. We have thus favoured clarity and simplicity over attempting to re-define these compact groups, for which frequently there would be insufficient data.

In the following subsections we show a contour map of H I emission (moment 0) overlaid on an optical image (from DECaLS, SDSS, or POSS) for each group. We favour DECaLS (Dey et al. 2019) images wherever they exist, as these are the deepest of the three, followed by SDSS (York et al. 2000) and POSS (Reid et al. 1991). We use the r -band (R-band for POSS) images obtained directly from the public image cutout services of each survey. In cases where we were able to separate features, the group member galaxies are shown in blue contours, extended features are shown in green, and non-members are shown in red.

For cases where it was not possible to separate features, the moment zero map is shown with multi-coloured contours, starting at 4σ (black) and each subsequent contour being twice the previous one. Dashed black contours indicate -4σ .

In addition, a spectrum is shown for each group. This spectrum includes all emission within the *SoFiA* source mask, including non-members and features. Note that in some cases this includes emission well beyond the region shown in the optical images of each group. Where it exists a GBT spectrum (Borthakur et al. 2010) is overlaid on the VLA spectrum, along with a weighted version of the VLA spectrum that accounts for the response of the GBT beam (and any difference in the pointing centres). We model the GBT beam as a circular 2D Gaussian with a HPBW of $9.1''$. The primary beam-corrected VLA data are weighted (in the image plane) with a Gaussian with a width such that its convolution with the VLA synthesised beam (assumed to be circular, with a width equal to the average of the major and minor axes), gives a Gaussian of HPBW $9.1''$. This thereby approximately accounts for the beam response of the GBT observations, which in cases where there is emission near the edge (or beyond) the GBT primary beam can be essential to making a fair comparison. Finally, the moment one (velocity field) contour maps overlaid on the optical images of each group (with detected H I emission) are shown in Appendix D.

3.1. HCG 2

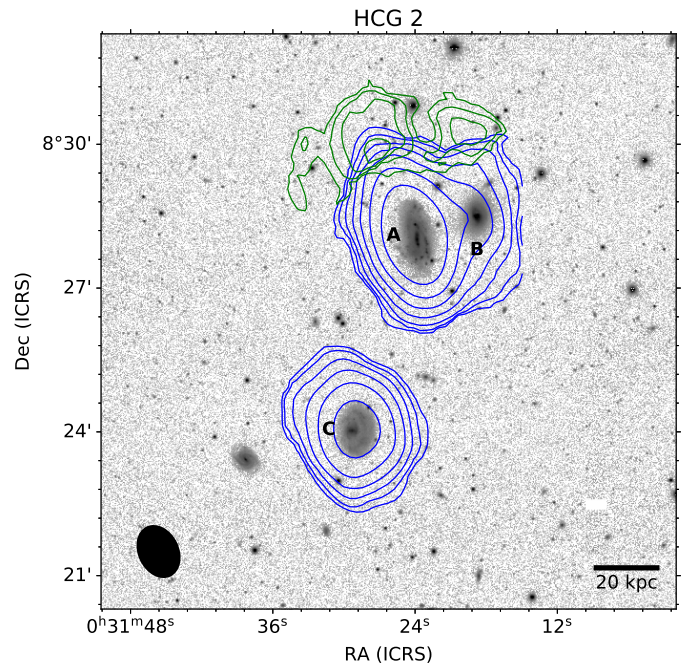


Fig. 1. Integrated H I emission (moment 0) contours overlaid on a DECaLS r -band image. HCG members are shown with blue contours, extended features in green, and non-member galaxies in red (none in this panel). The VLA synthesised beam is shown in the bottom left as a solid black ellipse and a scale bar indicating 20 kpc is in the lower right. The contours start at 4σ (over 20 km s^{-1}) and each subsequent contour is double the one before it. The minimum contour level is listed for each group in Table 1.

HCG 2 is a triplet (HCG 2d is a background object) of late-type galaxies at approximately 4300 km s^{-1} (Figure 1). The global moment map and velocity field of the group clearly shows that HCG 2a and c are strongly detected. HCG 2c shows min-

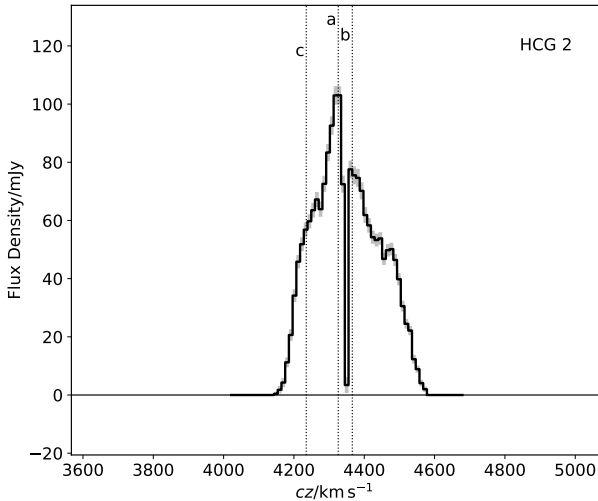


Fig. 2. VLA spectrum of all detected H I emission (solid black line) within the primary beam. The light grey shading around the black line indicates the uncertainty based on the rms noise and the number of pixels included in the source mask for a given channel. The vertical dotted lines indicate the velocities of group member galaxies. Regions of the spectrum where all values are exactly zero indicate spectral ranges where there are no pixels in the source mask.

imal signs of disturbance other than the misalignment of its iso-velocity contours with its minor axis, suggesting a probable warp. HCG 2a on the other hand is blended with emission that appears to be from HCG 2b, as it is co-spatial with the optical source and has a separate velocity structure (though is scarcely larger than a single beam) that occurs at the expected redshift. We therefore attribute this emission to HCG 2b as best as possible. There is a small, faint extension to the north of HCG 2a which we designate as an extended feature as it does not conform to the velocity structure of either HCG 2a or b. Finally, it should also be noted that one, central channel of the HCG 2 was almost entirely flagged, which will slightly influence the flux measurements of all sources. This channel is clearly visible in the integrated spectrum (Figure 2).

3.2. HCG 7

HCG 7 is a compact configuration of four (three late-type and one lenticular) galaxies at approximately 4200 km s^{-1} . The moment maps indicate that HCG 7a, c, and d are all strongly detected (Figure 3). HCG 7b, the lenticular, does not appear to be detected. HCG 7c is a little separated from the other three group members and has a mostly regular velocity field. The SoFiA mask already separates the emission from HCG 7a and d, so no manual intervention was required. None of the galaxies in the group appear to be strongly disturbed in H I (with caveat that HCG 7b is undetected), and as such no separate extended features were identified. One channel of the cube is entirely flagged, as is apparent in the integrated spectrum (Figure 4).

3.3. HCG 10

HCG 10 is a quartet made up of three tightly packed spirals and one elliptical slightly further afield, all within the range 4600 –

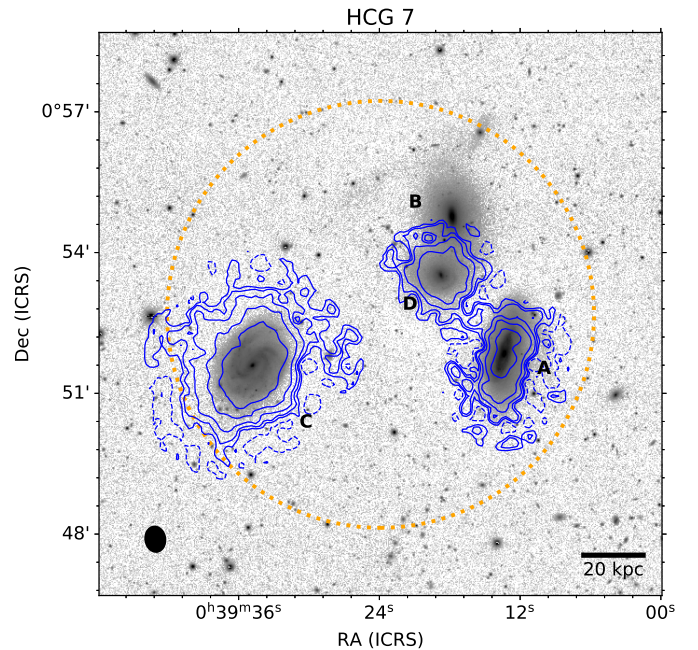


Fig. 3. As in Figure 1. The orange dashed circle indicates the primary beam of the GBT observation of this group.

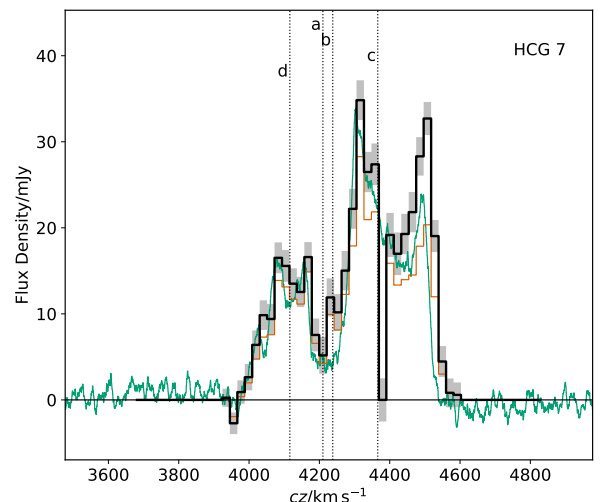


Fig. 4. As in Figure 2. The green (high velocity resolution) spectrum is from the GBT observation of this group (Borthakur et al. 2010), and the orange spectrum is the VLA spectrum weighted to match the GBT primary beam response.

5200 km s^{-1} . Both HCG 10a and d are strongly detected, but no others. In this case the mask generated by SoFiA was not split further at all. It had already identified the two galaxies separately and there is little sign of extended features (Figures 5 & 6), though in the H I cube the western side of HCG 10a appears to be somewhat kinematically disturbed.

3.4. HCG 15

HCG 15 is a collection of six galaxies in a compact, inverted ‘T’ formation. Most members are at $\sim 7000 \text{ km s}^{-1}$, but HCG 15d

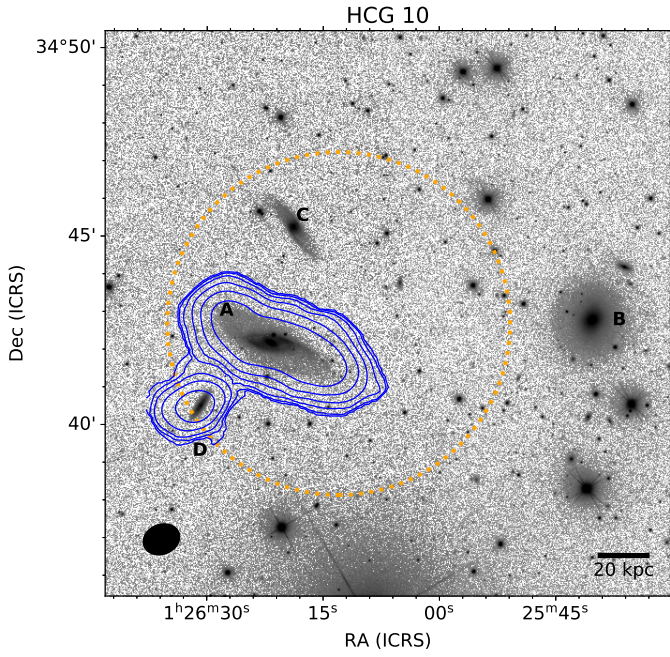


Fig. 5. As in Figure 3.

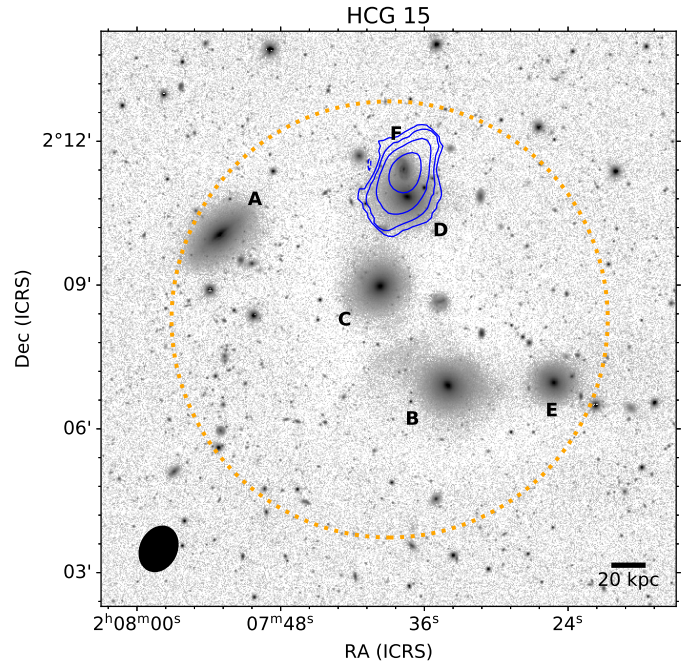


Fig. 7. As in Figure 3.

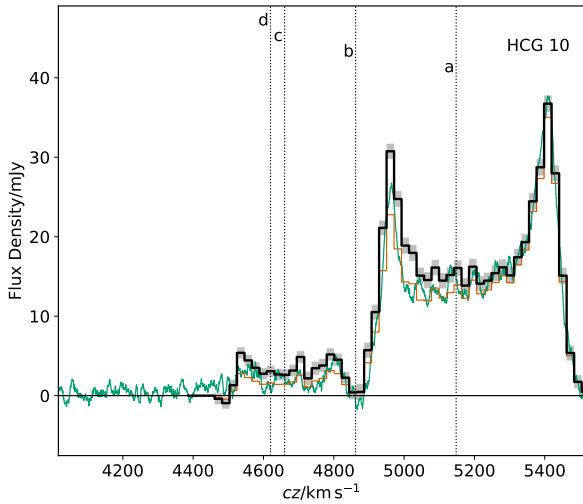


Fig. 6. As in Figure 4.

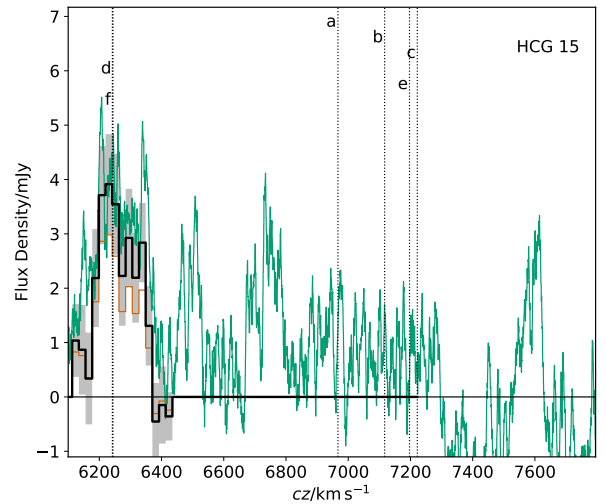


Fig. 8. As in Figure 4.

and f are at $\sim 6200 \text{ km s}^{-1}$. Only HCG 15f is detected in H I, on the very edge of the group. At the (poor) resolution of the data no clear disturbance or extended features could be identified and thus no manual separate was performed (Figures 7 & 8).

3.5. HCG 16

HCG 16 is a compact, linear group of five galaxies at $\sim 4000 \text{ km s}^{-1}$. Jones et al. (2019) performed a detailed study of HCG 16 based on the same archival VLA data. Here we attempt an equivalent separation of features to that study, however, we note that the automated approach to reducing the data that is used here results in slightly more D-array data being flagged relative to C-array than in Jones et al. (2019), which in turn leads to a slightly lower column density sensitivity and slightly finer spa-

tial resolution. In addition, in this work the SoFIA source masks are clipped at 4σ as opposed to 3.5σ in Jones et al. (2019).

All the core members of HCG 16 (a, b, c, and d) are detected as well as NGC 848 and PGC 8210. The former has clearly previously interacted with the core group and is at the head of a $\sim 160 \text{ kpc}$ long tidal tail (Figure 9), while the latter is a dwarf galaxy that has likely never entered the core group before (we do not consider it a group member). The emission from HCG 16a and b are almost blended together, but have been separated as best as possible, there is a high column density H I bridge between HCG 16c and d, as well as numerous tidal features and clumps throughout the group. The integrated H I spectrum of the group for one continuous (in velocity) feature (Figure 10).

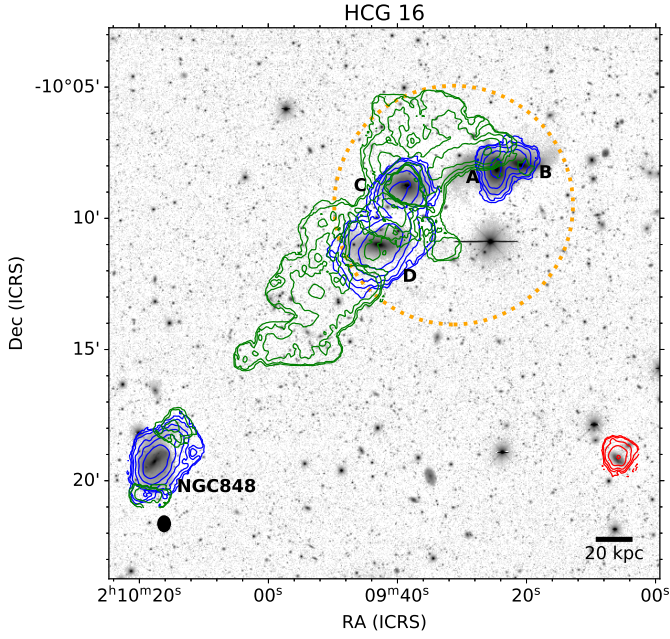


Fig. 9. As in Figure 3.

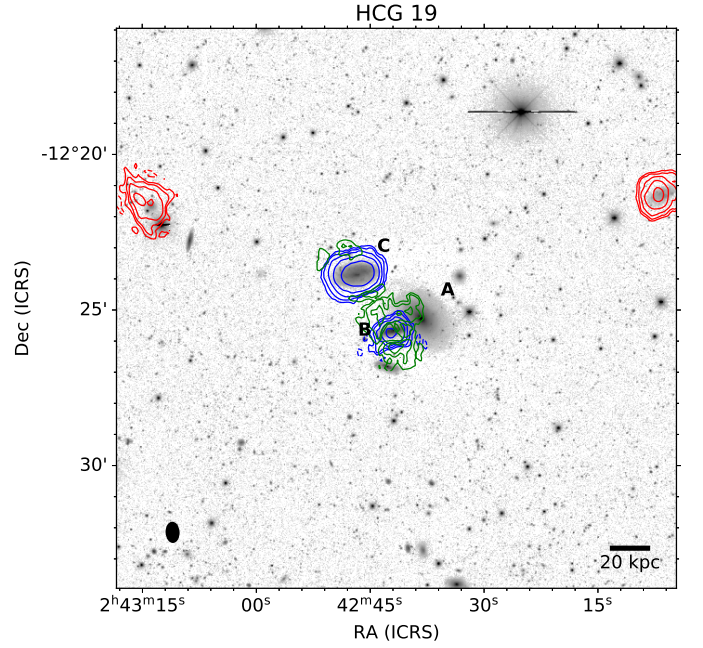


Fig. 11. As in Figure 1.

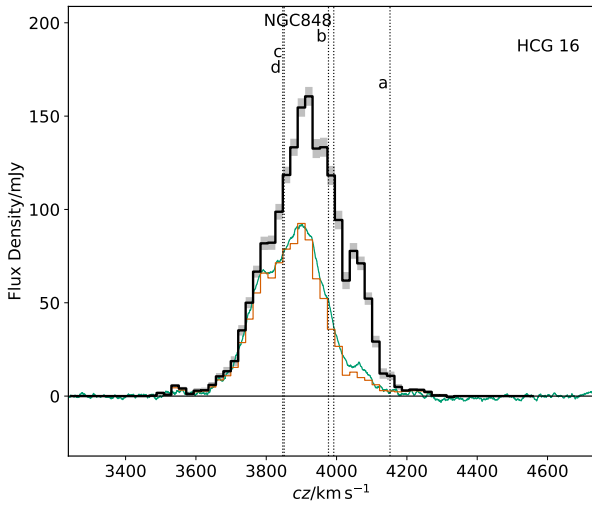


Fig. 10. As in Figure 4.

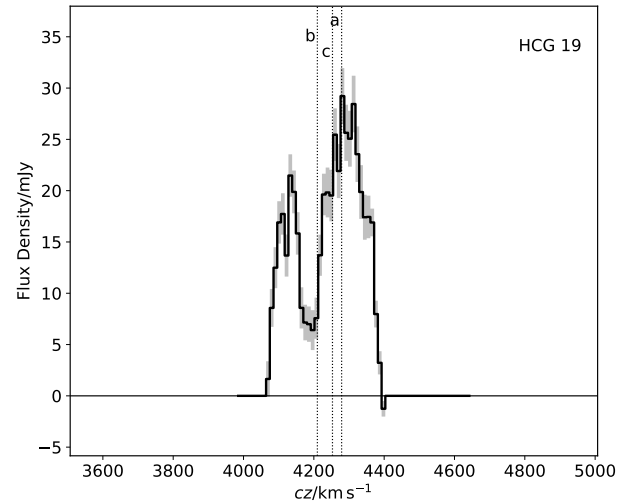


Fig. 12. As in Figure 2.

3.6. HCG 19

HCG 19 is a triplet (HCG 19d is a background object) of two late-type and one early-type galaxies at 4200 km s^{-1} . The SoFiA mask for HCG 19 was generated in a slightly different manner to most other groups owing to a troublesome continuum source artefact to the west of the group. To prevent the artefact from being included in the mask, positivity of sources was enforced, which in turn prevented the use of SoFiA's reliability estimation, and therefore required the threshold level to be raised to 5.5σ (from 4σ) to eliminate spurious sources.

In the core of the group HCG 19b and c are clearly detected, while HCG 19a is not detected. Further afield there are also strong detections of WISEA J024313.79-122138.9 and WISEA J024206.39-122118.3, which are low surface brightness (LSB) galaxies likely falling towards the group for the first time,

but are still separated from the core group by $\sim 100 \text{ kpc}$. We therefore do not include them in our measurement of H I content. For brevity we refer to these as HCG 19W1 and HCG 19W2.

With the exception of HCG 19c, the core galaxies do not appear to be strongly disturbed in H I. However, there are numerous incipient tidal features on the outskirts of the galaxies, including a bridge between HCG 19 a and c. Although there is not much flux in these features and they are difficult to trace due to the poor noise properties of this cube, we have attempted to separate them from the emission of the galactic discs (Figures 11 & 12).

3.7. HCG 22

HCG 22 is an 'S' shaped configuration of four galaxies (two early-types and two late-types) at $\sim 2600 \text{ km s}^{-1}$. Two original

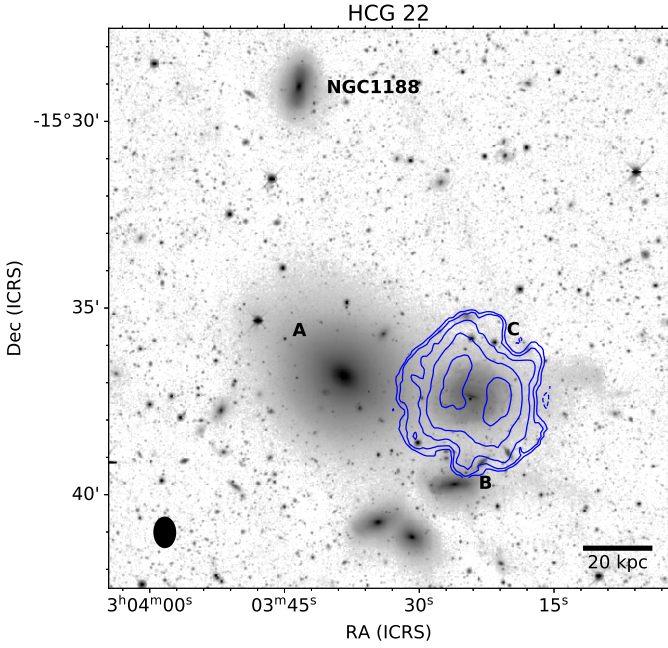


Fig. 13. As in Figure 1.

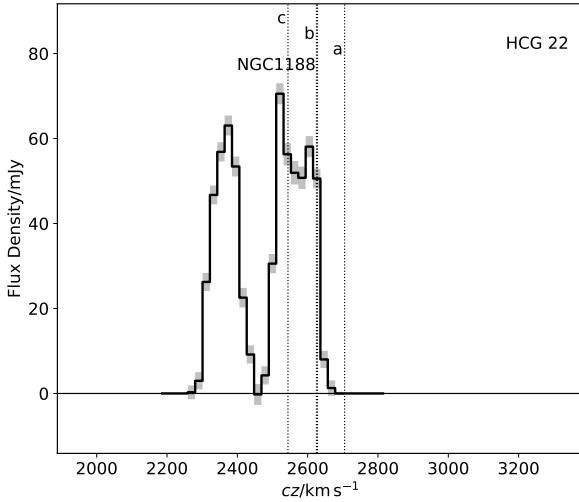


Fig. 14. As in Figure 2.

members of the group (HCG 22d and e) were subsequently shown to be background galaxies. The archival observations of HCG 22 form a very broad (in RA) mosaic of the group, however, only two galaxies, HCG 22c and NGC 1231 are detected within this field (Figures 13 & 14). The latter is separated from the core group by over $20'$ and we do not consider it as a group member at present. HCG 22c shows a clean velocity field and we do not see evidence for tidal features in the cube. We also note that the tabulated redshift for HCG 22c from (Hickson et al. 1992) appears to be erroneous (Figure 14). NGC 1231 shows some minor disturbances in the outskirts of its disc which we separate from its disc emission (even though it will not be included in our analysis of the H I content of the group). This is likely a result of interactions with its neighbour, NGC 1209. We also note that we consider NGC 1188 as a member of HCG 22,

as it is at the same redshift and close to the edge of the group. It is not detected in H I.

3.8. HCG 23

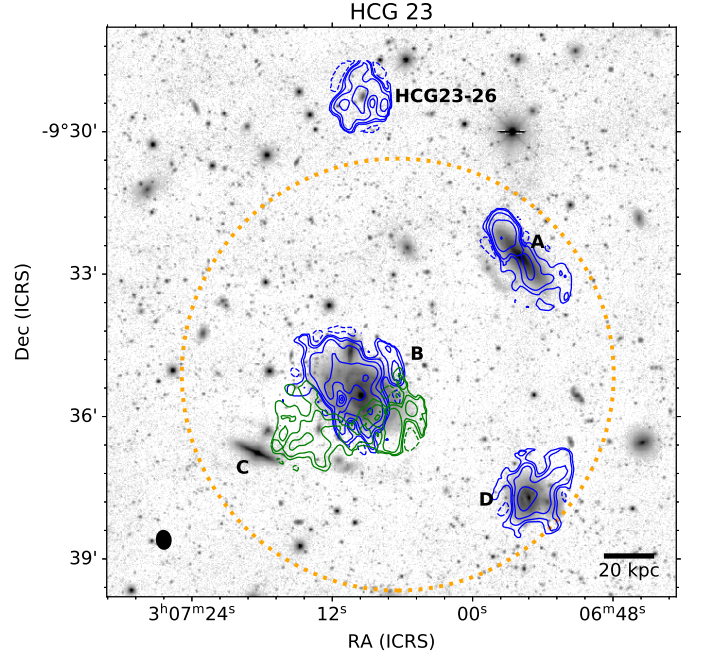


Fig. 15. As in Figure 3.

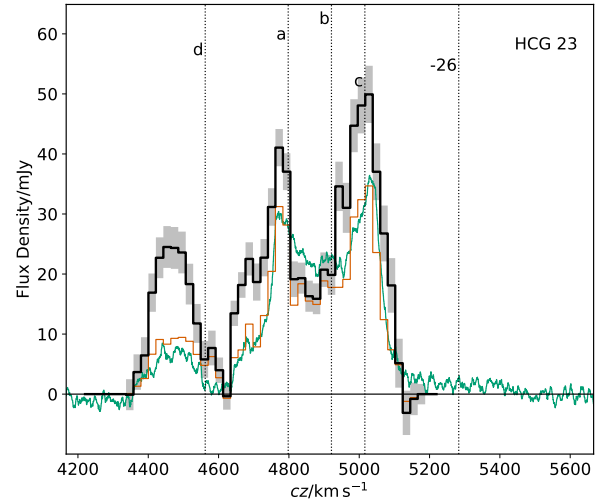


Fig. 16. As in Figure 4.

HCG 23 is a quintet of four late-type and one lenticular galaxies in a 'T' configuration in the range $4500\text{--}5300\text{ km s}^{-1}$. The narrow bands available for the historical VLA and the original observing strategy for this group, with the overlap of the two spectral windows centred at the redshift of the group's peak H I emission, led to imperfect continuum subtraction and poorly behaved noise for this group. This complicates the interpretation of faint features in this cube.

In the core group HCG 23a, b, and d are detected, HCG 23c is undetected. Outside the core group there are three further detections: HCG 23-26 (de Carvalho et al. 1997), PGC 987787, and PGC 011654. We consider the first of these as a group member, but the latter two are separated from the core group by well over 100 kpc and show no signs of past interaction with the group.

HCG 23b has two small tidal tails emanating from it. The first extends SE towards HCG 23c, and the second towards the SW (Figures 15 & 16). The remaining galaxies don't show any clear tidal features above the noise level. We also note that the emission from the almost edge-on HCG 23a is split into two separate sources by SoFia, which we combine into one.

3.9. HCG 25

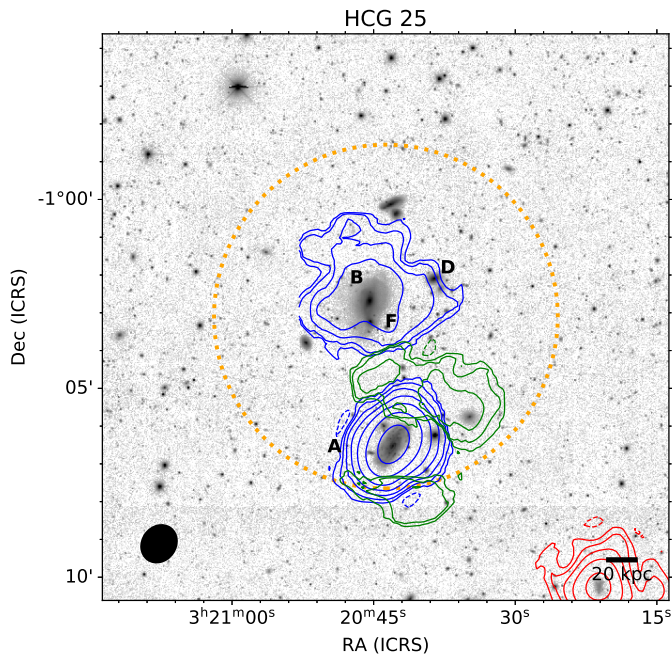


Fig. 17. As in Figure 3.

HCG 25 is a quartet of two late-type and two lenticular galaxies at $\sim 6300 \text{ km s}^{-1}$ (HCG 25c, e and g are all background objects). The moment zero map of this group shows four clear detections (Figures 17 & 18), HCG 25a and b in the core group, PGC 135673 slightly to the north, and the LSB galaxy 2SLAQ J032021.10-011013.6 to the SW, subsequently classified as an ultra-diffuse galaxy by Román & Trujillo (2017). For brevity we refer to the latter as HCG 25S1. Both of these detections of the periphery of the group are separated from the core group by well over 100 kpc and we do not consider them as current members.

HCG 25a and b are connected by a faint H I bridge, which we attempt to separate from the emission of the two galaxies themselves. However, this is complicated by the fact that it is at the limit of the spatial resolution and that, although HCG 25b is a strongly detected source overall, it is low S/N in individual channels. Thus the separation is largely based on the form of the emission from HCG 25a and the optical locations of the galaxies. HCG 25a also has an apparent incipient tidal tails connected to it on the NW and SW sides, which we also separate from the disc emission.

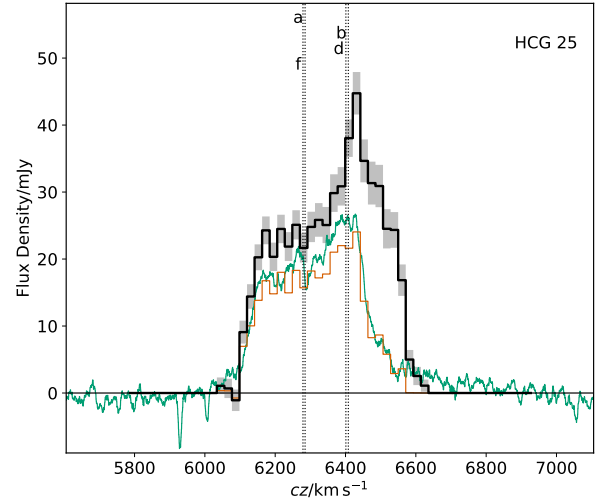


Fig. 18. As in Figure 4.

3.10. HCG 26

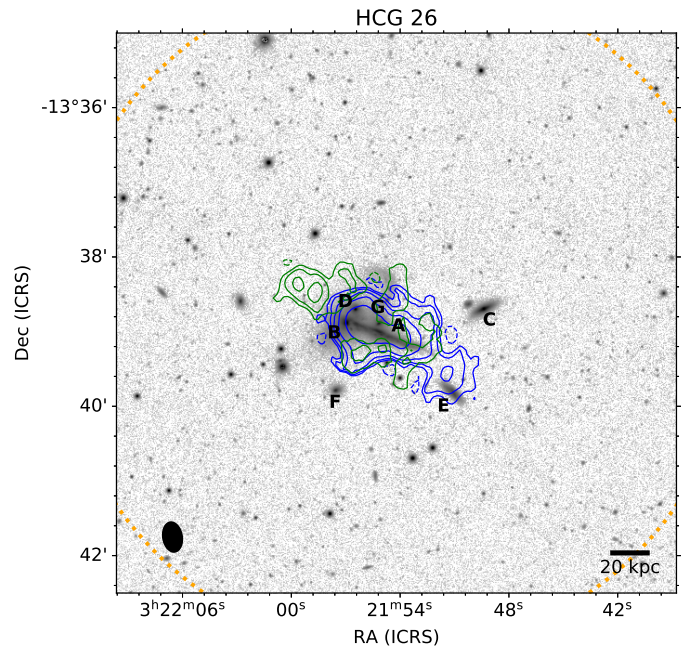


Fig. 19. As in Figure 3.

HCG 26 is a septet of galaxies between $9100\text{--}9700 \text{ km s}^{-1}$, dominated by the edge-on late-type HCG 26a (Figure 19). The vast majority of the H I emission detected in HCG 26 belongs to HCG 26a (although there appears to an offset between the catalogued redshift and the H I emission, Figure 20). HCG 26e is also faintly detected as well as some tidal features. The velocity structure of HCG 26a dominates almost the entire band and appears to be mostly regular, however, there are two clear tidal features, one extending towards HCG 26e and another extending in the opposite directions towards the NE. There are also numerous apparent minor clumps of H I emission that do not follow the velocity structure of HCG 26a. These were excised wherever possible, but the limited resolution and S/N of the features pre-

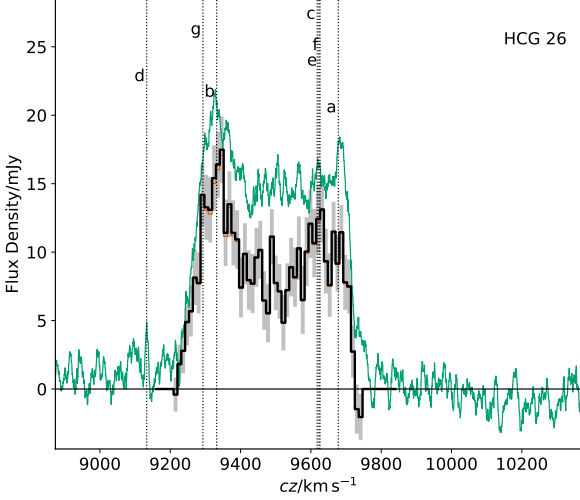


Fig. 20. As in Figure 4.

sented a challenge and some fainter features have likely not been successfully separated. HCG 26e itself appears significantly perturbed, not displaying a clear velocity structure, but given the resolution and low S/N of the detection it is difficult to draw more detailed conclusions. There also appears to be a $\sim 30\%$ offset between the GBT and VLA spectra of this group. Given the similar forms of the spectral profiles, this is most likely the result of differing absolute calibrations or continuum subtraction. However, the root cause could not be definitely identified.

3.11. HCG 30

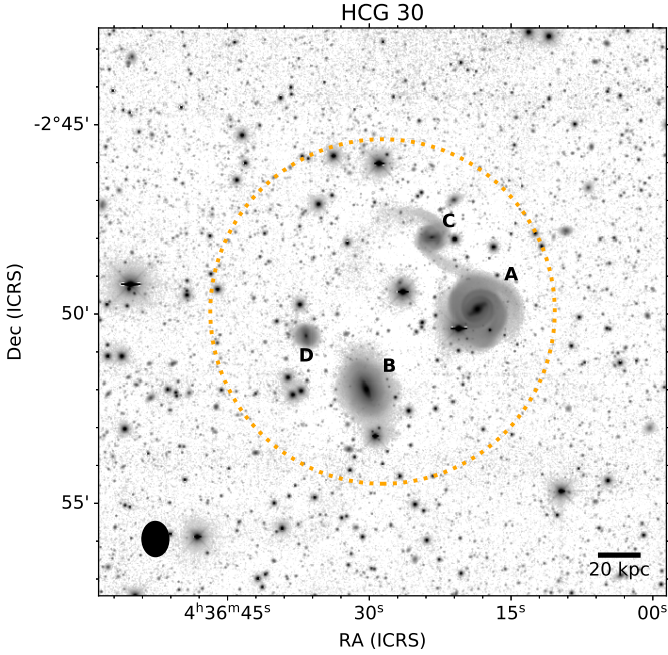


Fig. 21. As in Figure 3.

HCG 30 is a quartet of three late-type and one lenticular galaxies at $\sim 4600 \text{ km s}^{-1}$. None of the core members of

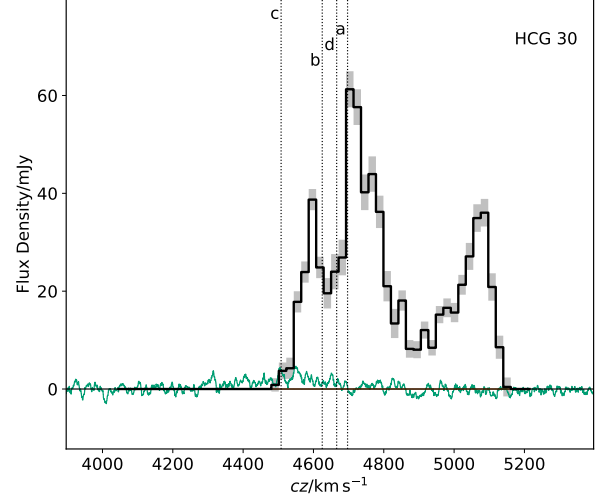


Fig. 22. As in Figure 4. Note that the emission in the VLA spectrum here is all emission beyond the core group, but still within the primary beam of the VLA. Therefore, it is not shown in Figure 21.

HCG 30 are detected in the H I cube (Figures 21 & 22). However, three galaxies, 6dFGS gJ043650.5-030237 (which we refer to as HCG 30dF1), NGC 1618, and NGC 1622, are strongly detected close to the edge of the VLA primary beam. None of these three detections appear particularly disturbed in H I (at the resolution of the data) and it is unlikely that they have ever interacted with the core group. Thus we do not consider them in our H I analysis of the group. NGC 1618 and NGC 1622 are both split into two separate sources by SoFiA, which we manually combine, but other than this no modification or separation of features was performed. The emission from these three detections accounts for the entirety of the flux in the VLA spectrum (Figure 22) and when the data are weighted to compare to the GBT spectrum there is no flux remaining.

In addition it should be noted that three channels ($4364\text{--}4406 \text{ km s}^{-1}$) in this data set were entirely flagged and a number of (primarily negative) low-level artefacts remain in the cube. Thus, positivity was enforced when creating the SoFiA mask and the threshold raised from 4σ to 5σ to increase reliability.

3.12. HCG 31

HCG 31 is quintet of late-type galaxies at $\sim 4100 \text{ km s}^{-1}$, three of which overlap with each other on the plane of the sky and are likely in the process of merging. The H I emission in HCG 31 is an extremely complicated mixture of dwarf galaxies and tidal features (Figure 23), studied in detail by Verdes-Montenegro et al. (2005a) based on an independent reduction of the same VLA data. HCG 31a, b, c, g (IC 399), and q (WISEA J050138.33-041321.2) are all detected in H I. Most of these galaxies are highly disturbed and are embedded in an almost continuous set of tidal features which spans the entire group. HCG 31e and f are also detected in H I, but are candidate tidal dwarf galaxies embedded in an H I tail (e.g. Mendes de Oliveira et al. 2006), and we therefore consider them as tidal features rather than normal galaxies. Verdes-Montenegro et al. (2005a) also noted the H I detection of PGC 3080767 to the south of the group, however, this is separated from the rest of

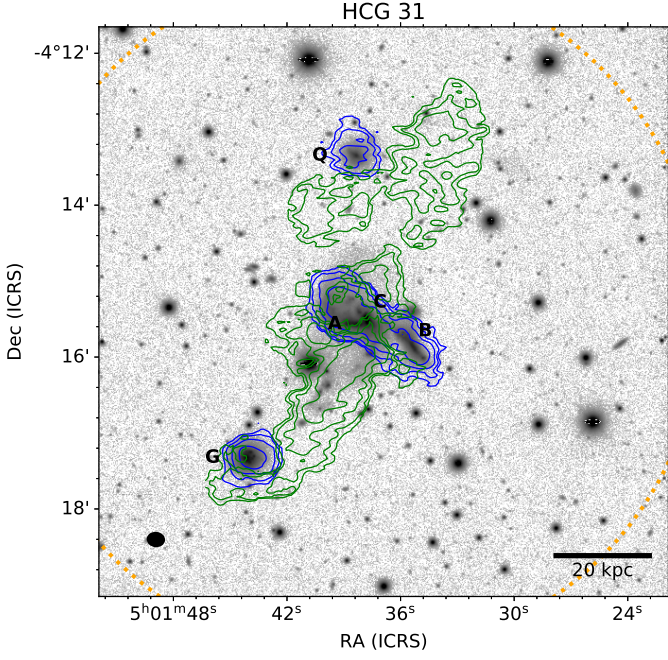


Fig. 23. As in Figure 3.

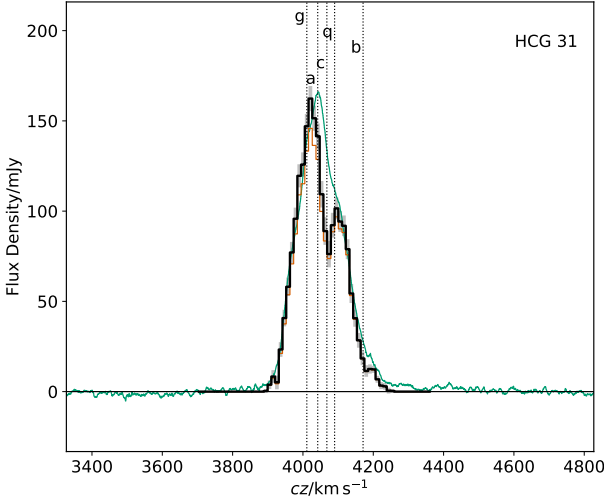


Fig. 24. As in Figure 4.

the group by over 200 kpc and we do not consider it a member. There are also some blue clumps visible in the DECaLS image within the extended H I features around HCG 31q (to the north of the core group), which may be other cases of in situ star formation. We also note that the absolute flux scale resulting from our calibration appears considerably higher than that of Verdes-Montenegro et al. (2005a), which greatly improves how well the integrated H I profile of the group matches to GBT observations shown Figure 24 (c.f. Borthakur et al. 2010).

Reliable separation of galaxies and tidal material in this group is extraordinarily challenging, in particular the galaxies HCG 31a and c, which are not only blended with tidal material, but also each other. The reported H I masses for these two galaxies and, to a lesser extent, the other galaxies in the group are undoubtedly quite uncertain (for example, the approaching side

of HCG 31b is deeply embedded in the complex of emission at the centre of the group). Despite this difficulty, what is clear, and of most importance for this work, is that a substantial fraction of the total H I emission of this group originates in the IGrM.

3.13. HCG 33

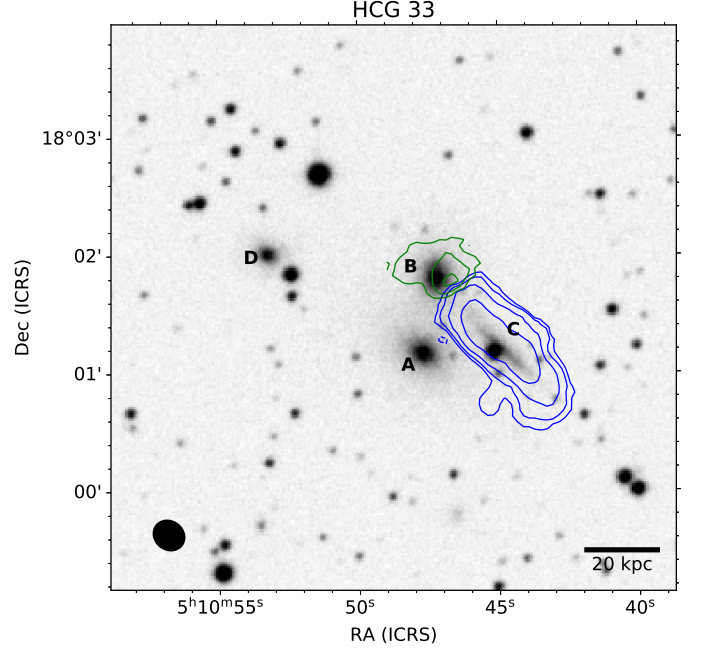


Fig. 25. As in Figure 1, except the background image is POSS *R*-band.

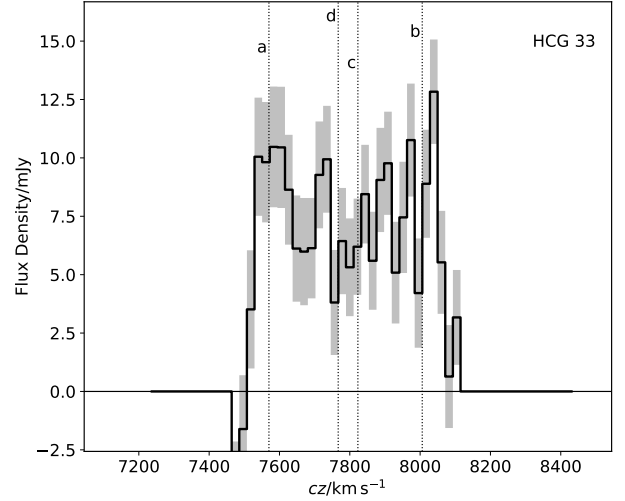


Fig. 26. As in Figure 2.

HCG 33 quartet of three early-type galaxies and a late-type galaxy in the redshift range 7500–8000 km s^{−1}. Only HCG 33c is detected in H I with the VLA (Figures 25 & 26). The velocity structure of HCG 33c spans a large fraction of the observational bandwidth and is mostly regular except for a clear incipient tidal feature extending to the NE, which we separate from the galaxy’s emission.

3.14. HCG 37

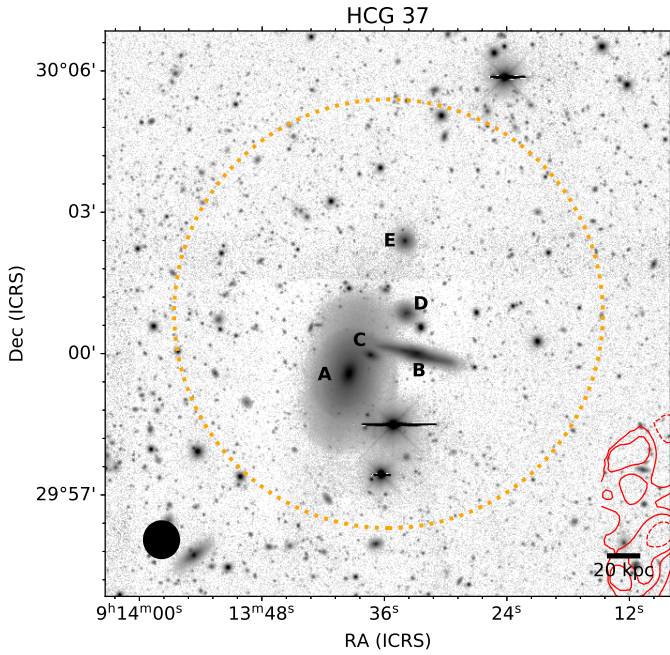


Fig. 27. As in Figure 3.

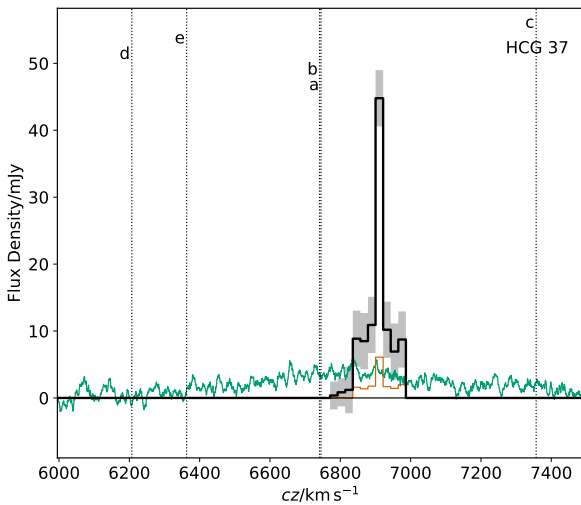


Fig. 28. As in Figure 4.

HCG 37 is a very compact quintet containing two early-type, one lenticular, and two late-type galaxies in the redshift range $6300\text{--}7400\text{ km s}^{-1}$. None of the core galaxies of HCG 37 are detection in H I with the VLA (Figures 27 & 28). The only feature above SoFiA's threshold is an amorphous blob to the SW of the group. This feature may be spurious, however, its peak coincides with an uncatalogued LSB dwarf galaxy (at $09^{\text{h}}13^{\text{m}}05.95^{\text{s}} +29^{\circ}55'14.2''$), which we refer to as HCG 37LSB1. We separated this feature into the densest clump that appears to be associated with an optical counterpart and the more diffuse emission. However, if associated with the LSB counterpart then this source

is separated from the core group by well over 100 kpc and we do not consider it part of the compact group at present.

3.15. HCG 38

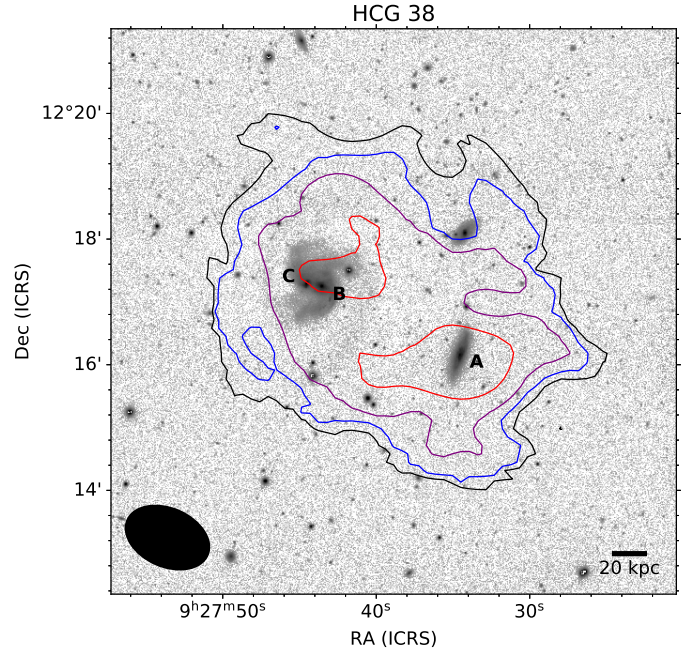


Fig. 29. Integrated H I emission (moment 0) contours overlaid on a DECaLS r-band image. Contours begin at 2σ (solid black lines) and each subsequent contour is a factor of two greater. The dashed black contours indicate -2σ . The VLA synthesised beam is shown as a black ellipse in the bottom left and a 20 kpc scale bar is in the bottom right.

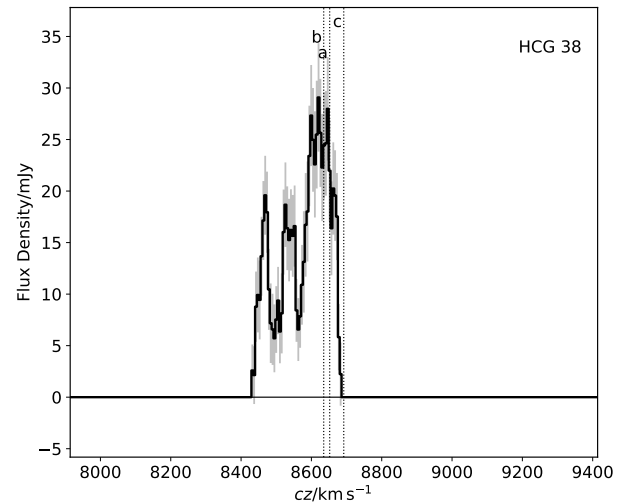


Fig. 30. As in Figure 2.

The single short observation of this group was hampered by RFI resulting in poor uv coverage, a poorly behaved synthesised beam, and a noisy cube. We caution the reader that results for this group are less reliable than for most others.

This group is apparently a triplet of late type galaxies at 8700 km s^{-1} (the redshift of HCG 38d places it in the distant background), where two of the members appear to be merging HCG 38b and c. In our H I cube we detect emission in the vicinity of all of these galaxies, as is apparent in the moment map (Figure 29). However, given the poor angular resolution and the noisy nature of the cube, emission is extremely challenging to confidently identify in individual channels and we thus do not attempt separation of features in this group. Will consider it only in terms of its global properties in the following analyses (Figure 30).

3.16. HCG 40

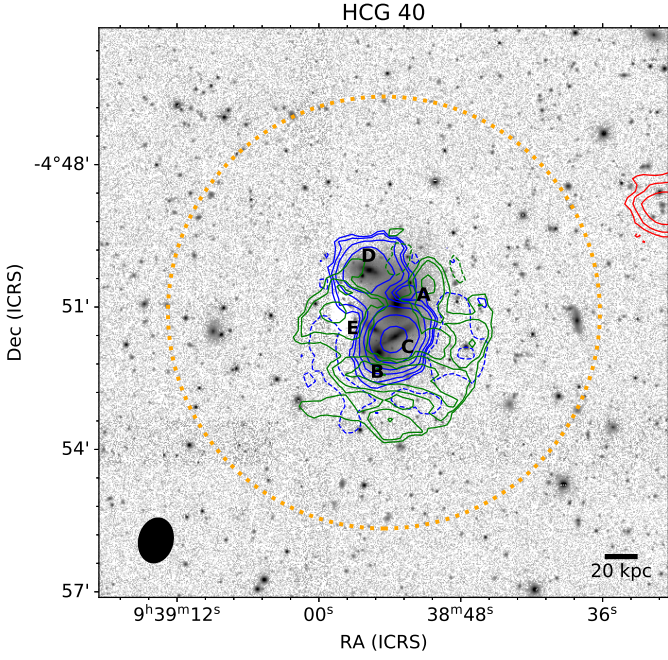


Fig. 31. As in Figure 3.

HCG 40 is an extremely compact configuration of five galaxies (three late-type and two early-type) in the redshift range $6400\text{--}6900 \text{ km s}^{-1}$, all of which overlap on the plane of the sky with their nearest neighbour. In the H I cube the only well-defined velocity structures (in the vicinity of the core group) align with the major axes of HCG 40c and d. We therefore attribute most of the H I to these two galaxies. Although some emission is classified as tidal features as it clearly does not conform to a disc-like structure, this is mostly low significance emission with minimal flux. To the NW of the group another H I source is detected, probably associated with GALEX-ASC J093831.05-044853.6. For brevity we will refer to this as HCG 40GLX1. This object is separated from the core group by $\sim 150 \text{ kpc}$ and we do not consider it as a member.

3.17. HCG 47

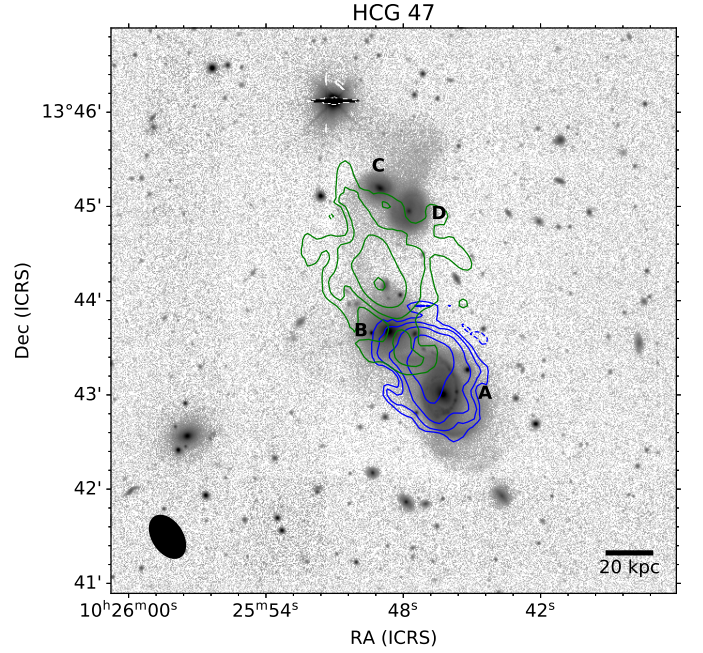


Fig. 33. As in Figure 1.

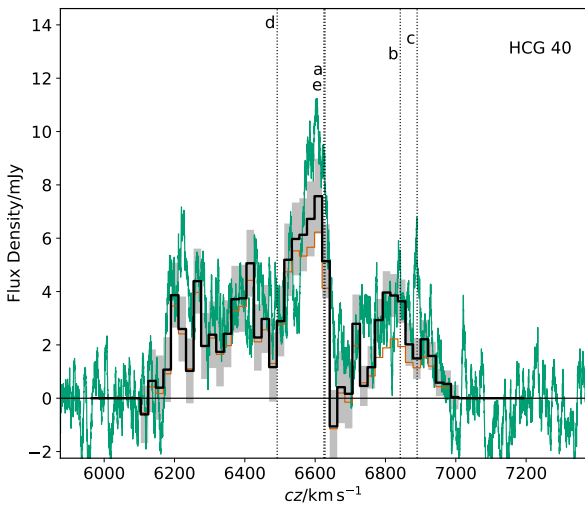


Fig. 32. As in Figure 4.

HCG 47 has the appearance of a pair of pairs, with the two larger galaxies, HCG 47a and b, in the south and the two smaller galaxies, HCG 47c and d, to the north, all of which are in the redshift range $9400\text{--}9600 \text{ km s}^{-1}$. H I emission is detected in HCG 47a and b and towards HCG 47c and d (Figures 33 & 34). However, much of this is a relatively low S/N, an issue which is exacerbated by the fact that the synthesised beam has significant side lobes due to the short observations and poor resulting uv coverage. In addition, five channels ($\Delta v \approx 24 \text{ km s}^{-1}$) near the centre of the cube were entirely, or almost entirely, flagged due to RFI.

The SoFiA mask contains two separate regions of H I emission. One, upon inspection of the channel maps, appears to mostly coincide with HCG 47a and b, while the other lies in between the two pairs. Owing to the difficulties with the data quality, we simply denote the first region as being from HCG 47a and b combined (although likely the majority is from HCG 47a), while the latter region is classified as extended emission which does not coincide with a galaxy. The reader is cautioned that the results for this group are quite uncertain.

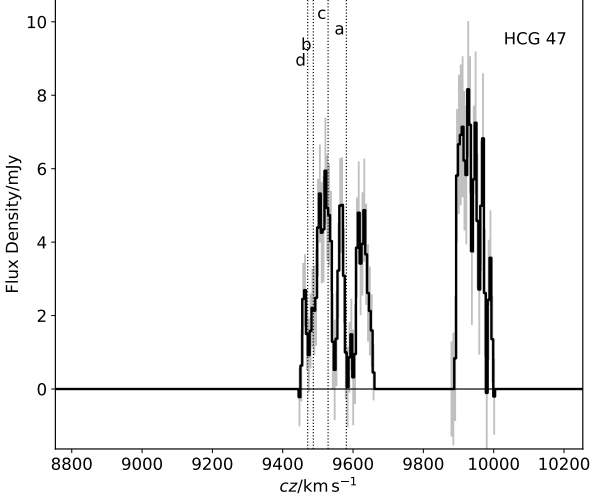


Fig. 34. As in Figure 2.

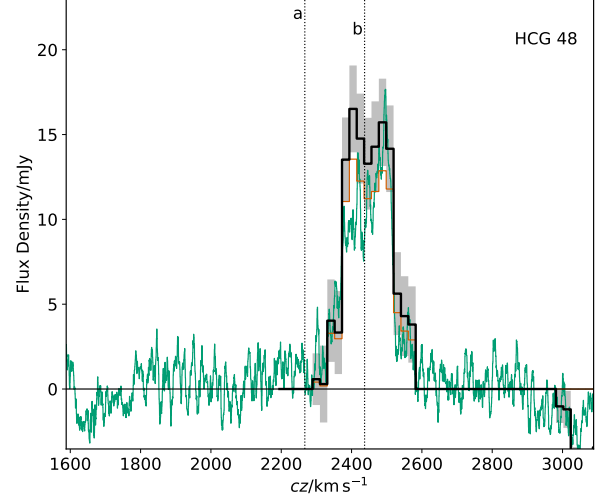


Fig. 36. As in Figure 4.

3.18. HCG 48

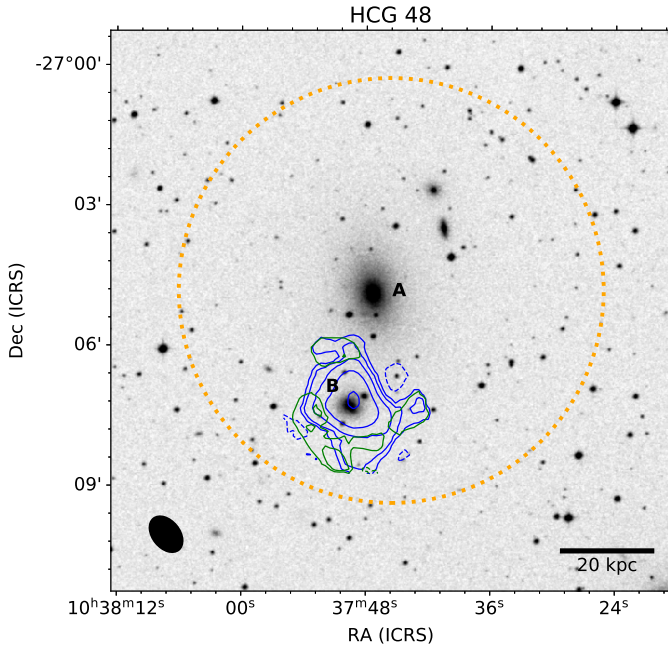


Fig. 35. As in Figure 3.

HCG 48 is likely a false group and is really just a pair of galaxies (HCG 48a, a large elliptical, and HCG 48b, a smaller late-type galaxy). The other two original members of this group were revealed to be a background pair once redshifts were obtained (we also note that there are several conflicting redshift measurements for these galaxies in the literature). In the VLA data only the H I emission from HCG 48b is detected, as well as PGC 762452, approximately 165 kpc to the NW (Figures 35 & 36). The H I cube has mostly well-behaved noise, but there is a continuum artefact NW of the group, as well as some structured noise. There are a few minor, low significance H I features connected to HCG 48b which we assign as tidal. In summary, as this

HCG is unlikely to be a genuine group we do not consider it in the remainder of our analysis.

3.19. HCG 49

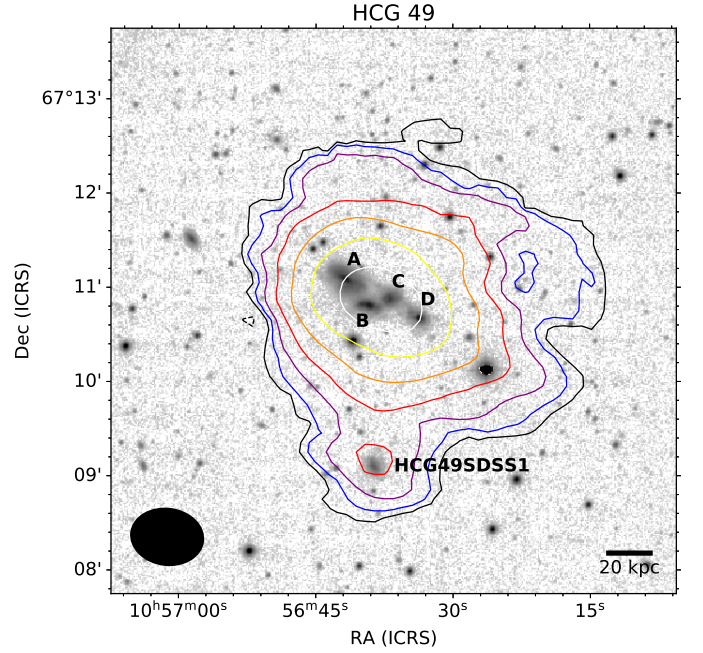


Fig. 37. As in Figure 29.

HCG 49 is an extremely compact configuration of three late-type galaxies and one early-type, with an additional late-type slightly to the south. All have redshifts of $\sim 10000 \text{ km s}^{-1}$. Owing to the distance of this group $\sim 140 \text{ Mpc}$, the physical resolution of the VLA DnC imaging is extremely poor. There is no possibility of reliably separating emission from the four core group members as this appears almost as one continuous cloud in the H I cube (Figures 37 & 38). Therefore, we approximately separate the emission of SDSS J105638.63+670906.0 (HCG 40SDSS1,

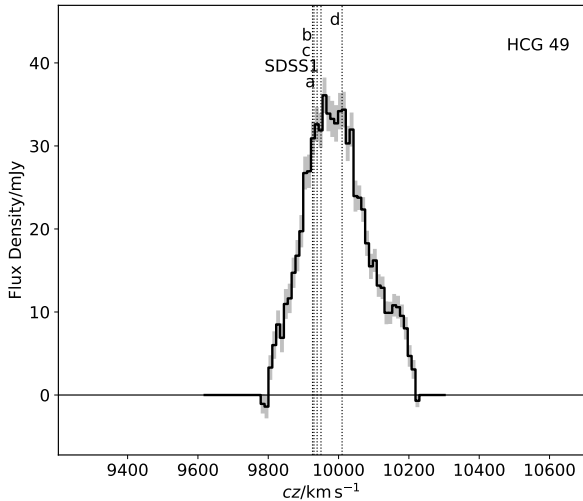


Fig. 38. As in Figure 2.

the galaxy slightly to the south), which does appear to be interacting with the core group (though resolution is a limiting factor), and SDSS J105454.97+670919.4 (HCG 40SDSS2), detected about 350 kpc to the west (not considered a member). However, for the remainder of this work this group will only be considered in terms of its global properties.

3.20. HCG 54

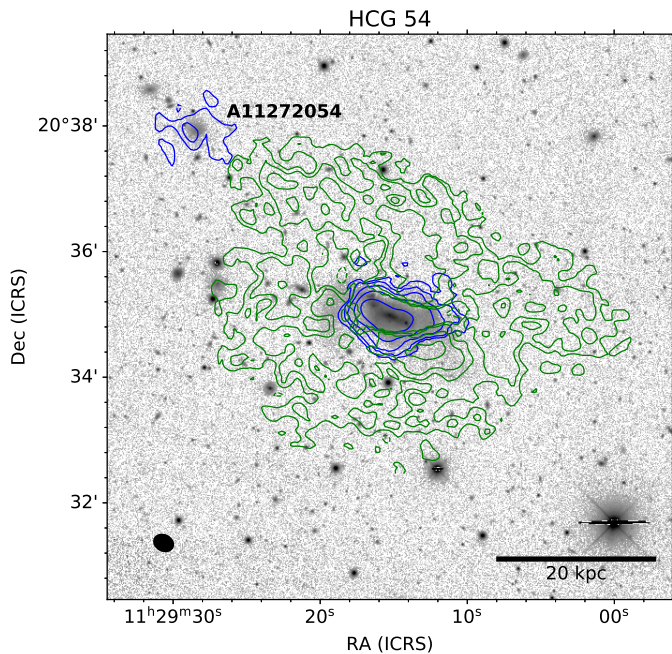


Fig. 39. As in Figure 1.

HCG 54 is a tight, linear arrangement of what were originally thought to be late-type dwarf galaxies (Hickson 1982), but are likely all regions associated with a merger event of two or more galaxies (Verdes-Montenegro et al. 2002). The H I emission mapped with the VLA spans all the bright, star-forming

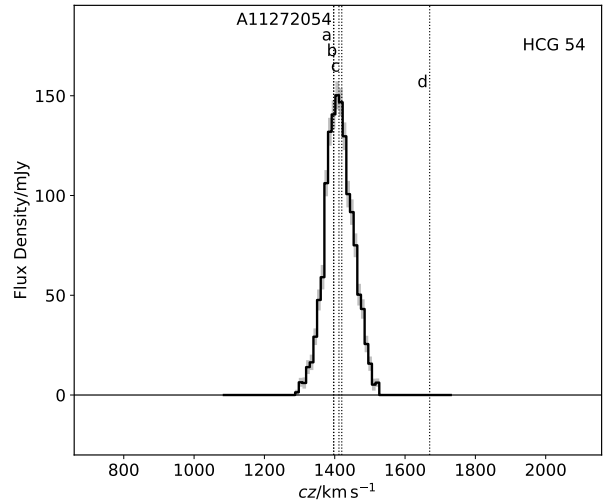


Fig. 40. As in Figure 2.

components of this merger and includes a significant tidal tail which wraps around to the north of the group (noted previously by Verdes-Montenegro et al. 2002). The moment zero map of the group has a mottled appearance due to significant side lobes to the synthesised beam (Figures 39 & 40).

We do not attempt to separate individual features in the main region of H I emission, which forms a contiguous structure from one side of the merger to the other. However, we do separate the clear tidal extended features around the group. In particular, there is a main tail that wraps around the merger and ends in the galaxy A1127+2054. As this HCG mainly consists of a single merger in cannot be considered as a group in the same manner as the other groups and we therefore do not consider it in our analysis.

3.21. HCG 56

HCG 56 is a compact configuration of four lenticular and one late-type galaxies in the redshift range 7900-8400 km s⁻¹. Only HCG 56a is detected in H I, which is an extremely high S/N detection with a clear, regular velocity structure (Figures 41 & 42). No separation of features is required as this is the only source in the SoFiA mask and there are no clear signs of tidal tails. However, there are some low significance features which did not reach the threshold required to be included within the SoFiA mask, deeper mapping would be required to verify these features and reveal if they are genuine H I associated with the remaining galaxies.

3.22. HCG 57

HCG 57 is a group of eight, mostly late-type, galaxies in the redshift range 8700-9600 km s⁻¹. The three galaxies at the centre of the group (HCG 57a, c, and d) appear to be detected in the VLA observations (Figures 43 & 44). However, the data quality is not optimal, with a relatively poorly behaved synthesised beam and some residual structure in the noise that becomes visible when summing several channels. Given these limitation we do not attempt to separate this emission into distinct galaxies and tidal

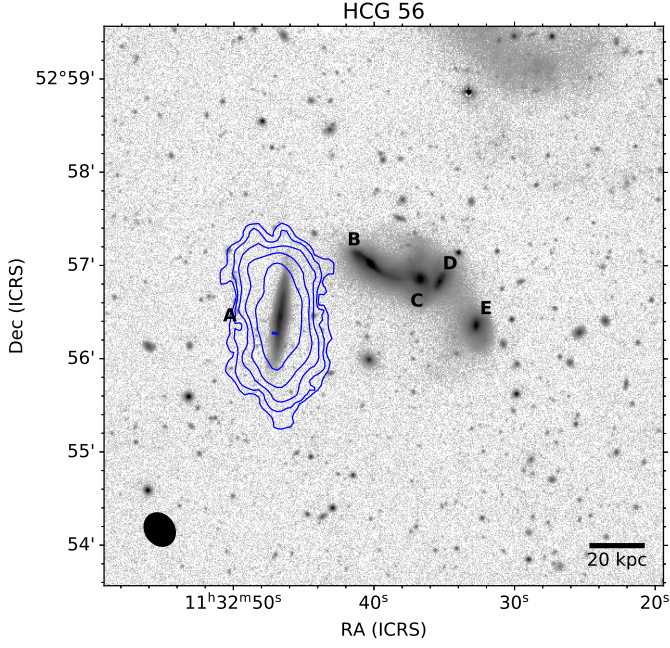


Fig. 41. As in Figure 1. Note that the extend feature in the NW corner of this image is due to a large foreground galaxy just outside the frame.

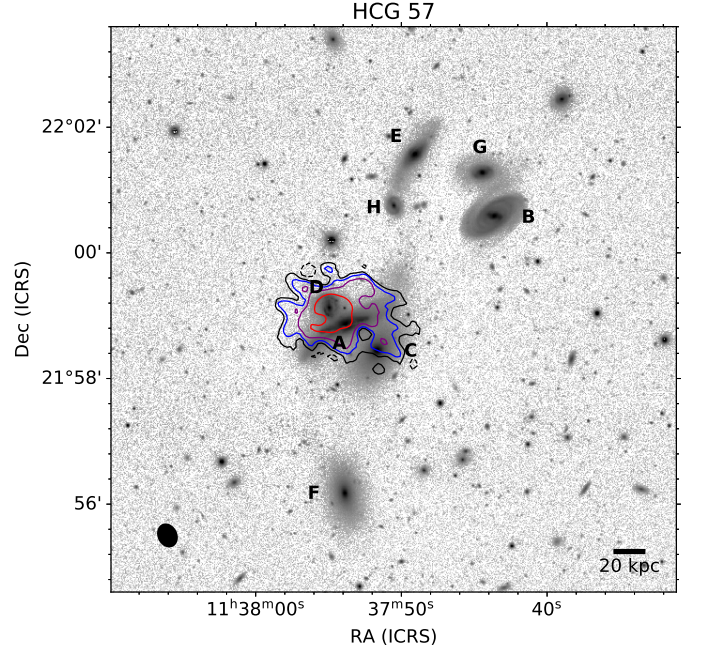


Fig. 43. As in Figure 29.

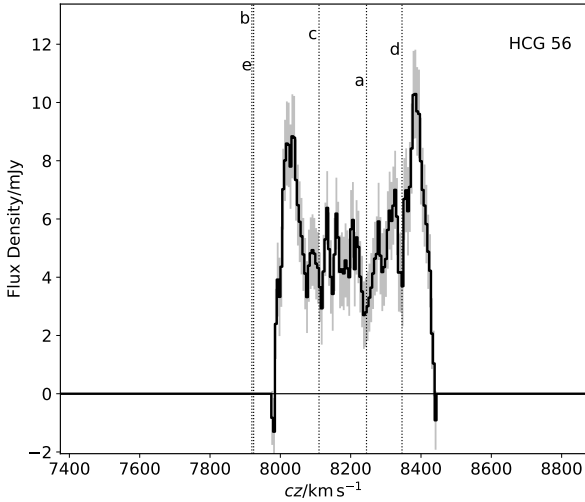


Fig. 42. As in Figure 2.

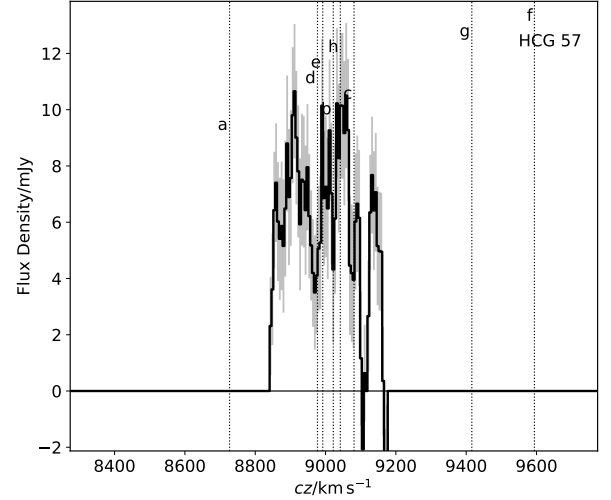


Fig. 44. As in Figure 2.

features, and will consider this group only in terms of its global H I properties.

In addition, we detect faint H I emission approximately 400 kpc to the SW of the group. This appears to coincide with an uncatalogued LSB galaxy. However, we note that given the low data quality this detection may be spurious and the apparent optical counterpart coincidental.

3.23. HCG 58

HCG 58 is a configuration of three late-type galaxies, one lenticular, and one early-type. H I emission is detected in the VLA observations throughout the structure (Figures 45 & 46). The core group is also surrounded by a number of other galaxies, sepa-

rated from the core group by 200-500 kpc, several of which we also detect in H I but do not consider as members of the core group. There is a continuum subtraction artefact to the south of the core group which was excluded when generating the SoFia mask.

Although H I is detected that is co-spatial with all the five group members, there are only clear overdensities associated with HCG 58a and e. The remaining galaxies appear so disturbed that they are virtually indistinguishable from the gas that fills the IGrM. We therefore separate only the high density gas associated with HCG 58a and e, and mark all remaining gas in the group as belonging to extended features.

The VLA spectrum weighted to match the GBT beam response (orange line, Figure 46) is down-weighted so much in comparison to the raw spectrum that it is significantly below the

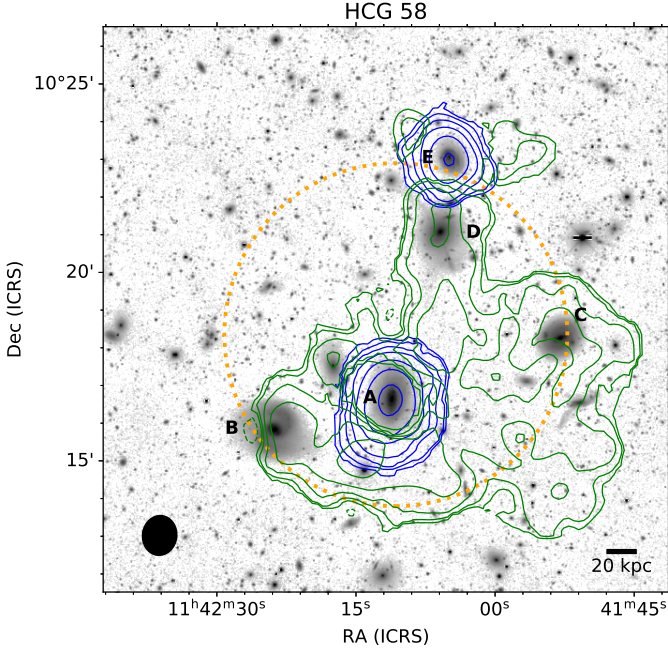


Fig. 45. As in Figure 3.

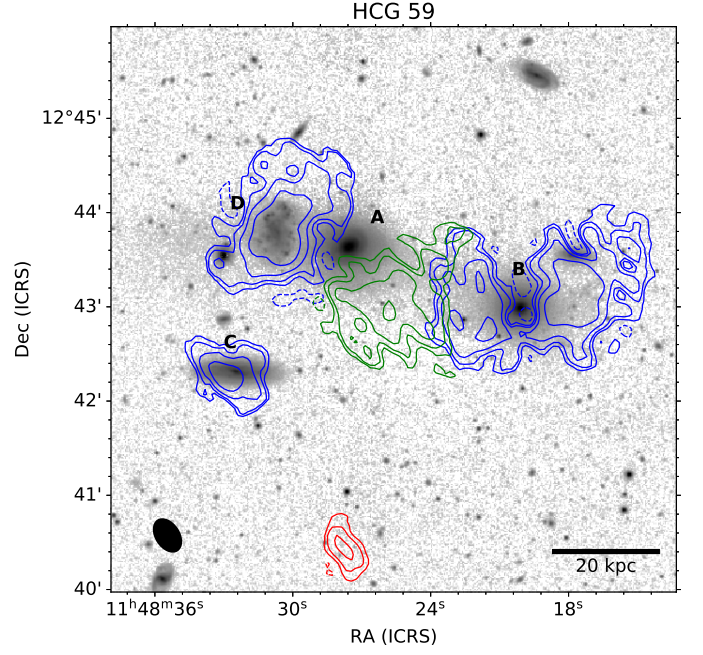


Fig. 47. As in Figure 1.

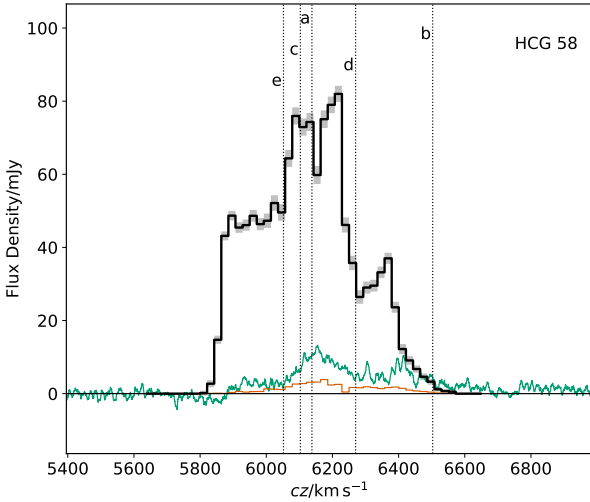


Fig. 46. As in Figure 4.

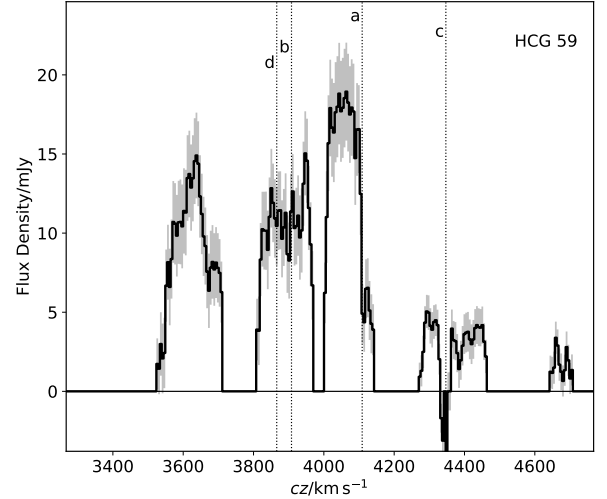


Fig. 48. As in Figure 2.

GBT spectrum. Given that HCG 58e is on the edge of the GBT primary beam (Figure 45) and much of the extended emission is beyond the beam, this comparison will be extremely sensitive to the approximate beam model we have assumed. In addition, any minor pointing offset in the GBT observation would also lead to significant differences in the comparison. Thus, although the GBT spectrum appears to contain considerably more flux, it is difficult to be certain that this indicates emission that was missed by the VLA.

3.24. HCG 59

Unlike all other sources the H I data for HCG 59 went through an additional step of self-calibration due to strong interference fringes originating from a bright, double continuum source near

the edge of the primary beam. These additional steps greatly reduce the strength of artefacts in the H I cube, however, there is still some residual structure in the noise and a high threshold (5σ) is used in SoFiA to attempt to eliminate them.

HCG 59 is a group of two spirals, one irregular and one elliptical galaxy arranged in an L-shape at a redshift of approximately 4000 km s^{-1} . All four appear to be detected in H I with the VLA data, although the H I emission of HCG 59c is interrupted by RFI (Figures 47 & 48). Although the emission from the three of these galaxies appears to overlap in the moment map, but are separated by slight differences in their radial velocities. The spectrum of the group also implies that the catalogued redshift for HCG 59d is offset from its H I velocity by over 200 km s^{-1} . A 5th H I detection occurs just south of the core group. There does not ap-

pear to by any optical counterpart to this source (which we label HCG 59LSB1) and it is likely spurious.

The low quality of the data makes confident separation of features challenging and caution is advised when interpreting results of this group. However, while in the cases of HCG 59c and d the H I emission appears to be well centred, for HCG 59a most of the H I emission occurs between HCG 59a and b. The emission associated with HCG 59b also appears to have been broken into approaching and receding parts by SoFiA. We therefore attribute, as best as possible, emission associated with HCG 59b and label the remainder as an extended feature rather than gas bound to HCG 59a. This feature is likely an H I bridge between the two galaxies.

3.25. HCG 61

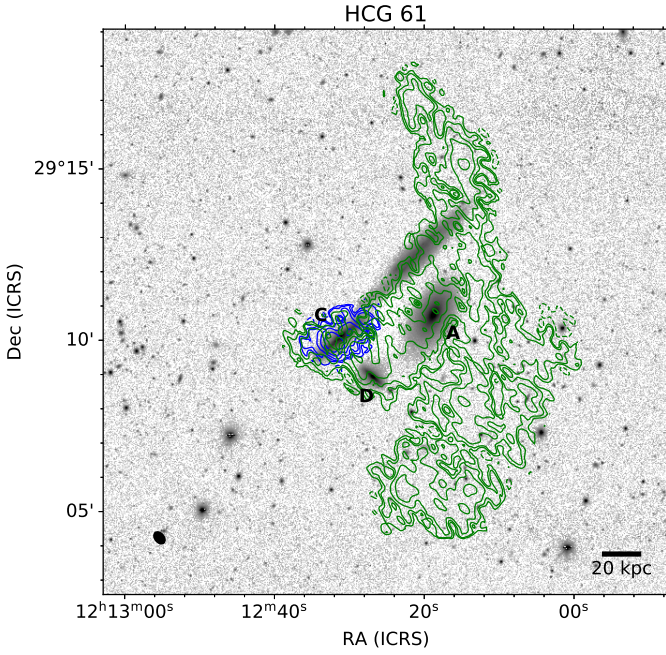


Fig. 49. As in Figure 1.

HCG 61 is a triplet made up of HCG 61a, c and d (HCG 61b is a foreground galaxy). HCG 61a and d are both classified as lenticular and HCG 61c is late-type, but edge-on. The H I map from the VLA shows several enormous extended features reminiscent of HCG 92. The moment zero map appears mottled due to significant side lobes to the synthesised beam.

The most easily discernible galaxy in the H I cube is HCG 61c as a faint, point-like emission region progresses along its edge-on disc when stepping through the channels of the cube in a relatively uniform manner. However, near its central velocity the signal almost entirely disappears and there are several apparent tidal features which we separate as best as possible. Aside from this gas, none of the remainder of the H I emission is definitively associated with either of the other galaxies. Although some of this emission does coincide with HCG 61a and d, and there is some velocity gradient across each, both are embedded in the large extended features and it is unlikely that much of this gas is still bound to the galaxies. Therefore, we classify all remain emission in the group as tidal in nature (Figures 49 & 50).

In addition to the H I in the group we also detect PGC 4316478 about 220 kpc to the SE of the group. This source

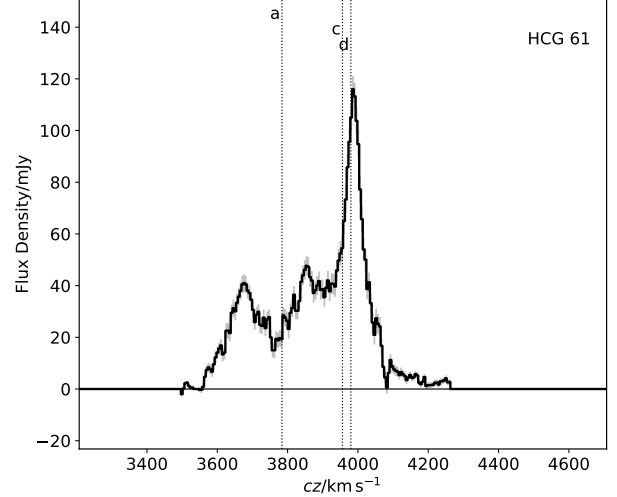


Fig. 50. As in Figure 2.

is at the very edge of the VLA primary beam and its flux is likely unreliable. We do not consider it a member of the group.

3.26. HCG 62

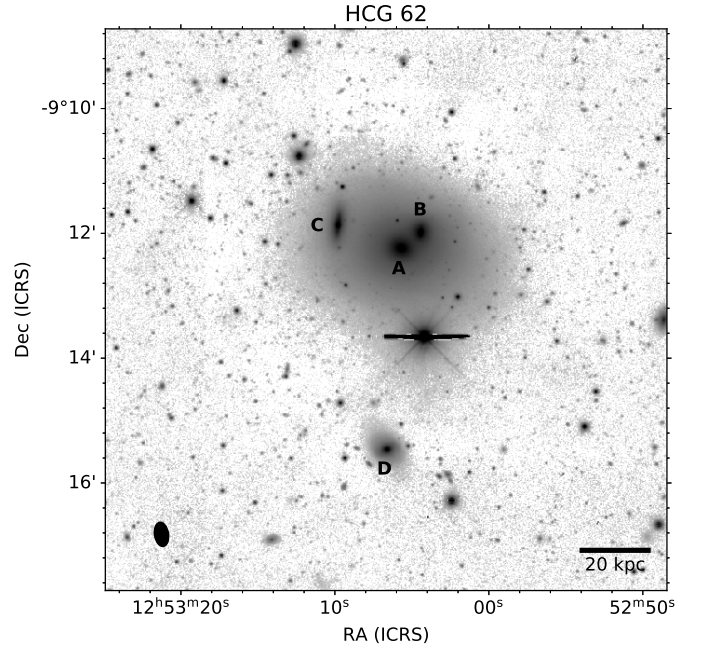


Fig. 51. As in Figure 1, except no H I emission is detected within the group.

HCG 62 is a group of two lenticular and two elliptical galaxies in the range 3600-4400 km s⁻¹. None are detected in the JVLA observations of this group (Figures 51 & 52). Three low significance, outlying clumps exist in the H I spectral line cube. However, these have no apparent optical counterparts and are almost certainly spurious. Therefore, we consider this group as entirely undetected with the JVLA observations.

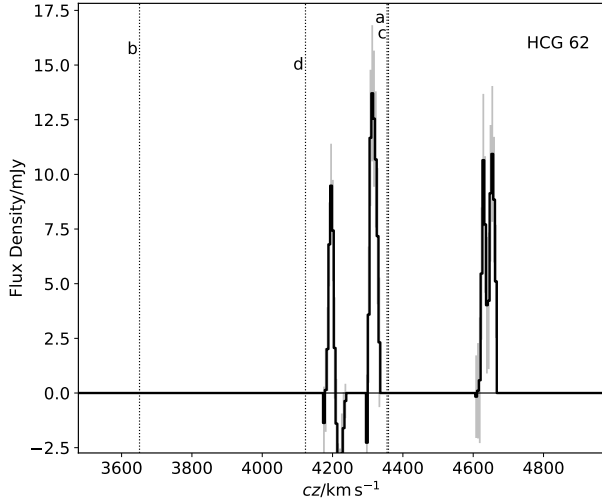


Fig. 52. As in Figure 2.

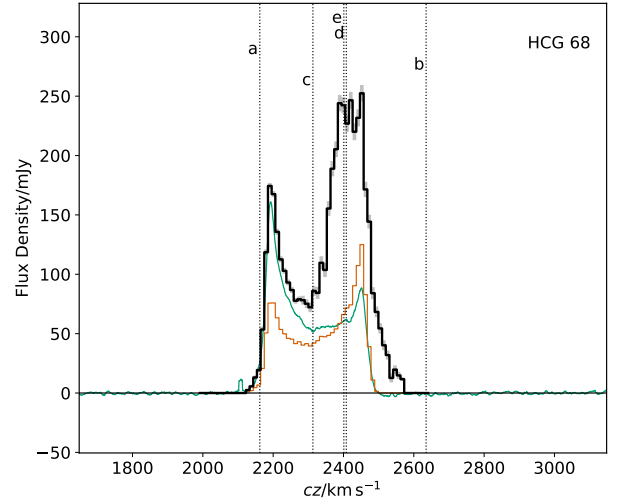


Fig. 54. As in Figure 4.

3.27. HCG 68

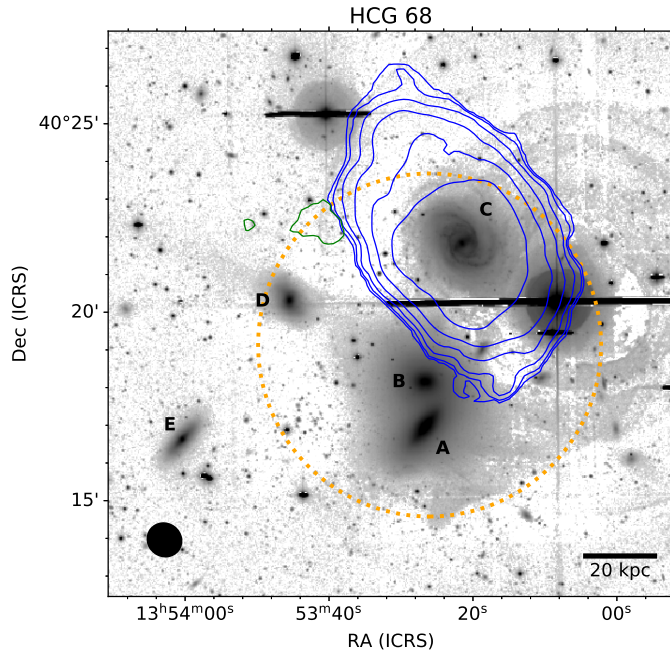


Fig. 53. As in Figure 3.

HCG 68 is a group of five galaxies, two lenticulars, two ellipticals, and one late-type, the only core group galaxy detected in H I with the VLA observations (HCG 68c). The velocity structure of the H I detected in HCG 68c is highly regular, with only a very minor, faint extension on the NW side which we separate as a tidal feature (but may simply be spurious), and a possible slight warp in its outer disc (Figures 53 & 54).

In addition to HCG 68c, UGC 8841 is clearly detected in H I about 150 kpc to the SW of the core group, and NGC 5371 is also detected a similar projected distance to the west of the group. The receding side of NGC 5371 is not visible as this is truncated by the edge of the bandpass of the VLA observation.

We do not consider either of these galaxies as members of the core group.

The comparison of the VLA and GBT spectra in Figure 54 shows a strange phenomenon where at low velocities the GBT spectrum (green line) contains more flux, but at high velocities the VLA weighted spectrum does (orange line). As with HCG 58 this is likely the result of the main source of H I emission lying near the edge of the GBT beam. Even a small offset in pointing or a slight bias in the beam weighting we have used could result in more emission for the receding or approaching side of HCG 68c being included.

3.28. HCG 71

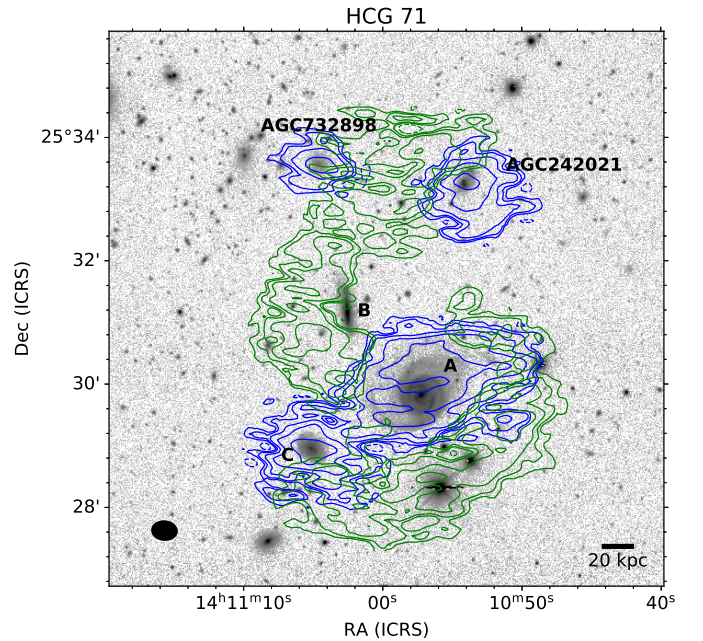


Fig. 55. As in Figure 1.

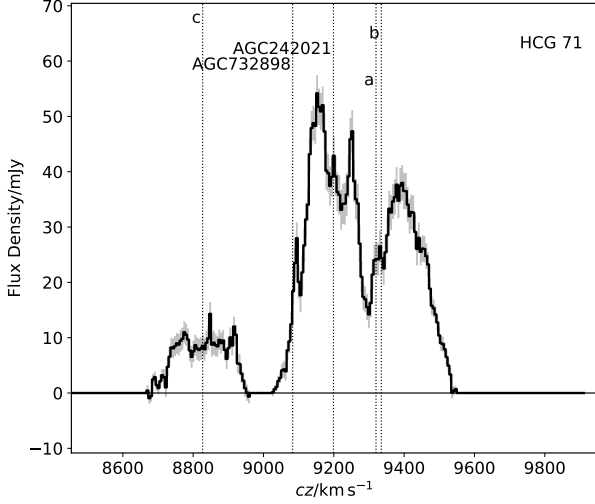


Fig. 56. As in Figure 2.

HCG 71 is a triangular configuration made up of the three late-type galaxies HCG 71a, b, and c (HCG 71d is a distant background galaxy) in the range 8800-9400 km s⁻¹. The H I moment map is dominated by emission associated with HCG 71a, a near face-on spiral (Figures 55 & 56). HCG 71c is also detected, but HCG 71b is not. This emission from HCG 71a stretches out to form a large loop to the north that connects to two LSB galaxies, AGC 732898 and AGC 242021, both of which were detected in H I in the ALFALFA survey (though blended with other emission in the group) and which we consider group members. The moment zero map of the group has a slightly mottled appearance due to significant side lobes and elongation of the synthesised beam, and possible slight residual continuum artefacts.

HCG 71c is slightly separated from the rest of the group in velocity and thus it is straightforward to distinguish its emission. It appears to have two minor (low S/N) extensions to the south and west, which we excise in separate features. HCG 71a has two large tails emanating from the east and west. The latter stretches down to the SE and in the moment map apparently connects to HCG 71c. However, this is a projection effect as in velocity space it stretches away from, not towards, HCG 71c. There is a dense clump of H I emission in the other tail that is at the same velocity as HCG 71b, but it does not quite overlap on the plane of the sky and therefore does not appear to be associated (although perhaps some of this gas originated from HCG 71b). Again, in projection, this tail appears to connect to AGC 732898 and AGC 242021, but veers away in velocity. Although only detected in a small number of channels AGC 732898 appears to have a regular structure and no extended features were identified around it. AGC 242021, on the other hand, appears highly disturbed in H I. We separate the emission into galaxy and extended features, but note that this is quite uncertain for this object.

3.29. HCG 79

HCG 79 is a group of two lenticular, one elliptical, and one late-type galaxy, all of which overlap on the plane of the sky (a 5th galaxy, HCG 79e, is a background interloper) and have redshifts in the range 4100-4500 km s⁻¹. Most of the H I emission detected with the VLA is centred on HCG 79d, the sole late-type galaxy in

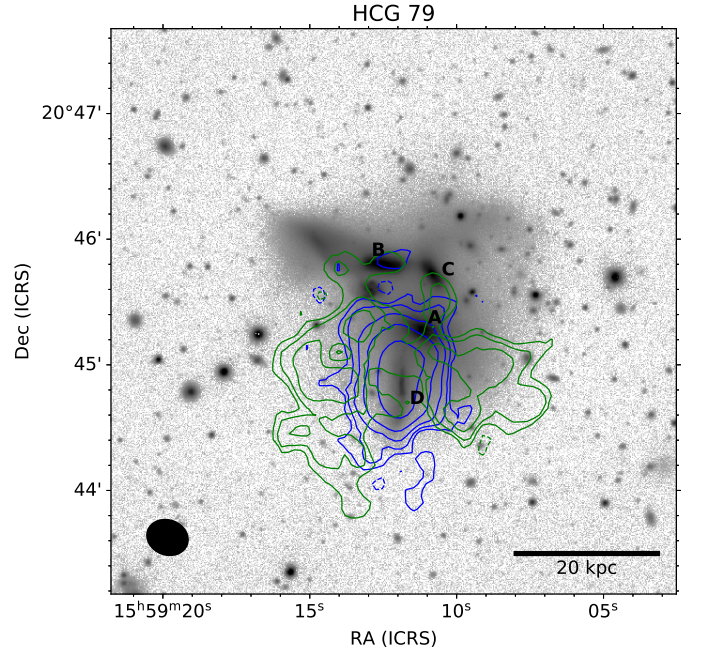


Fig. 57. As in Figure 1.

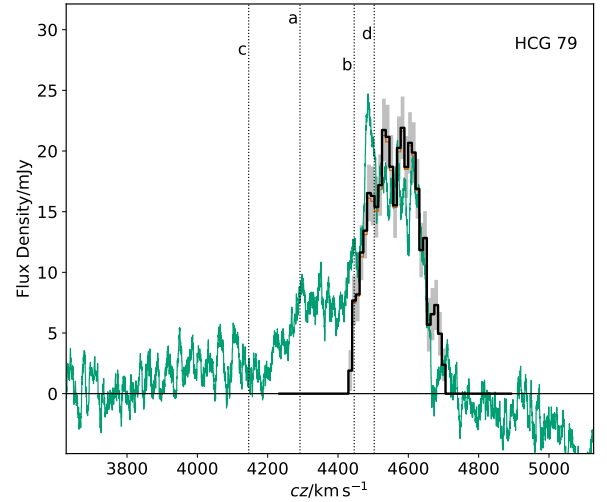


Fig. 58. As in Figure 2.

the group (Figures 57 & 58). There are numerous faint features on the edge of HCG 79d that appear disturbed and are separated out. However, it should be noted that these are faint features that are subject to variations in the noise.

3.30. HCG 88

HCG 88 is a linear arrangement of four late-type galaxies all with redshifts of ~6000 km s⁻¹. All four are detected in H I with the VLA, and have appear mostly undisturbed, except for HCG 88a which appears to have a truncated H I disc (Figures 59 & 60). HCG 88b and c have overlapping H I distributions. The regular velocity structure of the two galaxies implies that this H I is still mostly bound to their respective discs, and therefore we separate the two galaxies as best as possible and assign very lit-

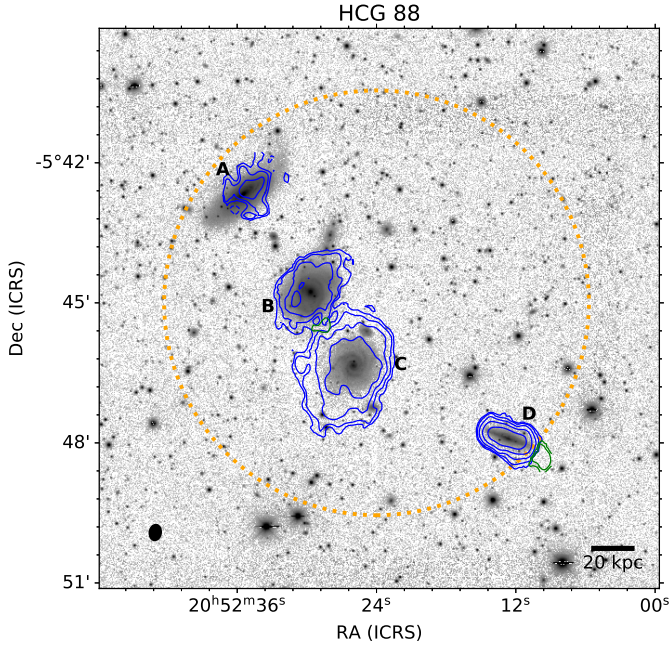


Fig. 59. As in Figure 3.

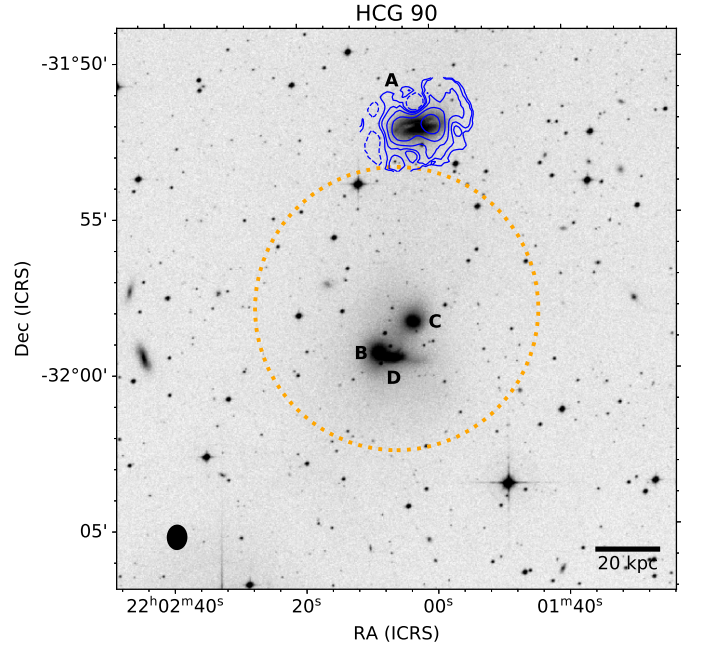


Fig. 61. As in Figure 3, except the background image is POSS *R*-band.

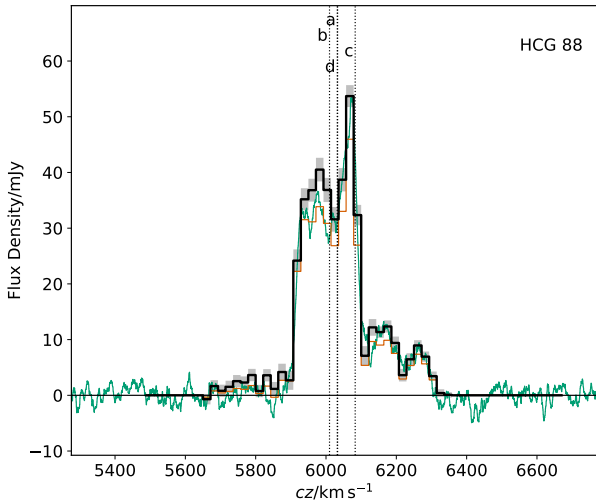


Fig. 60. As in Figure 2.

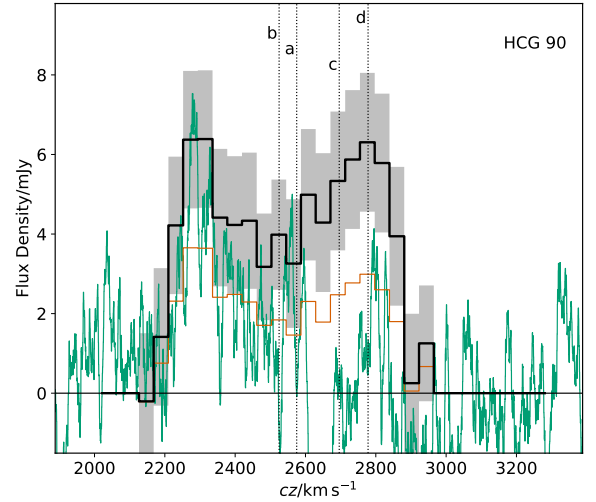


Fig. 62. As in Figure 3.

the emission to a bridge feature. HCG 88d also appears to have an incipient tidal tail on its SE side.

3.31. HCG 90

HCG 90 is an extremely compact configuration of three early-type galaxies and a fourth late-type galaxy about 60 kpc to the north. The VLA observations of the group used a very broad channel width (195 kHz) in order to span the full velocity range of the group and beyond. However, the broad channels cause SoFiA's reliability verification algorithm to fail, as too few sources (spurious plus real) are detected. Therefore, we raised the masking threshold to 5σ in order to eliminate any spurious detections.

We note that HCG 90 appears to be embedded at the centre of a much larger structure containing many tens of galaxies. There are several dwarf galaxies in the vicinity of the core group, some of which could be members (de Carvalho et al. 1997), but which we had chosen to disregard, and instead we focus on the core group, as we have done with other HCGs. With the exception of PGC 198500, which is marginally detected (but excluded due to the higher threshold of the SoFiA mask), these additional members are all undetected in H I and would minimally impact the estimated H I deficiency of the group, owing to their low mass relative to the core members.

SoFiA splits the emission from HCG 90a (the only core member detected) into two halves, which we combine (Figures 61 & 62). No other modification is made to the mask.

3.32. HCG 91

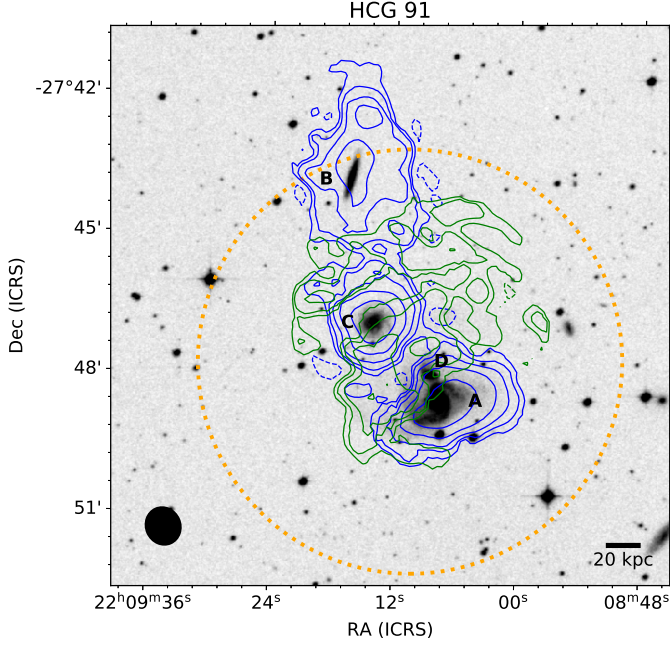


Fig. 63. As in Figure 3, except the background image is POSS *R*-band.

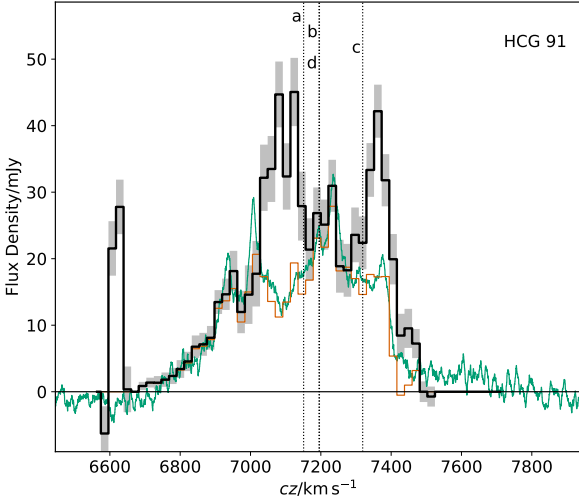


Fig. 64. As in Figure 4.

HCG 91 consists of four disc galaxies (in the redshift range $7100\text{--}7300\text{ km s}^{-1}$) in an almost linear N-S configuration. The H I distribution of this group has been studied in detail before by Vogt et al. (2015). Our analysis is based on a re-reduction of the same data. HCG 91a, b and c are all detected in H I, but HCG 91d is not (Figures 63 & 64). The main tidal feature in the group is a tail originating on the eastern side of HCG 91a and wrapping around to its north side. HCG 91c has a bright and narrow H I distribution, whereas HCG 91b is quite broad (in velocity) reducing its S/N in each channel. There also appears to be a low S/N extended feature between HCG 91b and c, which we separate out as best as possible. Finally, there are three additional detections in the H I separated from the core group by

over 300 kpc. These are PGC 68187, PGC 68161, and a likely spurious detection to the SE for which we could not identify an optical counterpart.

3.33. HCG 92

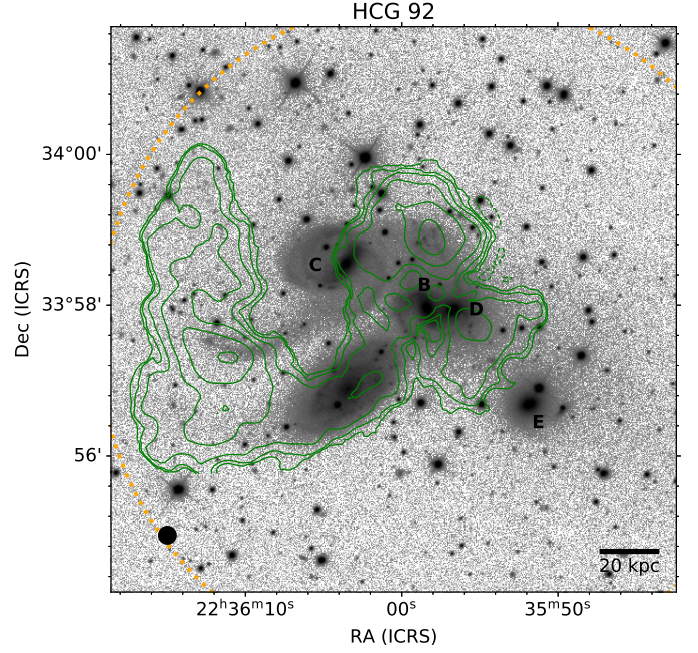


Fig. 65. As in Figure 3.

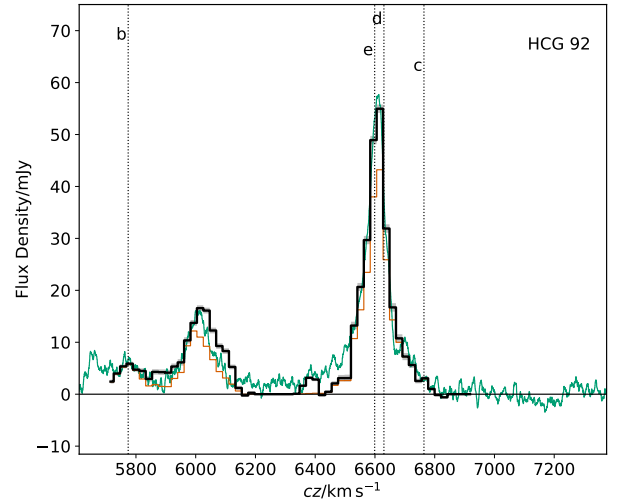


Fig. 66. As in Figure 4.

HCG 92 (or Stephan's Quintet) is an extremely compact configuration of galaxies that exhibits shocks and tidal tails in both neutral and ionised gas. It has been the target of over a hundred papers in IR, optical, UV, and X-ray imaging (e.g. Sulentic et al. 1995, 2001; Gallagher et al. 2001; O'Sullivan et al. 2009; Duc et al. 2018), radio continuum (e.g. van der Hulst & Rots 1981; Nikiel-Wroczyński et al. 2020), and line emission (e.g. Yun et al. 1997; Williams et al. 2002; Lisenfeld et al. 2002; Appleton et al.

2006; Guillard et al. 2012; Konstantopoulos et al. 2014; Duarte Puertas et al. 2019).

The core group is made up of four members, as HCG 92a is a foreground interloper. Although the morphology and kinematics of the H I gas in the group are extremely complex (Williams et al. 2002), for our purposes it is quite straightforward. As discussed in detail by Williams et al. (2002), none of the H I emission is located in the galaxies themselves. The majority is in an enormous L-shaped tail that extends to the east of the group, then there are three separate clouds on the western side of the group (two of which project on top of each other), but these do not coincide with the galaxies (Figures 65 & 66).

To the east of the group we also detect AGC 320272 in H I, however, this dwarf galaxy is ~ 175 kpc from the core group and appears undisturbed in H I. Therefore, we do not consider it as a member. In addition, we detect AGC 321245 about 250 kpc north of the core group, and finally there is a likely spurious detection in the H I cube a similar distance to the NW. We also note that a few central channels of the cube were effectively lost due to inadequate continuum subtraction where the two sub-bands of the observation (just) overlap, however, this does not appear to overlap with any of the aforementioned H I features.

3.34. HCG 93

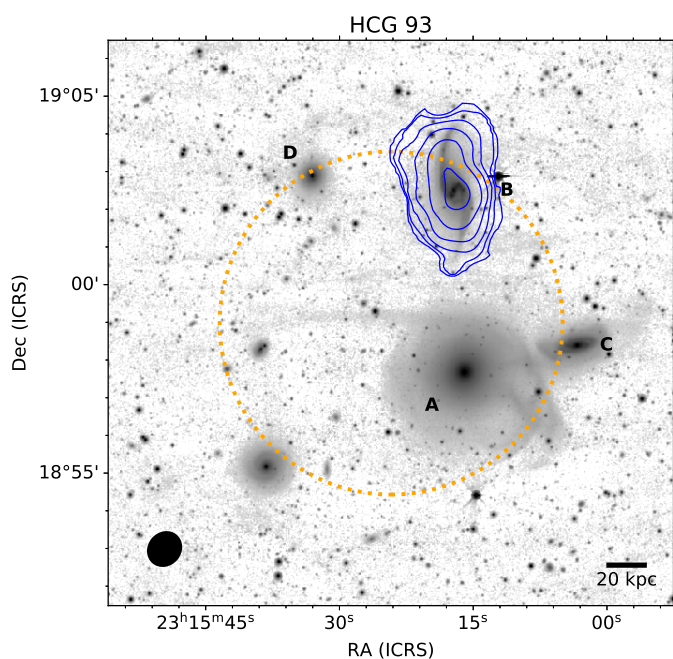


Fig. 67. As in Figure 3.

HCG 93 (projected adjacent to HCG 94, separated by only $\sim 30'$, but by over 6000 km s^{-1}) is made up of three late-type and one elliptical galaxy. In the core group only HCG 93b, a loosely wound spiral, is the only galaxy detected in the VLA H I map. In addition, we also detect three uncatalogued dwarf galaxies in the vicinity of the group, however, these are all separated from the core group by ~ 200 kpc.

The H I of HCG 93b appears quite regular and we do not separate off any tidal features; quite surprising given its optical appearance (Figures 67 & 68). This may in part be the result of the fairly low resolution of the VLA data, however, there is certainly no highly extended H I emission as is typical in gas-bearing galaxies experiencing strong tidal forces.

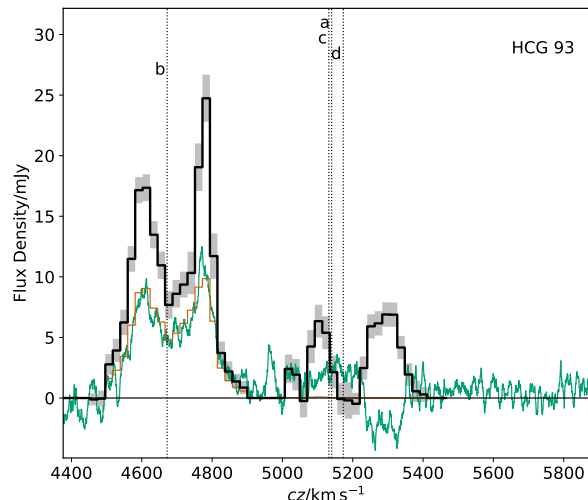


Fig. 68. As in Figure 4.

The first two of the three outlying dwarf galaxies (which we refer to as HCG 93LSB1–3) have clear optical counterparts in the DECaLS images. The third may be spurious as it is the lowest S/N of the three and has no apparent optical counterpart (although this may be hidden by its proximity to a bright star).

3.35. HCG 95

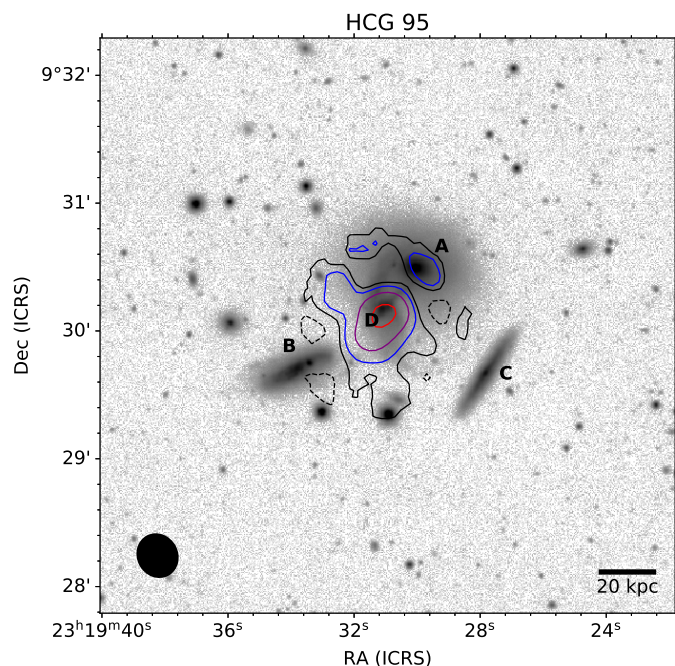


Fig. 69. As in Figure 29.

HCG 95 is a group of three late-type and one elliptical galaxies in the redshift range $11500\text{--}11900 \text{ km s}^{-1}$. Owing to its large distance (160 Mpc) the physical resolution of the VLA data are quite poor (even in CnB configuration). We therefore do not attempt to separate galaxies and extended features in this group. However, we note the detected H I emission is mostly co-spatial

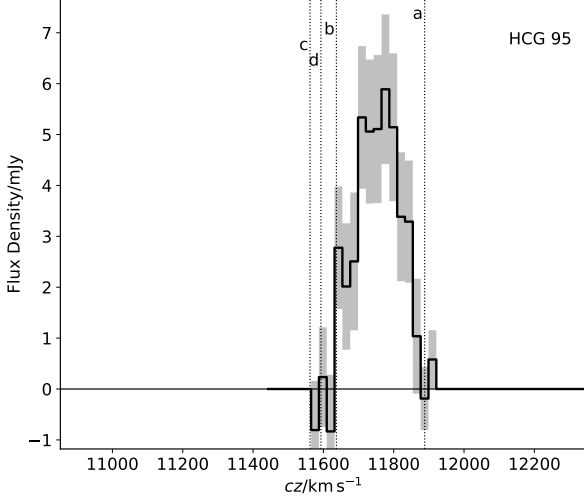


Fig. 70. As in Figure 2.

with HCG 95d, though there does appear to be an extension towards HCG 95a (Figures 69 & 70).

Beyond 125 kpc outside of the core group we detect HCG 95f and HCG 95e in H I. We note that these were not originally classified as HCG members by Hickson (1982) and Hickson et al. (1992), but they were added after deep imaging searching for LSB galaxies (Shi et al. 2017). For consistency with our approach to the other groups we do not consider these as members of the group. We also note that there are slight continuum subtraction artefacts remaining in this H I cube.

3.36. HCG 96

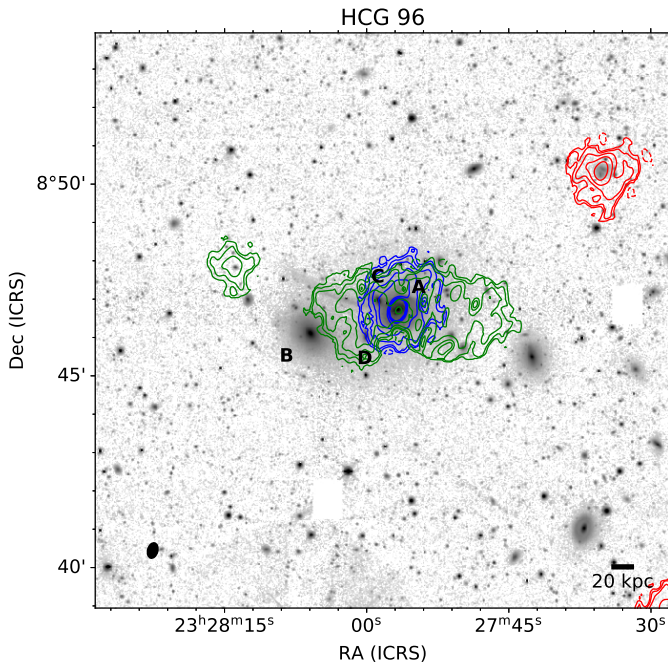


Fig. 71. As in Figure 1.

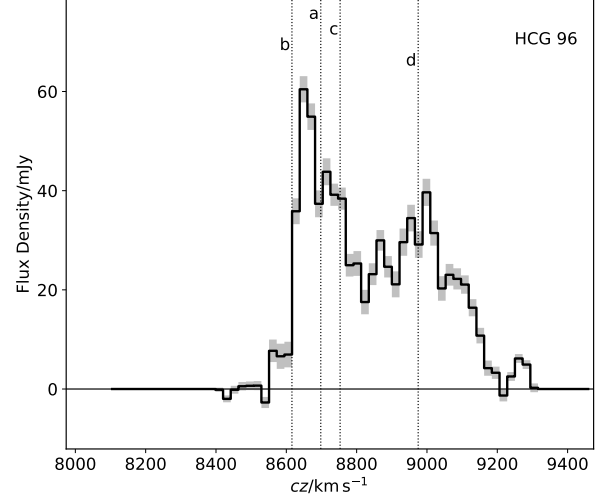


Fig. 72. As in Figure 2.

HCG 96 is a group of three late-type and one elliptical in the redshift range $8600\text{--}9000\text{ km s}^{-1}$, two of which (HCG 96a and c) may be in the process of merging. There is a large extended region of H I emission in the core group that appears to encompass HCG 96a, c, and d (Figures 71 & 72). HCG 96b is undetected. There are also several additional H I detections around the core group. The closest of these is an uncatalogued compact, blue, irregular galaxy GALEX-ASC J232813.78+084750.1 (which we refer to as HCG 96cl1). This object could plausibly be interacting with core group, or could even be a TDG forming from the ongoing major interactions. We therefore consider it as part of the group, but designate it as a tidal feature. The remaining detections outside of the group are GALEXASC J232735.09+085018.2, GALEXASC J232727.99+083853.7, GALEXASC J232714.32+084125.5, PGC 71560, and three likely spurious detections near the edge of the primary beam with no apparent optical counterparts.

Although the extended emission in the core group covers all of HCG 96a, c, and d in projection, all of this emission appears to be associated with HCG 96a. HCG 96d is sufficiently separated in velocity that it would not fall within the most complex region of emission, and we can confidently conclude that it is undetected. In the case of HCG 96c there are clumps in the extended emission which might correspond to the galaxy, however, even if they do, they do not significantly stand out from the surrounding emission and are thus unlikely to be bound to the galaxy. Hence, all the emission in the core group that is not clearly consistent with the rotation of HCG 96a is classified as extended features. The H I in the core group is also complicated by the presence of a strong H I absorption feature in front of the nucleus of HCG 96b.

3.37. HCG 97

HCG 97 consists of five galaxies approximately in the redshift range $6000\text{--}7000\text{ km s}^{-1}$, two ellipticals, two spirals, and one lenticular. Only one of these, HCG 97b, is detected in the VLA H I observations (Figures 73 & 74). However, a number of other objects are detected within the VLA primary beam (WISEA J234701.65-022033.4, LEDA 1092439, PGC 72457,

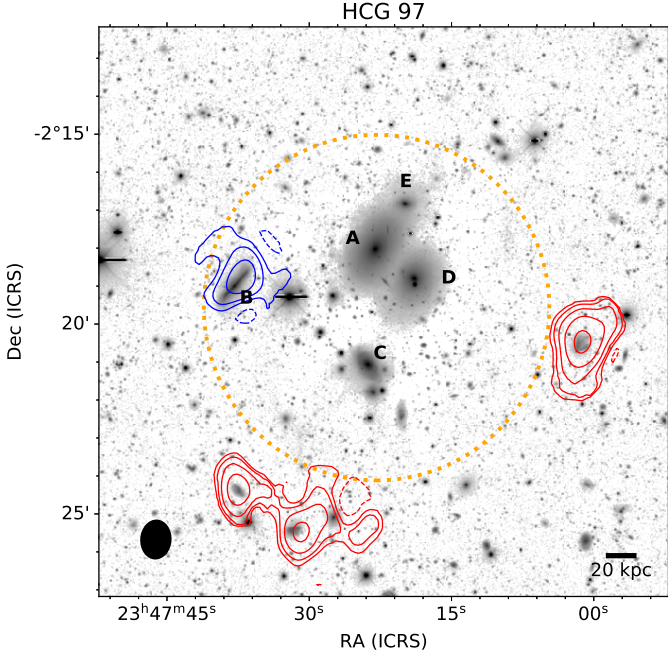


Fig. 73. As in Figure 3.

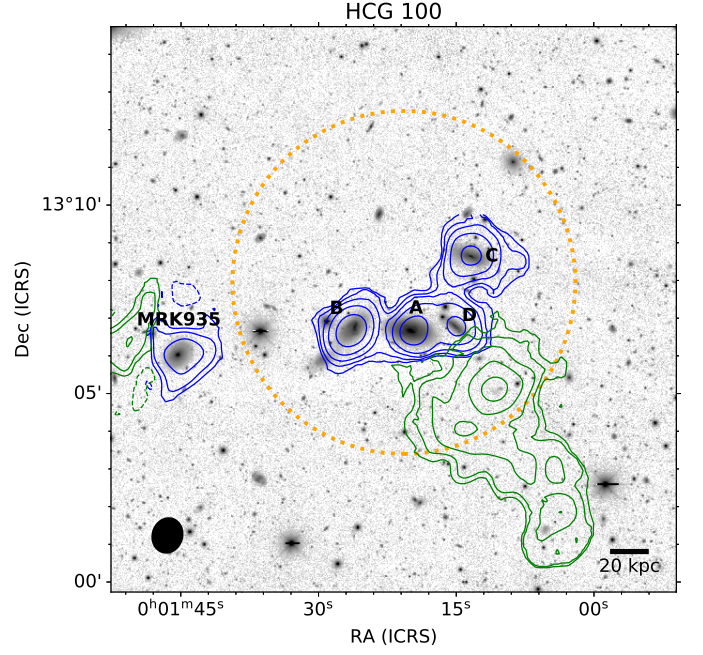


Fig. 75. As in Figure 3.

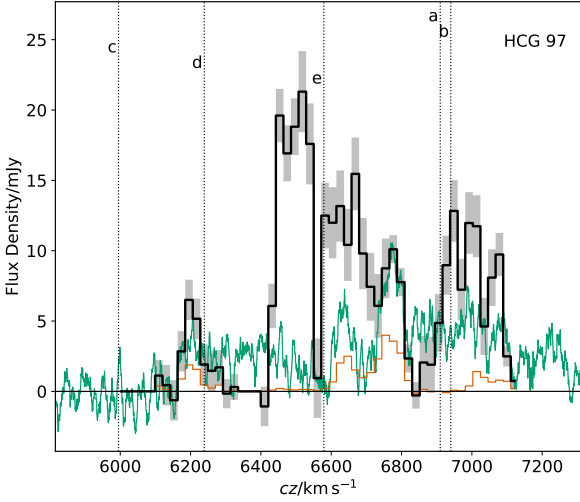


Fig. 74. As in Figure 4.

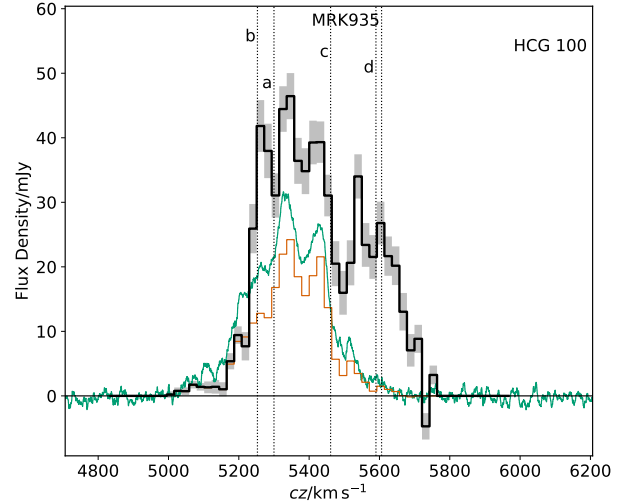


Fig. 76. As in Figure 4.

PGC 3080162, UM 177, PGC 1098512, and PGC 1092963, whose emission is truncated by the edge of the band), between about 100 kpc to 500 kpc away from the core group. The nearest of these lie on the edge of the beam of the GBT observation, and likely contributed some additional flux to the group's H I mass measurement.

HCG 97b is an edge-on spiral and it appears that H I is likely only detected on one side of the galaxy, with the emission from the receding side of the galaxy being too low S/N to be included in the source mask. This indicates that the galaxy is likely disturbed, but it is only marginally resolved in the VLA data.

3.38. HCG 100

HCG 100 is made up of a chain of four late-type galaxies in the redshift range 5200–5600 km s^{−1}. All are detected in H I in the VLA imaging, as well as an enormous extended feature, stretching over 100 kpc to the SW of the core group. At the tip of this tail there is a faint, blue optical counterpart, perhaps indicating the formation of a TDG (e.g. de Mello et al. 2012). In addition, we detect MRK 935 about 85 kpc east of the core group.⁶ The H I in this galaxy appears heavily perturbed and it is likely interacting with the core group and we therefore consider it a

⁶ We note that there are conflicting redshift measurements for MRK 935, however, the H I detection is consistent with $cz_{\odot} = 5606$ km s^{−1} (Petrosian et al. 2007).

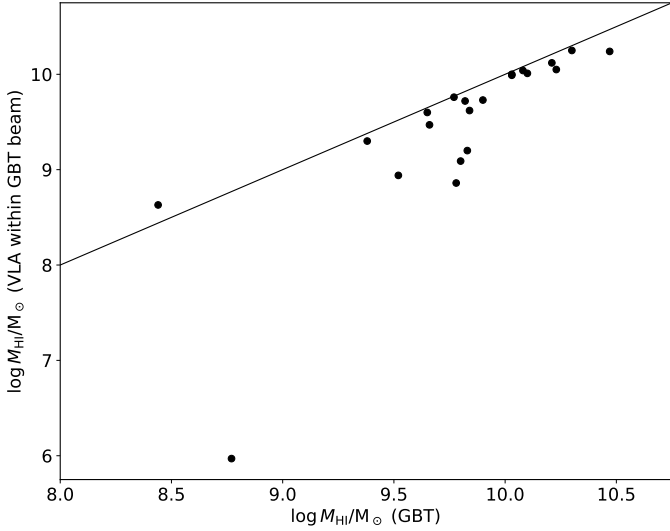


Fig. 77. H I mass of HCGs measured by the GBT (x-axis) and measured by the VLA with spatial weighting to match the falloff in sensitivity corresponding to the GBT beam (y-axis). The solid line indicates equality of the two. Note that the scale is not the same of both axes.

member. Further to the SE we also detect H I in NGC 7810 and AGC 105092.

We do not attempt to separate the four core galaxies from each other. Their optical discs almost overlap, and given that they are spread over only $\sim 400 \text{ km s}^{-1}$ it is not possible to reliably separate them at the resolution of the VLA data. However, the majority of the emission in extended features appears to be in the SE tail, which is separated as a distinct feature. Although the detection of MRK 935 is quite low S/N we attempt to separate this into emission from the galaxy itself and extended emission. However, the faintness of this object (in H I) mean that it has little bearing of the overall ratio of disc versus extended emission in the group.

4. Results

In this section we present the global results for the H I content of HCGs based on aggregating the results for individual groups from the previous section. First we compare the VLA measurements to those from the GBT, and then proceed calculate the H I deficiency of each HCG.

4.1. Discrepancies between single-dish and VLA fluxes

As shown in Figure 77 the vast majority of the VLA observations result in total fluxes (after weighting for the GBT beam response) that are just marginally below those observed with the GBT. This is expected, as in general an interferometer resolves out some extended emission and therefore does not recover the full flux seen with a single dish. However, there are a few points which require further investigation: a) the single point above the line of equality, b) the group of four points about 0.5 dex below the line, and c) HCG 30 which is about 2 dex below the line.

The first of these is formally impossible as an interferometer cannot detect more flux than a single dish, and would therefore normally point to a calibration, pointing, or continuum subtraction problem. This point corresponds to HCG 90. As can be seen in Figure 61, only HCG 90a is detected in the VLA map and this galaxy lies outside the HPBW of the GBT observation. There-

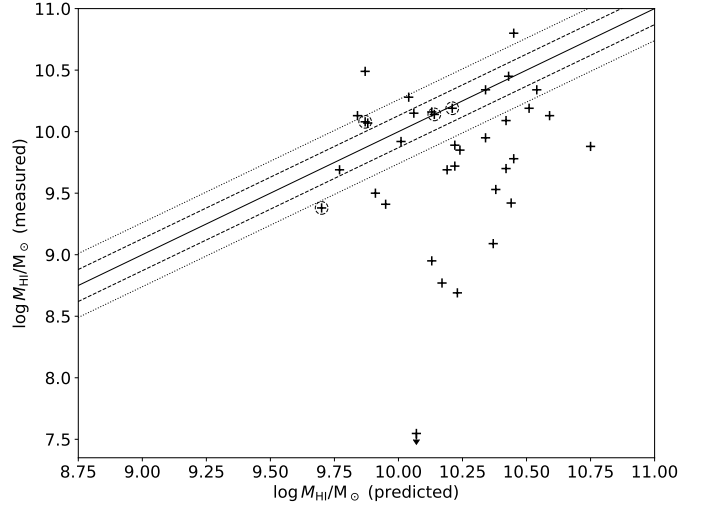


Fig. 78. Measured versus predicted (with the Jones et al. (2018) L_B – M_{HI} scaling relation) H I masses of HCGs. All measured H I masses are those from the VLA data, except for HCG 30 and 37, which use the GBT measurements. Points circled with black dashed lines are triplets. The solid black line indicates equality and the dashed and dotted lines indicate 1σ and 2σ scatters from the Jones et al. (2018) relation (for a single galaxy). HCG 62 was undetected with the VLA (and has no GBT observation) and is marked as an upper limit.

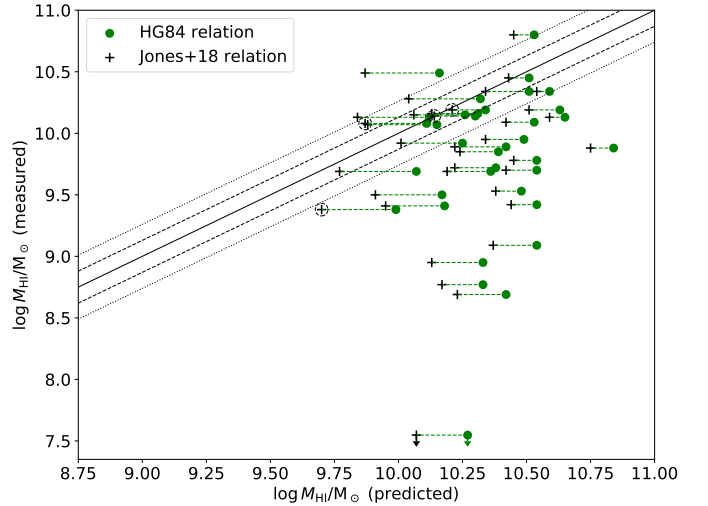


Fig. 79. As for Figure 78, except now marked with green circles are the predicted H I masses using the Haynes & Giovanelli (1984) L_B – M_{HI} scaling relation. In general this relation predicts significantly higher H I masses than those from the equivalent Jones et al. (2018) relation.

fore, the comparison between the VLA and GBT fluxes will be extremely sensitive to exact nature of our (approximate) weighting for the GBT primary beam response. Furthermore, there is a strong H I absorption feature at the centre of HCG 90a, which appears to impact the GBT spectrum more strongly than the VLA spectrum (Figure 62).

The second case, the four groups with about 0.5 dex lower VLA fluxes than GBT fluxes, also requires explanation. These groups are HCGs 15, 37, 58, and 97. HCG 97 is another case similar to HCG 90, where much of the H I emission occurs near or beyond the edge of the GBT primary beam, and therefore the comparison between the VLA and GBT spectra is likely to be unreliable (Figures 73 & 74). However, the spectra do also show regions where emission is detected by the GBT, but not at all

Table 2. H I deficiency of HCGs

HCG	$\log M_{\text{HI,VLA}}$ [M_{\odot}]	$\log M_{\text{HI,GBT}}$ [M_{\odot}]	$\log M_{\text{HI,pred}}$ [M_{\odot}]	H I-def. (VLA)	H I-def. (GBT)	$\log M_{\text{HI,gals}}$ [M_{\odot}]	$\log M_{\text{HI,exfs}}$ [M_{\odot}]	f_{exfs}	H I Phase
2‡	10.08 ± 0.04		9.87 ± 0.12	-0.21		10.06	8.66	0.04	1
7	9.73 ± 0.05	9.65	10.22 ± 0.16	0.49	0.57	9.73		0.0	1
10	9.85 ± 0.04	9.77	10.24 ± 0.12	0.39	0.47	9.85		0.0	1
15	9.09 ± 0.07	9.52	10.37 ± 0.09	1.28	0.85	9.09		0.0	3c
16	10.34 ± 0.05	10.08	10.34 ± 0.09	-0.0	0.26	10.11	9.95	0.41	2
19‡	9.39 ± 0.05		9.7 ± 0.13	0.31		9.28	8.72	0.22	1
22	9.41 ± 0.04		9.95 ± 0.15	0.54		9.41		0.0	3c
23	10.13 ± 0.05	10.03	9.84 ± 0.12	-0.29	-0.19	10.05	9.37	0.17	1
25	10.15 ± 0.05	10.1	10.06 ± 0.13	-0.09	-0.04	10.1	9.23	0.12	1
26	10.27 ± 0.05	10.47	10.04 ± 0.11	-0.23	-0.43	10.19	9.49	0.17	1
30	< 7.78	8.77	10.17 ± 0.13	> 2.39	1.4				3a
31	10.17 ± 0.05	10.22	10.13 ± 0.19	-0.04	-0.09	9.74	9.96	0.63	2
33	10.07 ± 0.06		9.88 ± 0.12	-0.19		10.02	9.1	0.11	3c
37	< 8.35	9.78	10.45 ± 0.14	> 2.1	0.67				3a
38‡	10.14 ± 0.05		10.14 ± 0.12	-0.0					
40	9.69 ± 0.07	9.84	10.42 ± 0.12	0.73	0.58	9.5	9.25	0.36	2
47	9.69 ± 0.05		10.19 ± 0.13	0.5		9.41	9.37	0.48	2
48†	8.85 ± 0.06	8.78	9.44 ± 0.17	0.59	0.66				
49	10.49 ± 0.04		9.87 ± 0.11	-0.62					
54	9.25 ± 0.05		8.99 ± 0.17	-0.26					
56	9.89 ± 0.04		10.22 ± 0.11	0.33		9.89		0.0	3c
57	9.88 ± 0.05		10.75 ± 0.09	0.87					
58	10.19 ± 0.04	9.83	10.51 ± 0.1	0.32	0.68	9.78	9.98	0.61	2
59	9.69 ± 0.05		9.77 ± 0.13	0.08		9.61	8.92	0.17	1
61‡	10.2 ± 0.04		10.21 ± 0.13	0.01		9.13	10.16	0.91	3a
62	< 7.54		10.07 ± 0.12	> 2.53					3a
68	9.95 ± 0.04	9.83	10.34 ± 0.11	0.39	0.51	9.95	7.4	0.0	3c
71	10.8 ± 0.05		10.45 ± 0.14	-0.35		10.59	10.39	0.39	2
79	9.49 ± 0.05	9.66	9.91 ± 0.12	0.42	0.25	9.26	9.11	0.42	2
88	10.08 ± 0.05	10.02	10.42 ± 0.11	0.34	0.4	10.08	8.4	0.02	1
90	8.94 ± 0.06	8.43	10.13 ± 0.1	1.19	1.7	8.94		0.0	3c
91	10.34 ± 0.06	10.3	10.54 ± 0.15	0.2	0.24	10.21	9.76	0.26	2
92	10.13 ± 0.04	10.23	10.59 ± 0.11	0.46	0.36		10.13	1.0	3a
93	9.53 ± 0.04	9.38	10.38 ± 0.12	0.85	1.0	9.53		0.0	3c
95	9.42 ± 0.09		10.44 ± 0.12	1.02					
96	10.45 ± 0.05		10.43 ± 0.14	-0.02		9.93	10.29	0.69	2
97	8.68 ± 0.1	9.8	10.23 ± 0.1	1.55	0.43	8.68		0.0	3c
100	9.92 ± 0.05	9.89	10.01 ± 0.11	0.09	0.12	9.64	9.59	0.47	2

Notes. Columns: (1) HCG ID number, (2) total H I mass from the VLA observations with uncertainties approximated as $\sigma_{M_{\text{HI}}} = 235600 \left(\frac{D}{\text{Mpc}} \right)^2 \times 3 \frac{\sigma_{\text{rms}}}{\text{Jy}} \times 100 \text{ km s}^{-1}$, combined with an assumed 10% uncertainty in absolute flux calibration (distance uncertainties are neglected), (3) total H I mass from the GBT observations (Borthakur et al. 2010), (4) predicted H I mass based on B-band luminosity (Jones et al. 2018), (5 & 6) H I deficiency of the entire group from the VLA and GBT mass measurements, respectively, (7) combined H I mass of all member galaxies, (8) combined H I mass of all extended features in the group, (9) fraction of total H I mass in extended features, (10) H I morphological classification. † Pair or false group. ‡ Triplet.

with the VLA. This may be a sign of diffuse H I emission that was resolved out by the VLA.

The comparison of the VLA and GBT spectra (Figure 8) for HCG 15 indicates that a considerable fraction of the H I emission in the GBT spectrum is undetected with the VLA. We also note that the VLA spectrum presented here differs strongly from that presented by Borthakur et al. (2010), where even HCG 15f is not detected. The high rms noise of the VLA data relative to the signals in the GBT spectrum, might prevent them from being included in the source mask. Alternatively, these could be diffuse features that were resolved out by the VLA. We also note that the two highest peaks in the GBT spectrum (aside from HCG 15f) do not correspond to the redshifts of any of the group members,

which could mean that they are additional LSB members, H I-only features, or spurious in some way.

In the cases of HCG 30 and 37, there is no H I emission detected in the group cores by the VLA (Figures 22 & 28), but in the GBT spectra there is broad ($\sim 1000 \text{ km s}^{-1}$ wide), faint emission that might indicate the presence of a diffuse H I component that the VLA is unable to detect (Borthakur et al. 2010). These two groups are the most clear examples of this phenomena that we identified, with the other possibility being HCG 97. In all other cases (except HCG 15) the spectra from the VLA and the GBT are broadly consistent.

Two other groups warrant mention for their minor mismatches in their GBT and VLA spectra, HCG 26 and 79. The

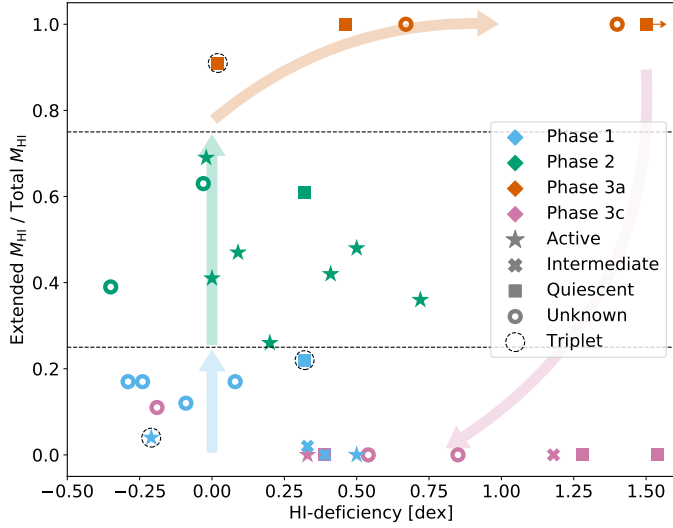


Fig. 80. H I deficiencies and extended H I emission fraction for each (resolved) group in the sample. The colour of each point indicates its H I morphological phase: blue for 1, green for 2, orange for 3a, and pink for 3c. The marker shape indicates the IR classification (Zucker et al. 2016) of each group: stars for groups dominated by IR active galaxies, crosses for groups not dominated by either active or quiescent (or transition) galaxies, squares for groups dominated by quiescent (or transition) galaxies, and rings for groups with too many members without IR classifications. Markers enclosed in a dashed black circle correspond to triplets. The lone upper limit plotted in the top-right corner corresponds to HCG 62 that was entirely undetected in H I with the VLA and has no GBT observation. The horizontal dashed lines indicate 25% and 75% extended emission. These thresholds entirely determine which groups are classified as Phase 2 or 3a. Phase 1 and 3c are distinguished from each other based on the number of galaxies detected in H I (Section 5.1). The shaded arrows indicate our proposed evolutionary path of groups through this parameter space.

spectral profile of HCG 26 in the VLA data matches closely with that from the GBT data, however, it is consistently lower (Figure 20). As the profile is so similar this likely indicates a slight calibration problem with one or both of these observations, rather than the presence of diffuse emission. For HCG 79 an entire emission feature appears to be absent from the VLA spectrum when compared to that of the GBT (Figure 58). At present there is not a clear explanation for this mismatch. It seems unlikely that this feature would be too low S/N to be detected, meaning it could be a diffuse feature resolved out by the VLA, an artefact in the GBT data, or a problem with the continuum subtraction of the VLA data. However, we were unable to identify the root cause.

Aside from the few cases discussed above, the GBT flux is well recovered by the VLA observations. Therefore, as all our targets have VLA data, but not all have GBT data, we use the H I deficiency of each group determined from the VLA data in most of our subsequent analysis. Switching to the GBT observations would make only marginal differences for all but a handful of groups, and in most of those cases would lead to a worse estimate (e.g. because of blended emission from non-members), not an improvement. The exception are HCG 30 and 37 for which we use the GBT measurements, as these are undetected with the VLA.

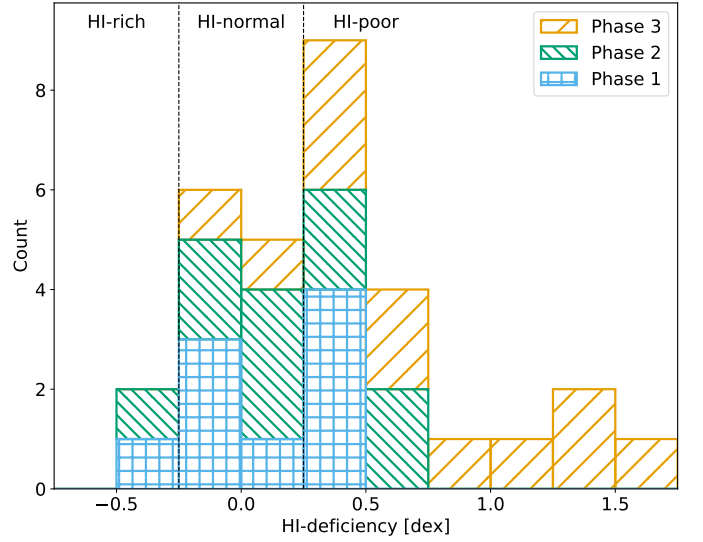


Fig. 81. Histogram of H I deficiencies of HCGs. The three phases are shown individually by differently hatched bars. The vertical black dashed lines indicate approximately the typical 1σ uncertainty (away from zero) in the measure of H I deficiency for an individual galaxy (Jones et al. 2018). Note that HCG 62 is not included as there is only an upper lower limit on its H I deficiency.

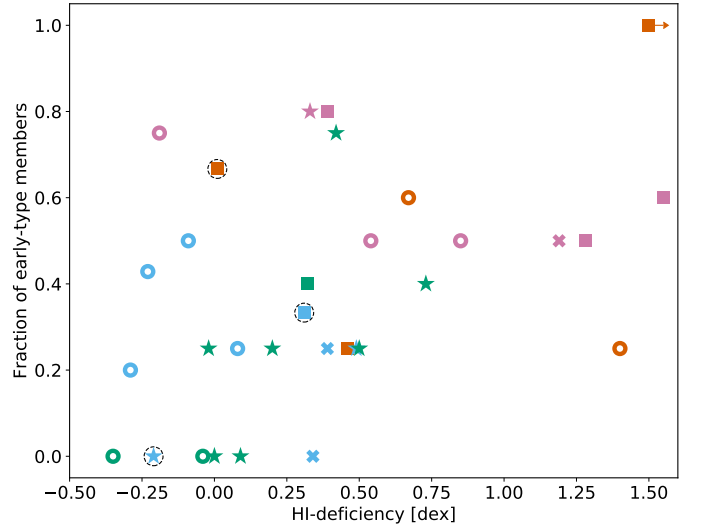


Fig. 82. H I deficiencies of HCGs versus the fraction of early-type members. In this case early-types are defined as lenticular or elliptical. The markers follow the same scheme as in Figure 80.

4.2. H I deficiency of HCGs

Huchtmeier (1997) and Verdes-Montenegro et al. (2001) found that the vast majority of HCGs were highly H I-deficient, motivating them to ask the question “where is the neutral atomic gas in HCGs?” The distribution of observed versus predicted H I masses is shown in Figure 78. We too find that many HCGs have significantly lower H I masses than would be expected for non-interacting galaxies, while very few are significantly rich in H I. We also see that triplets (circled with black dashed lines in Figure 78) appear to follow the same distribution as groups with more members. However, there are just four triplets in the sample.

We define H I deficiency (as in Haynes & Giovanelli 1984) to be the logarithmic decrement between the predicted and ob-

served H I mass, that is $H_{I\text{-def}} = \log M_{H_{I,\text{pred}}} - \log M_{H_{I,\text{obs}}}$, where the predicted mass is found from the B-band luminosity and the scaling relation of Jones et al. (2018), measured based on isolated galaxies in the AMIGA (Analysis of the interstellar Medium of Isolated GALaxies; Verdes-Montenegro et al. 2005b) sample. The AMIGA sample offers a benchmark of H I content of galaxies in the (near) absence of interactions. It is also an optically selected sample (as are HCGs) rather than an H I-selected sample. Thus, the Jones et al. (2018) relations offer a well-suited metric for HCGs, whereas other scaling relations in the literature (e.g. Toribio et al. 2011; Brown et al. 2017) would be less appropriate for this particular use case and could introduce a bias in the measures of H I-deficiency.

We note, however, that no scaling relation will function perfectly as intended in a compact group environment. The myriad of ongoing interactions, starbursts, shocks etc. in these groups is bound to influence the B-band luminosities of the galaxies and complicate the use of this scaling relation. We chose to adopt B-band luminosity as the predictor for H I mass as the alternative, optical diameter (Jones et al. 2018), can be extremely uncertain in systems where tidal effects are significant. Although also affected by tidal interactions, B-band luminosity is usually dominated by the bulge and is therefore expected to be less severely impacted in most cases. Even so, we caution the reader that the uncertainty estimates on the predicted $M_{H_{I}}$ values in Tables 2 & C.1 are based on the scatter of values for isolated galaxies and are likely underestimate the scale of the uncertainties for HCG galaxies.

The B-band magnitudes (and morphological types) of the member galaxies (Table C.1) for use with this scaling relation are taken from Hickson et al. (1989). In cases where we have identified new group members these values were taken from the HyperLeda database (Makarov et al. 2014). To perform detailed photometry Hickson et al. (1989) imaged HCG galaxies with the Canada-France-Hawaii telescope and overlapping galaxies were separated. For pairs the separation was performed by slicing the image at the nuclei of each galaxy and proportioning the light in between them based on the magnitude of the non-overlapping side of each galaxy. For high multiplicity blends the light in overlapping isophotes was divided amongst all the galaxies based on their magnitudes inside their non-overlapping isophotes. Finally, Hickson et al. (1989) corrected these values for internal and Galactic extinction following de Vaucouleurs et al. (1976).

For uniformity, we use the same relation for all galaxies with no consideration of morphological type. Although Jones et al. (2018) did also fit separate relations for early, late, and very late types, these relations were considerably more uncertain than the main relation, and Jones et al. (2018) largely advised against their use. We note, however, that this may lead to a slight bias towards higher H I deficiencies for groups dominated by early-types. However, in practice these are mostly Phase 3 groups that mostly have high H I deficiencies, regardless of the exact relation used. In addition, as these groups are likely more evolved than those dominated by late-types, and as we are interested in the comparison of their original and current H I contents, it is uncertain what morphological types should be used for them in the event that a morphology-dependent relation were to be used, further supporting the choice to ignore morphological type when estimating H I deficiency.

We find a similar result to Verdes-Montenegro et al. (2001), that the mean deficiency is 0.34 dex. We also note that the median deficiency is a fairer estimate of what is typical of the population, both because H I deficiency is a non-linear quantity and because it allows for the inclusion of upper limits from unde-

tected groups. This value is 0.33 dex, almost identical to the mean value.

This close agreement between the average H I deficiency that we find and that found by Verdes-Montenegro et al. (2001), 0.40 dex, disguises some fundamental differences between the results of that work and this work. The first is that the Jones et al. (2018) L_B - $M_{H_{I}}$ scaling relation provides a less biased prediction of the H I mass of a galaxy than the equivalent relation from Haynes & Giovanelli (1984). As explained in that work, this is primarily driven by the improved fitting methodology employed by Jones et al. (2018) and also, to a lesser extent, because of the larger and more morphologically diverse sample used. This results in predicted H I masses being significantly lower (on average) for the same groups compared to Haynes & Giovanelli (1984), as shown in Figure 79. However, even our predicted H I masses based on the Haynes & Giovanelli (1984) differ from those of Verdes-Montenegro et al. (2001), likely a result of changes in group membership and the use of a corrected form of the Haynes & Giovanelli (1984) relation (see Appendix C of Jones et al. 2018). In addition, our measurements of the H I mass of HCGs (after correcting for the different distance estimates used) are typically about 0.1 dex larger than those of Verdes-Montenegro et al. (2001). This is likely due to the fact that the single-dish observations of many HCGs had primary beams that were either too small to include all the H I flux from the group, or the flux from the outlying regions of a group was down weighted by the declining beam response. Serendipitously, these effects appear to have approximately cancelled each other out, resulting in a very similar average H I deficiency being calculated.

5. Discussion

In this section we discuss how groups are classified based on their H I and IR morphology. In addition we assess whether the hypothesis that H I deficiency should act as a proxy for morphological phase is supported by the observations that we have presented.

5.1. H I morphological classification scheme

Verdes-Montenegro et al. (2001) first proposed an evolutionary sequence for HCGs based on their H I morphology. One of the goals of this work is to compare that morphological sequence to the H I deficiencies of HCGs. With the uniform analysis of all available VLA observations of HCGs we have now greatly expanded the sample for which this comparison is possible, while the H I deficiency has been revised for all these groups based on a more self-consistent definition (Jones et al. 2018), as described above. However, before proceeding with this comparison, we first make slight adjustments to the Verdes-Montenegro et al. (2001) scheme based on our expanded findings of the H I morphology of our sample of HCGs.

The original scheme split groups up into three main categories, phases 1, 2, and 3. Phase 1 groups were those where the majority (70% or more) of the detected H I was in features associated with the galaxies themselves. Phase 2 groups were those where a significant fraction (30-60%) of the detected H I was in extended features. Finally, Phase 3 were those groups that were either undetected in H I or whose H I was predominantly (60% or more) in extended features, rather than in the galaxies themselves. The prototypical examples of each phase are HCGs 88, 16, and 92, in order of increasing evolutionary phase.

The first modification is very minor, and is to set the thresholds for being classified a Phase 2 or 3 as 25% and 75% of the

detected H I in extended features, respectively. These are slight a decrease and increase compared to (Verdes-Montenegro et al. 2001), respectively, and a reflection of the apparent breaks between these classes in our data. In particular, the morphology of groups like HCG 31 and 58 (Figures 23 & 45) seem to fit best into Phase 2, as they have both significant extended H I features, but also clear concentration remaining in the galactic discs. However, with the new analysis presented here and the original classification boundaries, these would have been classified as Phase 3. We note that the exact location of these thresholds is somewhat subjective, and there are cases where a particular HCG is essentially on the threshold and could be classified in one of two ways (e.g. HCG 19 or 91).

The second modification is more significant and concerns distinguishing groups which are Phase 1 from those that are Phase 3. Verdes-Montenegro et al. (2001) split the Phase 3 classification into two subcategories, 3a and 3b. In that scheme, 3a represented groups with either very high fractions of H I emission in extended features or no H I detection at all. We keep this subcategory essentially unchanged (except the threshold mentioned above). Phase 3b was used to denote groups that appeared to be evolving within a common H I envelope. However, improved observations and analyses (e.g. Verdes-Montenegro et al. 2002) have demonstrated that no groups (with the possible exception of HCG 49) convincingly fit this scenario, and thus the classification is no longer required. In this work we add a new designation, Phase 3c, to indicate groups that would be classified as Phase 1, but where only a single galaxy is detected in H I. There are a large number of groups where only one member of the group is detected in H I, for example, HCGs 15, 22, 33, 48, 56, 68, 90, 93, 97. The detected galaxy is always a late-type, while the remaining group members are typically dominated by early-types. In at least some, if not all, of these cases it is likely that this lone detection is a recent addition to the group, and effectively leads to a rejuvenation of the H I content of the group. Therefore, these groups are likely in a late stage of their evolution, but have recently gained a new member, hence the classification as Phase 3.

We note that the possibility of new members is not limited to Phase 3 groups. For example, Jones et al. (2019) found that HCG 16 has a recent addition to the group that is partly responsible for its extreme H I morphology (Figure 9). However, in most Phase 1 and 2 groups it would be difficult to identify new members as these groups already typically host several members with normal H I reservoirs. Indeed in Phase 1 it is not clear if the concept of a new member even has much meaning, as the lack of tidal features implies that the galaxies only recently entered into a compact configuration. In the case of Phase 3 groups, however, the incorporation of a new H I-bearing member is striking as these are clear outliers both in terms of their H I content and morphology.

As noted by Martinez-Badenes et al. (2012) the abundance of lenticular galaxies increases with H I phase, with Phase 3a groups being ~30% lenticulars, compared to ~10% in Phase 2 groups. As has been argued previously (Sulentic et al. 2001; Verdes-Montenegro et al. 2001; Bekki & Couch 2011) this increase in abundance of lenticulars is likely the result of spirals being stripped and the increase in their abundance from Phase 2 to 3 is an indication that the latter phase is more evolved. To estimate the abundance of lenticulars in Phase 3c we deducted one member per group (i.e. removing the assumed recent addition) before calculation the fraction, which resulted in a value of ~30%, supporting the idea that these are also evolved groups, just with one new (gas-rich) member.

The diffuse light seen in Phase 3c groups also supports the idea that these are evolved groups. HCG 90 is an extreme case where over a third of its total light is in a diffuse form (White et al. 2003). In HCG 22 the DECaLS images show clear shells and arcs around HCG 22b, signs of past interactions, and potentially even more extended (and extremely faint) features to the NW. HCG 93a also shows an extraordinary complex of diffuse features, and signs of similar (though less impressive) diffuse features are evident in all Phase 3c groups with DECaLS imaging. We are therefore confident that these are all evolved systems that have simply gained a new, gas-rich member.

In summary, our classification scheme is as follows:

- Phase 1: $f_{\text{exfs}} < 0.25$ and $N_{\text{det}} > 1$
- Phase 2: $0.25 < f_{\text{exfs}} < 0.75$
- Phase 3a: $f_{\text{exfs}} > 0.75$ and/or $N_{\text{det}} = 0$
- Phase 3c: $f_{\text{exfs}} < 0.25$ and $N_{\text{det}} = 1$

The fraction of H I emission in extended features, f_{exfs} , is the fraction of the total H I emission in each group that was assigned as an extended feature (e.g. a gas tail or bridge) in Section 3. N_{det} is the number of galaxies in each group that were detected in resolved H I imaging.

Figure 82 shows the early-type fraction of group members against the H I deficiency of each group. Although there is no simple correspondence between the two, we see that almost all groups classified as either Phase 3a or 3c have 50% or more of their members as early-type galaxies, and the reverse is true for Phases 1 and 2, even though no explicit reference to the morphological type of members is made in the classification scheme above. In general the Phase 1 and 2 HCGs are towards the lower-left corner of this figure (low H I deficiencies and few early-type members). The H I deficiencies of the Phase 3 HCGs cover a broad range (extending to much higher deficiency values than the Phase 1 and 2 groups), but these groups are confined almost exclusively to the top half of the plot. This figure thus supports the notion that the H I evolutionary sequence above does in some way correspond to the temporal evolution of HCGs under the assumption that interactions in these groups drive morphological change (e.g. Cluver et al. 2013; Zucker et al. 2016; Lisenfeld et al. 2017).

The classification of each group is written in Table 2 and plotted in Figure 80. Figure 81 show the histogram of the H I deficiencies of all HCGs in our sample and split into the three phases. We see that the Phase 1 groups and the Phase 2 groups have a very similar distribution of H I deficiencies, with the typical value being just marginally deficient. The Phase 3 groups extend from this range to H I deficiencies of about 1.5 dex, and two groups are entirely undetected and have only limits on their H I deficiencies. These findings are discussed further in Section 5.4.

5.2. Comparison with IR activity

In addition to highlighting the morphological phase and H I deficiency of HCGs, Figure 80 also shows the IR classification of Zucker et al. (2016) for each HCG. Star symbols indicate groups where more than 50% of the member galaxies are classified as IR active, crosses indicate groups with no dominant classification, squares indicate groups where more than 50% of members are classified as quiescent or ‘canyon’ (IR transition) galaxies, and rings indicate groups where too many galaxies are missing IR classifications in Zucker et al. (2016) for them to be conclusively assigned to any of the three other categories.

Curiously there is not a strong correspondence between the H I morphology and H I deficiency, and the IR classifications. The clearest trend is that there are almost no groups dominated by quiescent galaxies in Phase 2. There is some correlation between galaxies being H I-rich and those that are IR active (Table C.1), but there are also numerous cases of active galaxies that are undetected in H I, as well as quiescent or cation galaxies that have relatively normal H I reservoirs. We note that these results are somewhat at odds with Walker et al. (2016) who find a stronger correlation between the $g - r$ colours of galaxies in compact groups and the global H I content of the groups. However, the finding that there are several galaxies that appear to strongly deviate from the expected correlation between activity and gas content, is in common with that work. We also note that by defining H I content in terms of M_{HI}/M_* , rather than H I deficiency, Walker et al. (2016) likely incurred a considerable bias, as lower stellar mass galaxies in the field are expected to be more H I-rich (by that metric) as well as later morphological type (e.g. Huang et al. 2012).

We find that the majority of the IR active groups are actually those classified as Phase 2 by H I morphology, not those in Phase 1 (although nearly half of the Phase 1 groups are unclassified). This may indicate that the ongoing interactions that lead to large amounts of H I being spread throughout the IGrM more or less ensure that the participating galaxies will be actively forming stars. However, it should also be noted that some of the Phase 1 groups with the richest H I contents are not classified as active, for example, HCG 23. Thus, provided a group is not strongly H I-deficient, the connection between H I and IR classification appears to be more closely related to morphology of the group than to the exact quantity of neutral gas that is available.

There are some groups that are relatively H I-deficient (e.g. HCGs 7, 40) yet are still IR active. Both HCG 7 and HCG 40 contain a mixture of quiescent and active galaxies (though active galaxies dominate). In all cases the quiescent galaxy(ies) are undetected in H I, immediately raising the H I-deficiency of the group. However, in some cases the active galaxies are also H I-deficient themselves. Although we caution against over interpreting the H I-deficiencies of individual galaxies (which are only expected, in ideal circumstances, to be accurate to 0.2 dex), some of these groups may be in the process of losing their H I gas (potentially accelerated by interactions) but have not yet lost their molecular gas. Thus, interactions are still able to promote elevated levels of star formation activity. Figure 1 of Lisenfeld et al. (2017) shows that IR activity and molecular gas richness are highly correlated in HCGs. Furthermore, Martínez-Badenes et al. (2012) argue that the ongoing tidal interactions in HCGs might also enhance the efficiency of the conversion from H I to H₂. All of the active galaxies in HCGs 7 and 40 have significant molecular gas reservoirs, typically $M_{\text{H}_2}/M_* > 0.1$, which is the threshold where galaxies typically appear to transition from active to quiescent (Lisenfeld et al. 2017). H I is generally much more loosely bound than molecular gas and is therefore lost first, meaning that H I-poor galaxies may still be quite H₂-rich and actively forming stars. However, this is presumably an unsustainable situation as they will rapidly deplete or disperse their molecular gas reservoirs.

Phase 3 groups are mostly classified as quiescent (or unclassified), although there is one example of an IR active Phase 3 group, HCG 56, which is a rather peculiar group containing mostly lenticular galaxies. This finding that Phase 3c groups are often quiescent reinforces our conclusion that most groups with a sole H I detection are evolved groups (regardless of the value of their H I deficiency).

5.3. Evidence for a diffuse H I component

Borthakur et al. (2010) compared the spectra of HCGs from GBT and VLA observations and raised the possibility that, in some groups, flux missed by the VLA observations could be in the form of a diffuse H I component of the IGrM. In this work we have re-reduced all of the VLA observations which Borthakur et al. (2010) compared to and have attempted to recover as much (extended) flux as possible, using both multi-scale clean (which was not widely used when the original reduction was performed) for imaging and SoFiA for masking. As discussed in Section 4.1 the vast majority of our VLA spectra agree remarkably well with the GBT spectra, with their slight discrepancies likely arising from small differences in calibration or minor (undetected) extensions of high column density features. In most groups there is thus little evidence for a significant diffuse H I component of the IGrM.

Having said this, there are some notable exceptions. As mentioned in Section 4.1, HCGs 30, 37, and 97 all show significant additional H I emission in their GBT spectra that does not trace the emission from high column density features detected in the VLA data. In the cases of HCGs 30 and 37 this additional emission manifests as a spectrally broad and continuous emission feature, where no emission is detected the VLA data (Figure 22 & 28).

Based on the rms noise levels in the VLA cubes, this emission should be detectable in theory (at least in the spectral range where it is brightest). However, this is only true if the emission were spatially concentrated at the scale of the VLA synthesised beam, else the effective rms noise level would be higher, decreasing the significance of the emission feature. Hence the suggestion of Borthakur et al. (2010) that this may indicate a diffuse component. It is even possible that the emission is so spatially extended that it could be unrecoverable with the VLA. Both HCGs 30 and 37 were observed in DnC configuration, where the largest recoverable scale is expected to be $\sim 16''$. Given that this is larger than the maximum separation between the galaxies, it seems unlikely that this is the reason for the non-detection of this feature in the VLA data. However, if this were to be a limiting factor then the smaller minimum baselines of MeerKAT (20 m rather than 35 m) would be a means to resolve this issue. Furthermore, the increased sensitivity of MeerKAT, relative to the VLA, offers the current best possibility for detecting this ‘missing’ emission with an interferometer and resolving its nature.

5.4. Evolution of H I content of HCGs

As noted above there is little difference between the distribution of H I deficiencies for Phase 1 and Phase 2 groups (Figure 81). The apparent lack of a shift demonstrates that the processes that remove H I from the discs of galaxies and disperse it throughout the IGrM act on a timescale significantly shorter than the timescale on which H I is destroyed via evaporation or consumed through SF. As has been found by numerous works (e.g. Zwaan et al. 2005; Jones et al. 2016; Janowiecki et al. 2017; Said et al. 2019) the H I content of galaxies is a function of their larger scale environment, which may act as a partial explanation of the large scatter in H I deficiencies seen across Phase 1 & 2. This scatter is sufficiently large that even some Phase 3 groups are not distinct (in terms of their H I deficiencies) from Phase 1 & 2. HCG 61 has over 90% of its H I emission in extended features, but has a negligible H I deficiency. Even the prototypical example of a Phase 3 group, HCG 92, only has an H I deficiency of 0.46 dex, which is equalled by a handful of Phase 1 and 2 groups. Although, there

is a clear trend for most Phase 3 groups to be significantly more H I-deficient.

However, the increased H I deficiency of Phase 3 is not necessarily a one-way process. As indicated in Figure 80 by the pink arrow, it appears that Phase 3c groups were likely previously Phase 3a groups, devoid of H I, but have gained a new gas-bearing member. In some cases that new member is so gas-rich that these groups attain relatively low H I deficiencies again, and would be difficult to distinguish from Phase 1 groups if it were not for the fact that they are dominated by early-type galaxies and only one galaxy contains gas. However, we reiterate here that the morphological type of the galaxies is not used to define Phase 3c, which is based solely on the H I morphology of each group.

In some exceptional cases it appears these groups can undergo interactions with the newcomer galaxy, such that they effectively re-enter Phase 2 and appear to go around the cycle again. An example is HCG 79, which is classified as Phase 2 owing to 42% of its H I being in extended features. However, as can be seen in Figure 57, most of this H I emission clearly originated from HCG 79d, the only late-type in the group. We note that some of the extended features in this case are close to the noise level of the data, and that there is a notable difference between the GBT spectrum and that of the VLA (Figure 58), perhaps indicating there could be further extended features associated with HCG 79a. However, it regardless remains an evolved group that appears to have gained a new gas-rich member and now has a large fraction of its gas in extended features, analogous to a Phase 2 group.

This new step in the morphological sequence (Phase 3c) complicates the assumption that H I deficiency would increase with increasing morphological phase. This hypothesis implicitly assumes that groups cannot regain neutral gas after they have become significantly evolved. However, the larger number of groups dominated by early-type galaxies, but with a single gas-rich, late-type member casts serious doubt on this assumption. Though less likely, it is even possible that some groups containing a mixture of early and late-type galaxies (e.g. HCGs 10 & 25) represent the merger of two groups, one gas-rich and one evolved and gas-poor. In our scheme, such objects would likely be classified as either Phase 1 or Phase 2. Regardless of whether this more contrived scenario occurs frequently, the finding that the H I deficiency of an individual compact group does not necessarily monotonically increase with time means that, in general, it cannot be used as a proxy for evolutionary phase. Even with the Phase 3c groups excluded, H I deficiency is not a useful proxy as there appears to be more scatter than evolution in H I deficiency values across the remaining phases. Only the most H I-deficient Phase 3a groups would be distinguishable with such a proxy.

6. Conclusions

We have reduced and analysed archival VLA H I observations of 38 HCGs and determined their H I morphological phase based on an adaptation of the Verdes-Montenegro et al. (2001) evolutionary sequence. As this sequence is thought to represent the temporal evolution of HCGs it was expected that H I deficiency would act as a proxy for the evolutionary phase of a HCG, as gas is consumed or destroyed as the group evolves. However, we find that H I deficiency is a very poor proxy for the H I morphology of HCGs, with the exception that most Phase 3 groups are significantly deficient in H I.

The reason for this poor correspondence appears to be two-fold. Firstly, there is very little difference between the distribu-

tion of H I deficiency of Phase 1 and Phase 2 groups. This suggests that the initial H I content of groups is the primary factor determining their H I deficiencies in these two phases, and that the enormous morphological changes that occur between Phases 1 and 2 proceed on a timescale that is too short for a significant quantity of H I to be either consumed or destroyed. Secondly, the hypothesis that H I deficiency should be a proxy for H I morphology relies on the assumption that gas replenishment is largely negligible. However, we find a large fraction of the HCGs, about 25%, appear to be evolved groups dominated by early-type galaxies with a lone, late-type, gas-rich member, presumably a newcomer. In this way, once highly H I-deficient groups can have their gas content rejuvenated, confounding the use of H I deficiency as a proxy for evolutionary phase. We add a new sub-phase to the Verdes-Montenegro et al. (2001) evolutionary sequence to classify such groups.

We also find that there is not a clear one-to-one correspondence between the H I content of HCGs and the IR activity of their galaxies. However, most groups that are dominated by active galaxies are in Phase 2 of the H I evolutionary sequence, with ongoing interactions likely driving the ubiquitous IR activity. Phase 3 are likely to be dominated by passive galaxies, as is expected for these gas-poor groups. However, Phase 1 groups are a mixture of active, intermediate, and even quiescent IR classifications, as well as several groups with missing classifications.

Finally, we searched for evidence of a potential diffuse H I component in HCGs, as proposed by Borthakur et al. (2010). While some cases appear less compelling with our revised reduction of the VLA observations, the discrepancy between the spectra of HCGs 30 and 37 in VLA versus GBT observations remain difficult to explain without the presence of a diffuse component. Deeper interferometric observations with improved surface brightness sensitivity and *uv*-coverage might be capable of revealing this component and conclusively demonstrating its reality.

Acknowledgements. We thank the anonymous referee for their helpful comments that improved this paper. MGJ thanks the NRAO helpdesk for their rapid and insightful support, in particular with some of the oldest and most problematic VLA datasets. MGJ was supported by a Juan de la Cierva formación fellowship (FJCI-2016-29685) from the Spanish Ministerio de Ciencia, Innovación y Universidades (MCIU) during much this work. We also acknowledge support from the grants AYA2015-65973-C3-1-R (MINECO/FEDER, UE) and RTI2018-096228-B-C31 (MCIU), and from the grant IAA4SKA (Ref. R18-RT-3082) from the Economic Transformation, Industry, Knowledge and Universities Council of the Regional Government of Andalusia and the European Regional Development Fund from the European Union. This work has been supported by the State Agency for Research of the Spanish MCIU “Centro de Excelencia Severo Ochoa” programme under grant SEV-2017-0709. This work used the following Python libraries and packages: *numpy* (van der Walt et al. 2011), *scipy* (Virtanen et al. 2020), *matplotlib* (Hunter 2007), *astropy* (Astropy Collaboration et al. 2018), *aplpy* (Robitaille 2019), *astroquery* (Ginsburg et al. 2019), *jupyter* (Kluyver et al. 2016), *ruffus* (Goodstadt 2010), *CGAT-core* (Cribbs et al. 2019), and *Anaconda* (<https://anaconda.com>). The National Radio Astronomy Observatory is a facility of the National Science Foundation operated under cooperative agreement by Associated Universities, Inc. The Legacy Surveys consist of three individual and complementary projects: the Dark Energy Camera Legacy Survey (DECaLS; Proposal ID 2014B-0404; PIs: David Schlegel and Arjun Dey), the Beijing-Arizona Sky Survey (BASS; NOAO Prop. ID 2015A-0801; PIs: Zhou Xu and Xiaohui Fan), and the Mayall z-band Legacy Survey (MzLS; Prop. ID 2016A-0453; PI: Arjun Dey). This research has made use of the NASA/IPAC Extragalactic Database, which is funded by the National Aeronautics and Space Administration and operated by the California Institute of Technology. This research has made use of the VizieR catalogue access tool, CDS, Strasbourg, France. The original description of the VizieR service was published in Ochsenbein et al. (2000). This research has made use of the NASA/IPAC Infrared Science Archive, which is funded by the National Aeronautics and Space Administration and operated by the California Institute of Technology. Funding for the SDSS and SDSS-II has been provided by the Alfred P. Sloan Foundation, the Participating Institutions, the National Science Foundation, the U.S. Department of Energy, the National Aeronautics and Space

Administration, the Japanese Monbukagakusho, the Max Planck Society, and the Higher Education Funding Council for England. The SDSS Web Site is <http://www.sdss.org/>.

References

- Alatalo, K., Appleton, P. N., Lisenfeld, U., et al. 2015, *ApJ*, 812, 117
- Appleton, P. N., Xu, K. C., Reach, W., et al. 2006, *ApJ*, 639, L51
- Astropy Collaboration, Price-Whelan, A. M., Sipőcz, B. M., et al. 2018, *AJ*, 156, 123
- Bekki, K. & Couch, W. J. 2011, *MNRAS*, 415, 1783
- Belsole, E., Sauvageot, J.-L., Ponman, T. J., & Bourdin, H. 2003, *A&A*, 398, 1
- Borthakur, S., Yun, M. S., & Verdes-Montenegro, L. 2010, *ApJ*, 710, 385
- Borthakur, S., Yun, M. S., Verdes-Montenegro, L., et al. 2015, *ApJ*, 812, 78
- Brown, T., Catinella, B., Cortese, L., et al. 2017, *MNRAS*, 466, 1275
- Cluver, M. E., Appleton, P. N., Ogle, P., et al. 2013, *ApJ*, 765, 93
- Cribbs, A., Luna-Valero, S., George, C., et al. 2019, *F1000Research*, 8
- de Carvalho, R. R., Ribeiro, A. L. B., Capelato, H. V., & Zepf, S. E. 1997, *The Astrophysical Journal Supplement Series*, 110, 1
- de Mello, D. F., Urrutia-Viscarra, F., Mendes de Oliveira, C., et al. 2012, *MNRAS*, 426, 2441
- de Vaucouleurs, G., de Vaucouleurs, A., & Corwin, H. G., Jr. 1976, *Second reference catalogue of bright galaxies. Containing information on 4,364 galaxies with references to papers published between 1964 and 1975.*
- Desjardins, T. D., Gallagher, S. C., Tzanavaris, P., et al. 2013, *ApJ*, 763, 121
- Dey, A., Schlegel, D. J., Lang, D., et al. 2019, *AJ*, 157, 168
- Duarte Puertas, S., Iglesias-Páramo, J., Vilchez, J. M., et al. 2019, *A&A*, 629, A102
- Duc, P.-A., Cuillandre, J.-C., & Renaud, F. 2018, *MNRAS*, 475, L40
- Eigenthaler, P., Ploekinger, S., Verdugo, M., & Ziegler, B. 2015, *MNRAS*, 451, 2793
- Gallagher, S. C., Charlton, J. C., Hunsberger, S. D., Zaritsky, D., & Whitmore, B. C. 2001, *AJ*, 122, 163
- Ginsburg, A., Sipőcz, B. M., Brasseur, C. E., et al. 2019, *AJ*, 157, 98
- Goodstadt, L. 2010, *Bioinformatics*, 26, 2778
- Graziani, R., Courtois, H. M., Lavaux, G., et al. 2019, *MNRAS*, 488, 5438
- Guillard, P., Boulanger, F., Pineau des Forêts, G., et al. 2012, *ApJ*, 749, 158
- Haynes, M. P. & Giovanelli, R. 1984, *AJ*, 89, 758
- Hickson, P. 1982, *ApJ*, 255, 382
- Hickson, P., Kindl, E., & Auman, J. R. 1989, *ApJS*, 70, 687
- Hickson, P., Mendes de Oliveira, C., Huchra, J. P., & Palumbo, G. G. 1992, *ApJ*, 399, 353
- Huang, S., Haynes, M. P., Giovanelli, R., & Brinchmann, J. 2012, *ApJ*, 756, 113
- Huchtmeier, W. K. 1997, *A&A*, 325, 473
- Hunter, J. D. 2007, *Computing in Science & Engineering*, 9, 90
- Janowiecki, S., Catinella, B., Cortese, L., et al. 2017, *MNRAS*, 466, 4795
- Jones, M. G., Espada, D., Verdes-Montenegro, L., et al. 2018, *A&A*, 609, A17
- Jones, M. G., Papastergis, E., Haynes, M. P., & Giovanelli, R. 2016, *MNRAS*, 457, 4393
- Jones, M. G., Verdes-Montenegro, L., Damas-Segovia, A., et al. 2019, *A&A*, 632, A78
- Kluyver, T., Ragan-Kelley, B., Pérez, F., et al. 2016, in *ELPUB*
- Konstantopoulos, I. S., Appleton, P. N., Guillard, P., et al. 2014, *ApJ*, 784, 1
- Konstantopoulos, I. S., Maybhat, A., Charlton, J. C., et al. 2013, *ApJ*, 770, 114
- Kourkchi, E., Courtois, H. M., Graziani, R., et al. 2020, *AJ*, 159, 67
- Lisenfeld, U., Alatalo, K., Zucker, C., et al. 2017, *A&A*, 607, A110
- Lisenfeld, U., Braine, J., Duc, P. A., et al. 2002, *A&A*, 394, 823
- Makarov, D., Prugniel, P., Terekhova, N., Courtois, H., & Vauglin, I. 2014, *A&A*, 570, A13
- Martinez-Badenes, V., Lisenfeld, U., Espada, D., et al. 2012, *A&A*, 540, A96
- McMullin, J. P., Waters, B., Schiebel, D., Young, W., & Golap, K. 2007, in *Astronomical Society of the Pacific Conference Series*, Vol. 376, *Astronomical Data Analysis Software and Systems XVI*, ed. R. A. Shaw, F. Hill, & D. J. Bell, 127
- Mendes de Oliveira, C. L., Temporin, S., Cypriano, E. S., et al. 2006, *AJ*, 132, 570
- Molenaar, G. & Smirnov, O. 2018, *Astronomy and Computing*, 24, 45
- Nikiel-Wroczyński, B., Soida, M., Heald, G., & Urbanik, M. 2020, *ApJ*, 898, 110
- Ochsenbein, F., Bauer, P., & Marcut, J. 2000, *A&AS*, 143, 23
- O’Sullivan, E., Giacintucci, S., Vrtilik, J. M., Raychaudhury, S., & David, L. P. 2009, *ApJ*, 701, 1560
- O’Sullivan, E., Vrtilik, J. M., David, L. P., et al. 2014, *ApJ*, 793, 74
- Petrosian, A., McLean, B., Allen, R. J., & MacKenty, J. W. 2007, *ApJS*, 170, 33
- Plauchu-Frayn, I., Del Olmo, A., Coziol, R., & Torres-Papaqui, J. P. 2012, *A&A*, 546, A48
- Punzo, D., van der Hulst, T., Roerdink, J., & Fillion-Robin, J.-C. 2016, *SlicerAstro: Astronomy (HI) extension for 3D Slicer, Astrophysics Source Code Library*
- Reid, I. N., Brewer, C., Brucato, R. J., et al. 1991, *PASP*, 103, 661
- Rich, J. A., Dopita, M. A., Kewley, L. J., & Rupke, D. S. N. 2010, *ApJ*, 721, 505
- Robitaille, T. 2019, *APLpy v2.0: The Astronomical Plotting Library in Python*
- Román, J. & Trujillo, I. 2017, *MNRAS*, 468, 4039
- Said, K., Kraan-Korteweg, R. C., & Staveley-Smith, L. 2019, *MNRAS*, 486, 1796
- Serra, P., Koribalski, B., Duc, P.-A., et al. 2013, *MNRAS*, 428, 370
- Serra, P., Westmeier, T., Giese, N., et al. 2014, *SoFiA: Source Finding Application, Astrophysics Source Code Library*
- Serra, P., Westmeier, T., Giese, N., et al. 2015, *MNRAS*, 448, 1922
- Shi, D. D., Zheng, X. Z., Zhao, H. B., et al. 2017, *ApJ*, 846, 26
- Sulentic, J. W., Pietsch, W., & Arp, H. 1995, *A&A*, 298, 420
- Sulentic, J. W., Rosado, M., Dultzin-Hacyan, D., et al. 2001, *AJ*, 122, 2993
- Toribio, M. C., Solanes, J. M., Giovanelli, R., Haynes, M. P., & Martin, A. M. 2011, *ApJ*, 732, 93
- Tully, R. B., Courtois, H. M., & Sorce, J. G. 2016, *AJ*, 152, 50
- Tzanavaris, P., Hornschemeier, A. E., Gallagher, S. C., et al. 2010, *ApJ*, 716, 556
- van der Hulst, J. M. & Rots, A. H. 1981, *AJ*, 86, 1775
- van der Walt, S., Colbert, S. C., & Varoquaux, G. 2011, *Computing in Science Engineering*, 13, 22
- Verdes-Montenegro, L., Del Olmo, A., Iglesias-Páramo, J. I., et al. 2002, *A&A*, 396, 815
- Verdes-Montenegro, L., del Olmo, A., Perea, J., et al. 1997, *A&A*, 321, 409
- Verdes-Montenegro, L., Del Olmo, A., Yun, M. S., & Perea, J. 2005a, *A&A*, 430, 443
- Verdes-Montenegro, L., Sulentic, J., Lisenfeld, U., et al. 2005b, *A&A*, 436, 443
- Verdes-Montenegro, L., Yun, M. S., Williams, B. A., et al. 2001, *A&A*, 377, 812
- Virtanen, P., Gommers, R., Oliphant, T. E., et al. 2020, *Nature Methods*, 17, 261
- Vogt, F. P. A., Dopita, M. A., Borthakur, S., et al. 2015, *MNRAS*, 450, 2593
- Vogt, F. P. A., Dopita, M. A., & Kewley, L. J. 2013, *ApJ*, 768, 151
- Walker, L. M., Johnson, K. E., Gallagher, S. C., et al. 2016, *AJ*, 151, 30
- White, P. M., Bothun, G., Guerrero, M. A., West, M. J., & Barkhouse, W. A. 2003, *ApJ*, 585, 739
- Wilkinson, M. D., Dumontier, M., Aalbersberg, I. J., et al. 2016, *Scientific Data*, 3, 160018
- Williams, B. A., McMahon, P. M., & van Gorkom, J. H. 1991, *AJ*, 101, 1957
- Williams, B. A. & Rood, H. J. 1987, *ApJS*, 63, 265
- Williams, B. A. & van Gorkom, J. H. 1995, in *Astronomical Society of the Pacific Conference Series*, Vol. 70, *Groups of Galaxies*, ed. O.-G. Richter & K. Borne, 77
- Williams, B. A., Yun, M. S., & Verdes-Montenegro, L. 2002, *AJ*, 123, 2417
- York, D. G., Adelman, J., Anderson, John E., Jr., et al. 2000, *AJ*, 120, 1579
- Yun, M. S., Verdes-Montenegro, L., del Olmo, A., & Perea, J. 1997, *ApJ*, 475, L21
- Zucker, C., Walker, L. M., Johnson, K., et al. 2016, *ApJ*, 821, 113
- Zwaan, M. A., Meyer, M. J., Staveley-Smith, L., & Webster, R. L. 2005, *MNRAS*, 359, L30

Appendix A: Discrepancies with previously published VLA data

There are some other notable differences between the VLA data presented here and in Borthakur et al. (2010). In particular, the spectra of HCGs 15, 23, and 31 all differ significantly. HCG 15 has already been discussed in Section 4.1. HCG 23 is essentially undetected in the VLA data presented in Borthakur et al. (2010) and the bandwidth shown is too narrow to include most of the group’s emission. Whereas here we find strong detections of four group members and a close match with the GBT spectrum. It is unclear why this difference exists as the observations for this group were completed in 1990 and thus the same data were presumably used in both cases. In the case of HCG 31 the difference is primarily in the flux scale. Borthakur et al. (2010) found that this group was missing a significant amount of H I emission in its VLA spectrum, however, we find a very close match. We took no special steps in the reduction of this group and used the standard flux calibration models in CASA. There was likely an error in the calibration of these data in their original reduction, but at this point it is difficult to know where this occurred.

The final spectrum of HCG 58 is also quite different in the two works, with the Borthakur et al. (2010) spectrum matching somewhat better to the GBT spectrum. In this case it is likely that it is the exact form of the correction for the GBT beam response that is most responsible for the difference as much of the flux detected in the VLA cube is near or beyond the GBT beam, resulting in enormous correction factors.

Appendix B: Reproducibility

In addition to the analysis of the gas content of HCGs, we have followed best practices to support the reproducibility of the software methods used in this study. In this section we provide an overview of how we have tried to accomplish this, where barriers were met, and some lessons learnt.

Appendix B.1: Discussion of our approach

For our pilot study of HCG 16 (Jones et al. 2019) we constructed a full end-to-end pipeline (<https://github.com/AMIGA-IAA/hcg-16>), with software containers to preserve the exact software environment (in addition to the scripts themselves) in order to maximise the longevity of the pipeline. In this case, because of the larger scale of the current project, the increased volume of data, and the computation time it would take to reprocess all steps, we have instead aimed to create a flexible pipeline for processing the data of individual groups or VLA observing projects. This allowed the parameters of the data reduction to be tuned (e.g. for flagging, continuum subtraction, and imaging) for each data set and group, and the processing of each data set to be repeated and modified independently. This approach has clear advantages, but it also means that modifying the data reduction is a more manual process, as the pipeline must be executed separately for each VLA project or each HCG. In addition, the choice not to run the pipeline scripts in containers aides short term simplicity of execution, but may results in poorer long term preservation.

Our pipeline for processing the VLA H I data is available at https://github.com/AMIGA-IAA/hcg_hi_pipeline. The parameters and log file for our actual execution of the pipeline are stored in a separate github repository, https://github.com/AMIGA-IAA/hcg_global_hi_analysis. Instructions for the installation and use of the resources are described in the

repositories themselves. In addition, the second repository includes Python scripts and Jupyter notebooks to recreate all the plots and figures in this paper. These are based on our reduction of the data, and we have therefore also included all the final H I data cubes, moment zero maps, and cubelets⁷ of separated features in a Zenodo repository, <https://doi.org/10.5281/zenodo.6366659>. The analysis repository also contains links to the specific versions of CASA and SoFiA that were used to reduce and analyse the data.

Unfortunately, one step of the analysis process remains not fully reproducible, which is the separation of features using SlicerAstro. This separation is a necessarily manual and subjective process that is not straightforward to fully record in our pipeline. In the other steps of data reduction and analysis we have endeavoured to provide all the relevant parameters files such that another astronomer could modify and re-run these steps in a relatively approachable manner. However, for the separation of features step we have instead opted for preservation and exact reproduction, rather than full, independent reproducibility. We therefore note that even if another astronomer were to repeat (and modify) all the steps of our pipeline and then run our Jupyter notebooks, their modifications would only be carried forward for the properties of the groups that do not rely on the separated features cubelets. In general these are the global properties, such as the total H I mass and deficiency of each group, not those that depend on individual objects, such as the fraction of emission in extended features or the H I masses of individual galaxies.

All of the VLA data presented in this work are publicly available in the VLA archive. However, this archive cannot be automatically queried for data downloads, and thus the data for any group must be downloaded manually. The logs for the reduction of each data set include the names of all files that are imported so that the exact files can be obtained from the VLA archive, thus allowing anyone to repeat and modify our reduction (using our pipeline, or otherwise) from the beginning. In general, we anticipate end users only downloading and reprocessing data for the individual groups that they are interested in. Therefore, it does not make sense to re-host the entire data set (as we did for HCG 16, Jones et al. 2019) to allow automated access. In addition, creating additional, distributed copies of an archive is inefficient and impractical given the potential volume of data (for a generic VLA project). However, we point out that a more straightforward means to identify and locate individual VLA archive files, such as a digital object identifier, would streamline the process of (re-)acquiring the raw data.

For those who do not wish to repeat all the reduction, we advise downloading the reduced data products from the Zenodo repository. We have also included the relevant GBT H I spectra of HCGs from Borthakur et al. (2010), as the digital versions of these spectra have not been publicly released previously. Finally, we have included the optical images from DECaLS, SDSS, and POSS that we use. Although these can all be obtained from public services, because of the small volume of these data and because some services require manual interaction, we have chosen to re-host them. These data products can all be used with the analysis Jupyter notebooks to reproduce or modify any of the figures or values presented in the paper. In our prior work with HCG 16 we elected to enable cloud-execution of these notebooks using the Binder service (<https://mybinder.org/>). Although, the current analysis notebooks can also be executed

⁷ It should be noted that a bug in SlicerAstro produces a single bad pixel at the origin of each cubelet, which our scripts correct for.

using Binder, and we do recommend attempting this for those simply wishing to reproduce a few figures or a table, we also note that given the volume of data the Binder container may fail to build or launch and that the success or failure may depend on the end user's location as well as the current load on the infrastructure where Binder attempts to allocate resources.

When generating plots and tables, where possible we have generally tried to avoid using locally stored data that another user would have to locate, download, and extract manually. Instead we have relied heavily on *astroquery* (Ginsburg et al. 2019) to query data tables stored at the Centre de Données astronomiques de Strasbourg (CDS, <https://cds.u-strasbg.fr/>). In certain cases values were not available from CDS and we instead queried the NASA/IPAC Extragalactic Database (NED, <https://ned.ipac.caltech.edu/>). In the extremely unusual cases where values were not available from either service they were added manually from other sources, and these additions are preserved explicitly in the Jupyter notebooks.

Making use of querying services such as CDS and NED is very convenient and avoids the issue of each paper needing to replicate every data table on which they rely in order to be reproducible. However, it also raises a separate issue, which is that if any of the tables we query were to be amended or corrected then the final values we present could be altered. While this may be the desired functionality in some cases, it is also valid to want to preserve the exact form of the analysis. In practice, given the age of the data tables that we query, they are extremely unlikely to be updated. However, it would be an improvement to be able to specify whether to query from a specific version of a table (e.g. corresponding to a version on a particular date) or to simply query the latest version. As far as we are aware this option does not currently exist, but it would allow for an end user to select either functionality, depending on their aims.

To allow for either functionality, we have included the final data tables that our Jupyter notebooks produce (after querying CDS and NED) in the Zenodo repository. If the CDS/NED tables are amended, then these fixed versions of our tables can be used instead of regenerating them with the analysis notebooks. Thereby preserving the original form of the analysis.

Appendix B.2: Outlook

Our efforts to maximise the reproducibility of this work have taught us certain lessons regarding the storage and processing of astronomical data. We do not claim to be the first to discuss any of these issues (see e.g. Wilkinson et al. 2016), instead mostly these are lessons re-learned or reinforced, rather than being genuinely novel.

One of the least streamlined steps in our reproducibility framework is actually the first, the retrieval of the raw data from the VLA archive. This is mostly because this archive cannot be queried automatically. As we say above, this design choice is understandable due to the considerable data volume that VLA observations can represent. However, this issue is only likely to get worse in the future as new facilities, such as Square Kilometre Array (SKA) precursors (and soon the SKA itself) are already greatly increasing the volume of this type of data. The solution to this problem, which has been discussed many times before, is to stop moving the data (via the internet or on hard disks) to the home institution of each end user, but instead to have them process it in a central computing facility that also hosts the data archive. In our case this would prevent the disconnect arising from the raw data being stored in a completely different system from where they are processed. It would likely also make

sense for this same facility to act as an archive for the final data products that the end users produce when using the computing resources to reduce and analyse their data. This is essentially a (rudimentary) description of the proposed structure of SKA Regional Centres (e.g. <https://aussrc.org/wp-content/uploads/2021/05/SRC-White-Paper-v1.0-Final.pdf>).

This does not, however, address the issue of additional external data that is required for certain analyses. The need for such data typically arises when performing multi-frequency analyses, as observations at different wavelengths are often stored in different archives and can follow different standards. In our case, such data is mostly in the form of optical images from large sky surveys (POSS, SDSS, and DECaLS), as well as data tables that we query from CDS and NED. The need for such multi-frequency comparisons and analyses mean that the transfer of some data is inevitable. However, typically the external data will already be reduced and therefore be much smaller in volume than in its raw form, and thus represent less of an issue. If the data portals for data at all wavelengths have automatically accessible interfaces and follow common standards (such as those described by the International Virtual Observatory Alliance) then the inclusion of external data resources would be further streamlined.

Unlike in our previous work with HCG 16 (Jones et al. 2019), we have not constructed containers for the software. SoFia is publicly available, with its version history, through *github* and we therefore consider this to be a well-preserved resource that will likely be possible to build and install for several years. Similarly, although CASA is not available through *github*, the National Radio Astronomy Observatory (NRAO) provide back dated versions of CASA going back almost a decade. Aside from these software packages (and *SlicerAstro*, which we return to below) our analysis was performed exclusively in Python. We make use of *conda* as a means to preserve and build the coding environment such that the results can be reproduced exactly. While these solutions are all adequate and suitable for our use case, software and hardware will always continue to change over time, and at present the best means of preserving software environments is likely through containers and virtual machines (VMs). However, for each project to build their own containers and VMs for all their software is a formidable task. These are some community projects to assist with this, for example the Kern suite (Molenaar & Smirnov 2018) project in radio astronomy, however, ultimately once data reduction takes place predominantly in the cloud it will likely become the role of computing centres to maintain such software containers and backwards compatibility. This will make achieving reproducibility (at least of the software environment) more straightforward for the end users.

Finally, we return to the issue that the separation of features (in *SlicerAstro*) is not as fully reproducible as other steps in our pipeline because it requires manual (and subjective) input. This means that a new data product, created by modifying earlier data reduction steps, cannot automatically be propagated through the separation of features steps, and thus the results of any modifications can only be included automatically in some, but not all, of the final output of our analysis. Although in this particular scenario it is conceivable that in the future some algorithm maybe be developed to perform an equivalent separation of H₁ features automatically, in research in general there will always be manual and subjective steps which cannot be fully included in an automated pipeline. In such cases we suggest that the best way forward is to strive for preservation and exact duplication, rather than full independent, automated reproducibility. This means storing the data products before and after

such steps, along with any logs and important intermediate data products that may be manually produced during the process. Although this does not allow another researcher to interact with and modify the original reduction and analysis process, it does allow them to reliably compare to the results of each step in the process.

In summary, in our opinion the means to maximising the reproducibility of future radio astronomy projects (and in other domains) is for data, software, and computing resources to be provided in a central location which a user can access through a unified portal. As users would develop their own analysis scripts and tools in this environment, integrating version control tools and standard astronomy tools and services into the platform would help to maximise its usability. Crucially such a resource would remove much of the burden of “recreating the wheel” that currently falls on individual teams, thus making reproducibility a much more readily achievable goal for most projects.

Appendix C: Individual group members

Table C.1 shows the predicted and observed H I masses on individual galaxies in each HCG in our sample, as well as their IR classifications from Zucker et al. (2016).

Appendix D: Velocity maps

Maps of iso-velocity contours overlaid on the same optical images for each group in Section 3 are shown in Figure D.1. They can also be generated as described in Appendix B. The same source masks were used to produce these moment one contour maps, but only pixels with fluxes higher than $4.5\sigma_{\text{rms}} \sqrt{20\text{km s}^{-1}/\Delta v_{\text{chan}}}$ were included. The iso-velocity contours have separations of 20 km s^{-1} in all cases. HCGs 30, 37, and 62 are omitted as no H I was detected in their core groups.

Table C.1. H I deficiency of individual HCG members

HCG	Name	RA deg	Dec deg	Type	IR class	cz_{\odot} km s ⁻¹	$m_{B,c}$ mag	$\log M_{H I, pred}$ [M _⊙]	$\log M_{H I}$ [M _⊙]	H I-def dex
2	HCG2a	7.84955	8.46822	SBd	Active	4326	13.35 ± 0.1	9.59 ± 0.2	9.93	-0.34
2	HCG2b	7.82825	8.47518	cI	Active	4366	14.39 ± 0.1	9.2 ± 0.2	8.9	0.3
2	HCG2c	7.87232	8.40068	SBc	Active	4235	14.15 ± 0.1	9.29 ± 0.2	9.36	-0.07
7	HCG7a	9.8065	0.86363	Sb	Active	4210	12.98 ± 0.1	9.73 ± 0.2	9.05	0.68
7	HCG7b	9.82517	0.91273	SB0	Quiescent	4238	13.74 ± 0.2	9.44 ± 0.21		
7	HCG7c	9.89604	0.85962	SBc	Active	4366	12.6 ± 0.7	9.87 ± 0.33	9.53	0.34
7	HCG7d	9.82911	0.89148	SBc	Active	4116	14.77 ± 0.2	9.06 ± 0.21	8.9	0.16
10	HCG10a	21.58943	34.70204	SBb	Quiescent	5148	12.62 ± 0.1	9.86 ± 0.2	9.8	0.06
10	HCG10b	21.41817	34.71284	E1	Quiescent	4862	12.7 ± 0.1	9.83 ± 0.2		
10	HCG10c	21.57849	34.75395	Sc	Active	4660	14.07 ± 0.1	9.32 ± 0.2		
10	HCG10d	21.62865	34.67508	Scd	Active	4620	14.69 ± 0.2	9.09 ± 0.21	8.83	0.26
15	HCG15a	31.97094	2.16759	Sa	Quiescent	6967	14.29 ± 0.2	9.77 ± 0.21		
15	HCG15b	31.89217	2.11521	E0		7117	14.74 ± 0.1	9.6 ± 0.2		
15	HCG15c	31.91572	2.14973	E0	Quiescent	7222	14.37 ± 0.1	9.74 ± 0.2		
15	HCG15d	31.90634	2.18078	E2	Quiescent	6244	14.65 ± 0.2	9.63 ± 0.21		
15	HCG15e	31.85567	2.11613	Sa	Quiescent	7197	15.56 ± 0.1	9.29 ± 0.2		
15	HCG15f	31.90778	2.19028	Sbc	Active	6242	15.74 ± 0.2	9.22 ± 0.21	9.09	0.13
16	NGC848	32.5735	-10.32145	SBab		3992	13.37 ± 0.1	9.57 ± 0.2	9.64	-0.07
16	HCG16a	32.35312	-10.13622	SBab	Active	4152	12.76 ± 0.15	9.79 ± 0.21	8.97	0.82
16	HCG16b	32.3361	-10.13309	Sab	Quiescent	3977	13.27 ± 0.15	9.6 ± 0.21	8.66	0.94
16	HCG16c	32.41071	-10.14637	Im	Active	3851	13.1 ± 0.08	9.67 ± 0.2	9.46	0.21
16	HCG16d	32.42872	-10.18394	Im	Active	3847	13.42 ± 0.09	9.55 ± 0.2	9.64	-0.09
19	HCG19a	40.65998	-12.42128	E2	Quiescent	4279	14.0 ± 0.2	9.39 ± 0.21		
19	HCG19b	40.67548	-12.42777	Scd	Active	4210	15.24 ± 0.2	8.93 ± 0.21	9.17	-0.24
19	HCG19c	40.69507	-12.39783	Sdm	Canyon	4253	14.46 ± 0.1	9.22 ± 0.2	8.62	0.6
22	NGC1188	45.93135	-15.48522	S0		2628	14.32 ± 0.39	8.98 ± 0.25		
22	HCG22a	45.91056	-15.61369	E2	Quiescent	2705	12.24 ± 0.13	9.76 ± 0.21		
22	HCG22b	45.8593	-15.66187	Sa		2625	14.47 ± 0.1	8.92 ± 0.2		
22	HCG22c	45.85141	-15.62332	SBcd	Canyon	2544	13.9 ± 0.7	9.14 ± 0.33	9.41	-0.27
23	HCG23-26	46.78954	-9.48784	cI		5283	19.26 ± 0.5	7.58 ± 0.27	9.22	-1.64
23	HCG23a	46.73285	-9.54406	Sab	Quiescent	4798	14.32 ± 0.2	9.44 ± 0.21	9.28	0.16
23	HCG23b	46.78976	-9.59332	SBc	Active	4921	14.42 ± 0.2	9.4 ± 0.21	9.74	-0.34
23	HCG23c	46.82692	-9.61328	S0	Quiescent	5016	15.52 ± 0.2	8.99 ± 0.21		
23	HCG23d	46.73012	-9.62953	Sd	Active	4562	16.0 ± 0.5	8.81 ± 0.27	9.31	-0.5
25	HCG25a	50.17978	-1.10935	SBc	Active	6285	13.86 ± 0.1	9.8 ± 0.2	9.95	-0.15
25	HCG25b	50.18997	-1.04486	SBa	Quiescent	6408	14.45 ± 0.2	9.58 ± 0.21	9.55	0.03
25	HCG25d	50.16172	-1.0354	S0		6401	15.92 ± 0.1	9.03 ± 0.2		
25	HCG25f	50.18977	-1.05425	S0		6279	16.98 ± 0.2	8.63 ± 0.21		
26	HCG26a	50.4804	-13.65085	Scd	Active	9678	16.1 ± 0.7	9.34 ± 0.33	10.17	-0.83
26	HCG26b	50.48811	-13.64841	E0		9332	15.61 ± 0.2	9.52 ± 0.21		
26	HCG26c	50.45648	-13.64554	S0		9618	17.1 ± 0.1	8.96 ± 0.2		
26	HCG26d	50.48558	-13.64543	cI		9133	15.81 ± 0.2	9.44 ± 0.21		
26	HCG26e	50.46302	-13.66473	Im	Active	9623	17.05 ± 0.1	8.98 ± 0.2	8.88	0.1
26	HCG26f	50.48992	-13.66392	cI		9626	18.68 ± 0.1	8.37 ± 0.2		
26	HCG26g	50.48012	-13.64874	S0		9293	17.4 ± 0.7	8.85 ± 0.33		
30	HCG30a	69.07744	-2.83129	SB-	Quiescent	4697	12.87 ± 0.2	9.93 ± 0.21		
30	HCG30b	69.12619	-2.86656	Sa	Quiescent	4625	13.65 ± 0.1	9.64 ± 0.2		
30	HCG30c	69.097	-2.79985	SBbc	Active	4508	15.06 ± 0.1	9.11 ± 0.2		
30	HCG30d	69.15276	-2.84302	S0		4666	15.69 ± 0.1	8.87 ± 0.2		
31	HCG31g	75.43338	-4.28875	cI		4011	15.11 ± 0.5	8.98 ± 0.27	9.0	-0.02
31	HCG31q	75.40974	-4.22245	cI		4090	16.01 ± 0.5	8.64 ± 0.27	8.71	-0.07
31	HCG31a	75.41146	-4.25946	Sdm		4042	14.83 ± 0.2	9.08 ± 0.21	9.22	-0.14
31	HCG31b	75.39756	-4.26401	Sm		4171	14.31 ± 0.2	9.28 ± 0.21	9.13	0.15
31	HCG31c	75.40751	-4.2577	Im	Active	4068	12.5 ± 0.5	9.96 ± 0.27	8.96	1.0

Notes. Columns: (1) HCG ID number, (2) name of group member, (3) right ascension, (4) declination, (5) optical morphological Hubble type (Hickson et al. 1989), (6) infrared classification (Zucker et al. 2016), (7) redshift (Hickson et al. 1992), (8) corrected apparent B-band magnitude (Hickson et al. 1989), (9) predicted H I mass based on B-band luminosity (Jones et al. 2018), (10) measured H I mass from VLA observations, (11) H I deficiency.

Table C.1 continued.

HCG	Name	RA deg	Dec deg	Type	IR class	$c z_{\odot}$ km s^{-1}	$m_{\text{B,c}}$ mag	$\log M_{\text{HI,pred}}$ [M_{\odot}]	$\log M_{\text{HI}}$ [M_{\odot}]	H I-def dex
33	HCG33a	77.69998	18.01867	E1	Quiescent	7570	15.35 ± 0.2	9.46 ± 0.21		
33	HCG33b	77.69854	18.02957	E4	Quiescent	8006	15.41 ± 0.2	9.44 ± 0.21		
33	HCG33c	77.68831	18.01956	Sd	Active	7823	16.4 ± 0.7	9.06 ± 0.33	10.02	-0.96
33	HCG33d	77.72327	18.03292	E0		7767	16.73 ± 0.2	8.94 ± 0.21		
37	HCG37a	138.41438	29.99243	E7	Quiescent	6745	12.97 ± 0.2	10.27 ± 0.21		
37	HCG37b	138.38589	29.99977	Sbc	Canyon	6741	14.5 ± 0.2	9.7 ± 0.21		
37	HCG37c	138.40514	29.99954	S0a		7357	15.57 ± 0.2	9.3 ± 0.21		
37	HCG37d	138.39107	30.01442	SBdm	Active	6207	15.87 ± 0.2	9.18 ± 0.21		
37	HCG37e	138.3918	30.03975	E0	Active	6363	16.21 ± 0.1	9.06 ± 0.2		
38	HCG38a	141.89442	12.26922	Sbc	Active	8652	15.25 ± 0.1	9.61 ± 0.2		
38	HCG38b	141.93169	12.28719	SBd	Active	8635	14.76 ± 0.2	9.79 ± 0.21		
38	HCG38c	141.93544	12.2879	Im	Active	8692	15.39 ± 0.2	9.56 ± 0.21		
40	HCG40a	144.72309	-4.84903	E3	Quiescent	6628	13.44 ± 0.2	10.11 ± 0.21		
40	HCG40b	144.72942	-4.86608	S0	Quiescent	6842	14.58 ± 0.2	9.68 ± 0.21		
40	HCG40c	144.72173	-4.85936	Sbc	Active	6890	15.15 ± 0.2	9.47 ± 0.21	9.29	0.18
40	HCG40d	144.73246	-4.83737	SBa	Active	6492	14.53 ± 0.2	9.7 ± 0.21	9.09	0.61
40	HCG40e	144.73111	-4.85775	Sc	Active	6625	16.69 ± 0.2	8.89 ± 0.21		
47	HCG47a	156.4431	13.71686	SBb	Active	9581	14.61 ± 0.2	9.93 ± 0.21		
47	HCG47b	156.4527	13.72793	E3		9487	15.67 ± 0.2	9.53 ± 0.21		
47	HCG47c	156.45454	13.75306	Sc	Active	9529	16.63 ± 0.2	9.17 ± 0.21		
47	HCG47d	156.4495	13.74866	Sd	Active	9471	16.2 ± 0.7	9.33 ± 0.33		
48	HCG48a	159.44682	-27.08051	E2	Quiescent	2267	13.21 ± 0.2	9.33 ± 0.21		
48	HCG48b	159.45641	-27.12175	Sc	Active	2437	14.63 ± 0.2	8.79 ± 0.21	8.77	0.02
49	HCG49SDSS1	164.16092	67.15169	cI		9950	18.56 ± 0.02	8.47 ± 0.2	9.02	-0.55
49	HCG49a	164.17315	67.18515	Scd	Active	9939	15.87 ± 0.2	9.48 ± 0.21		
49	HCG49b	164.16325	67.18027	Sd	Active	9930	16.3 ± 0.2	9.31 ± 0.21		
49	HCG49c	164.15288	67.18123	Im	Active	9926	17.18 ± 0.2	8.98 ± 0.21		
49	HCG49d	164.13946	67.17808	E5	Active	10010	16.99 ± 0.2	9.06 ± 0.21		
54	A11272054	172.36851	20.63192	cI		1397	19.01 ± 0.05	6.96 ± 0.2	7.7	-0.74
54	HCG54a	172.31332	20.58358	Sdm	Active	1397	13.86 ± 0.2	8.89 ± 0.21		
54	HCG54b	172.30866	20.5815	Im	Active	1412	16.08 ± 0.2	8.06 ± 0.21		
54	HCG54c	172.31785	20.58646	Im	Active	1420	16.8 ± 0.7	7.79 ± 0.33		
54	HCG54d	172.31885	20.5886	Im		1670	18.02 ± 0.2	7.33 ± 0.21		
56	HCG56a	173.19443	52.94092	Sc	Active	8245	15.24 ± 0.2	9.57 ± 0.21	9.89	-0.32
56	HCG56b	173.16862	52.95052	SB0	Active	7919	14.5 ± 0.2	9.84 ± 0.21		
56	HCG56c	173.15296	52.94758	S0	Quiescent	8110	15.37 ± 0.2	9.52 ± 0.21		
56	HCG56d	173.14712	52.94725	S0	Active	8346	16.52 ± 0.2	9.08 ± 0.21		
56	HCG56e	173.13647	52.93923	S0	Active	7924	16.23 ± 0.1	9.19 ± 0.2		
57	HCG57a	174.47409	21.98084	Sb	Canyon	8727	13.99 ± 0.2	10.16 ± 0.21		
57	HCG57b	174.43198	22.00933	SBb	Quiescent	9022	14.32 ± 0.2	10.04 ± 0.21		
57	HCG57c	174.46564	21.97384	E3		9081	14.63 ± 0.2	9.92 ± 0.21		
57	HCG57d	174.47966	21.98564	SBc	Active	8977	14.51 ± 0.2	9.96 ± 0.21		
57	HCG57e	174.45486	22.02576	S0a	Quiescent	8992	15.37 ± 0.1	9.64 ± 0.2		
57	HCG57f	174.47535	21.93609	E4	Quiescent	9594	15.22 ± 0.1	9.7 ± 0.2		
57	HCG57g	174.43585	22.02083	SB0		9416	15.84 ± 0.1	9.46 ± 0.2		
57	HCG57h	174.46122	22.01187	SBb	Active	9042	16.75 ± 0.1	9.12 ± 0.2		
58	HCG58a	175.54619	10.2777	Sb	Active	6138	13.56 ± 0.2	9.94 ± 0.21	9.67	0.27
58	HCG58b	175.59827	10.2642	SBab	Quiescent	6503	13.4 ± 0.2	10.0 ± 0.21		
58	HCG58c	175.47156	10.30409	SB0a	Quiescent	6103	13.83 ± 0.2	9.84 ± 0.21		
58	HCG58d	175.52466	10.35087	E1	Quiescent	6270	14.49 ± 0.2	9.59 ± 0.21		
58	HCG58e	175.52022	10.38388	Sbc	Active	6052	14.86 ± 0.2	9.45 ± 0.21	9.13	0.32
59	HCG59a	177.11466	12.72734	Sa	Active	4109	14.52 ± 0.1	9.3 ± 0.2		
59	HCG59b	177.08402	12.71615	E0	Canyon	3908	15.2 ± 0.2	9.04 ± 0.21	9.35	-0.31
59	HCG59c	177.13534	12.70525	Sc		4347	14.4 ± 0.5	9.34 ± 0.27	8.63	0.71
59	HCG59d	177.12802	12.72981	Im	Active	3866	15.8 ± 0.2	8.82 ± 0.21	9.16	-0.34
61	HCG61a	183.07729	29.1798	S0a	Quiescent	3784	12.82 ± 0.1	9.94 ± 0.2		
61	HCG61c	183.12894	29.16854	Sbc	Active	3956	13.53 ± 0.1	9.67 ± 0.2	9.13	0.54
61	HCG61d	183.11153	29.14912	S0	Quiescent	3980	14.12 ± 0.1	9.45 ± 0.2		

Table C.1 continued.

HCG	Name	RA deg	Dec deg	Type	IR class	c_{Z_0} km s^{-1}	$m_{\text{B,c}}$ mag	$\log M_{\text{HI,pred}}$ [M_{\odot}]	$\log M_{\text{HI}}$ [M_{\odot}]	H I-def dex
62	HCG62a	193.27438	-9.20458	E3	Quiescent	4355	13.36 ± 0.2	9.73 ± 0.21		
62	HCG62b	193.26862	-9.19889	S0	Quiescent	3651	13.76 ± 0.2	9.58 ± 0.21		
62	HCG62c	193.29147	-9.19809	S0	Quiescent	4359	14.57 ± 0.2	9.28 ± 0.21		
62	HCG62d	193.27827	-9.25811	E2	Canyon	4123	15.81 ± 0.1	8.81 ± 0.2		
68	HCG68a	208.36072	40.28294	S0	Quiescent	2162	11.84 ± 0.08	9.87 ± 0.2		
68	HCG68b	208.3611	40.30247	E2	Quiescent	2635	12.24 ± 0.06	9.72 ± 0.2		
68	HCG68c	208.34055	40.36331	SBbc	Active	2313	11.93 ± 0.2	9.83 ± 0.21	9.95	-0.12
68	HCG68d	208.44021	40.33812	E3	Quiescent	2408	13.73 ± 0.1	9.16 ± 0.2		
68	HCG68e	208.49892	40.27334	S0	Quiescent	2401	14.22 ± 0.1	8.97 ± 0.2		
71	AGC732898	212.76914	25.55967	Sd		9083	17.97 ± 0.5	8.64 ± 0.27	9.22	-0.58
71	AGC242021	212.72563	25.55402	cI		9199	17.1 ± 0.36	8.97 ± 0.24	9.72	-0.75
71	HCG71a	212.73775	25.4967	SBc	Canyon	9320	13.75 ± 0.2	10.23 ± 0.21	10.39	-0.16
71	HCG71b	212.76055	25.51965	Sb	Active	9335	14.9 ± 0.1	9.79 ± 0.2		
71	HCG71c	212.77152	25.48257	SBc	Active	8827	15.56 ± 0.1	9.54 ± 0.2	9.85	-0.31
79	HCG79a	239.79777	20.75416	E0	Active	4292	14.35 ± 0.2	9.35 ± 0.21		
79	HCG79b	239.80276	20.76312	S0	Active	4446	13.78 ± 0.2	9.56 ± 0.21		
79	HCG79c	239.79586	20.76154	S0	Quiescent	4146	14.72 ± 0.2	9.21 ± 0.21		
79	HCG79d	239.80026	20.74648	Sdm	Active	4503	15.87 ± 0.2	8.78 ± 0.21	9.26	-0.48
88	HCG88a	313.14714	-5.71068	Sb	Canyon	6033	13.18 ± 0.1	9.97 ± 0.2	8.82	1.15
88	HCG88b	313.12394	-5.74655	SBb	Quiescent	6010	13.24 ± 0.1	9.95 ± 0.2	9.33	0.62
88	HCG88c	313.10833	-5.77224	Sc	Active	6083	13.87 ± 0.1	9.71 ± 0.2	9.79	-0.08
88	HCG88d	313.05323	-5.79796	Sc	Active	6032	14.49 ± 0.2	9.48 ± 0.21	9.46	0.02
90	HCG90a	330.50889	-31.87014	Sa	Active	2575	12.36 ± 0.07	9.62 ± 0.2	8.94	0.68
90	HCG90b	330.53631	-31.99068	E0	Quiescent	2525	12.57 ± 0.13	9.54 ± 0.21		
90	HCG90c	330.51423	-31.97451	E0	Quiescent	2696	12.73 ± 0.06	9.48 ± 0.2		
90	HCG90d	330.52602	-31.99423	Im	Active	2778	12.81 ± 0.15	9.45 ± 0.21		
91	HCG91a	332.28174	-27.80984	SBc	Active	7151	12.62 ± 0.13	10.36 ± 0.21	9.83	0.53
91	HCG91b	332.3183	-27.73134	Sc	Active	7196	14.63 ± 0.2	9.61 ± 0.21	9.67	-0.06
91	HCG91c	332.30881	-27.78241	Sc	Active	7319	14.47 ± 0.2	9.67 ± 0.21	9.66	0.01
91	HCG91d	332.28567	-27.80086	SB0	Quiescent	7195	14.99 ± 0.2	9.47 ± 0.21		
92	HCG92b	338.994	33.96595	Sbc	Quiescent	5774	13.18 ± 0.13	10.11 ± 0.21		
92	HCG92c	339.01604	33.97535	SBc	Active	6764	13.33 ± 0.1	10.05 ± 0.2		
92	HCG92d	338.9871	33.96555	Sc	Quiescent	6630	13.63 ± 0.08	9.94 ± 0.2		
92	HCG92e	338.96756	33.94459	E1	Quiescent	6599	14.01 ± 0.08	9.79 ± 0.2		
93	HCG93a	348.81679	18.96147	E1	Quiescent	5140	12.61 ± 0.1	10.07 ± 0.2		
93	HCG93b	348.82171	19.04158	SBd	Active	4672	13.18 ± 0.1	9.85 ± 0.2	9.53	0.32
93	HCG93c	348.76515	18.97311	SBa	Quiescent	5132	13.94 ± 0.1	9.57 ± 0.2		
93	HCG93d	348.88811	19.0479	SB0		5173	15.27 ± 0.1	9.07 ± 0.2		
95	HCG95a	349.87475	9.50793	E3	Quiescent	11888	14.42 ± 0.2	10.1 ± 0.21		
95	HCG95b	349.8909	9.49491	Scd	Active	11637	15.34 ± 0.1	9.75 ± 0.2		
95	HCG95c	349.86626	9.49434	Sm	Active	11562	15.2 ± 0.2	9.81 ± 0.21		
95	HCG95d	349.87951	9.50274	Sc	Active	11593	16.14 ± 0.1	9.45 ± 0.2		
96	HCG96a	351.98711	8.77821	Sc	Active	8698	13.53 ± 0.2	10.21 ± 0.21	9.93	0.28
96	HCG96b	352.02523	8.76841	E2	Quiescent	8616	14.49 ± 0.1	9.85 ± 0.2		
96	HCG96c	351.99507	8.7828	Sa	Active	8753	15.69 ± 0.2	9.4 ± 0.21		
96	HCG96d	352.00084	8.76733	Im	Active	8975	16.56 ± 0.1	9.07 ± 0.2		
97	HCG97a	356.84591	-2.30096	E5	Quiescent	6910	14.16 ± 0.2	9.72 ± 0.21		
97	HCG97b	356.90753	-2.31716	Sc	Canyon	6940	14.83 ± 0.1	9.47 ± 0.2	8.68	0.79
97	HCG97c	356.84884	-2.35143	Sa	Quiescent	5995	14.54 ± 0.1	9.58 ± 0.2		
97	HCG97d	356.82867	-2.31329	E1		6239	14.45 ± 0.1	9.61 ± 0.2		
97	HCG97e	356.83253	-2.28102	S0a	Canyon	6579	16.31 ± 0.2	8.91 ± 0.21		
100	MRK935	0.43845	13.10067	cI		5606	15.34 ± 0.05	9.08 ± 0.2	8.54	0.54
100	HCG100a	0.33374	13.11095	Sb		5300	13.66 ± 0.1	9.71 ± 0.2		
100	HCG100b	0.35885	13.11278	Sm		5253	14.9 ± 0.1	9.25 ± 0.2		
100	HCG100c	0.30629	13.14398	SBc		5461	15.22 ± 0.1	9.13 ± 0.2		
100	HCG100d	0.31151	13.11264	Scd		5590	15.97 ± 0.1	8.84 ± 0.2		

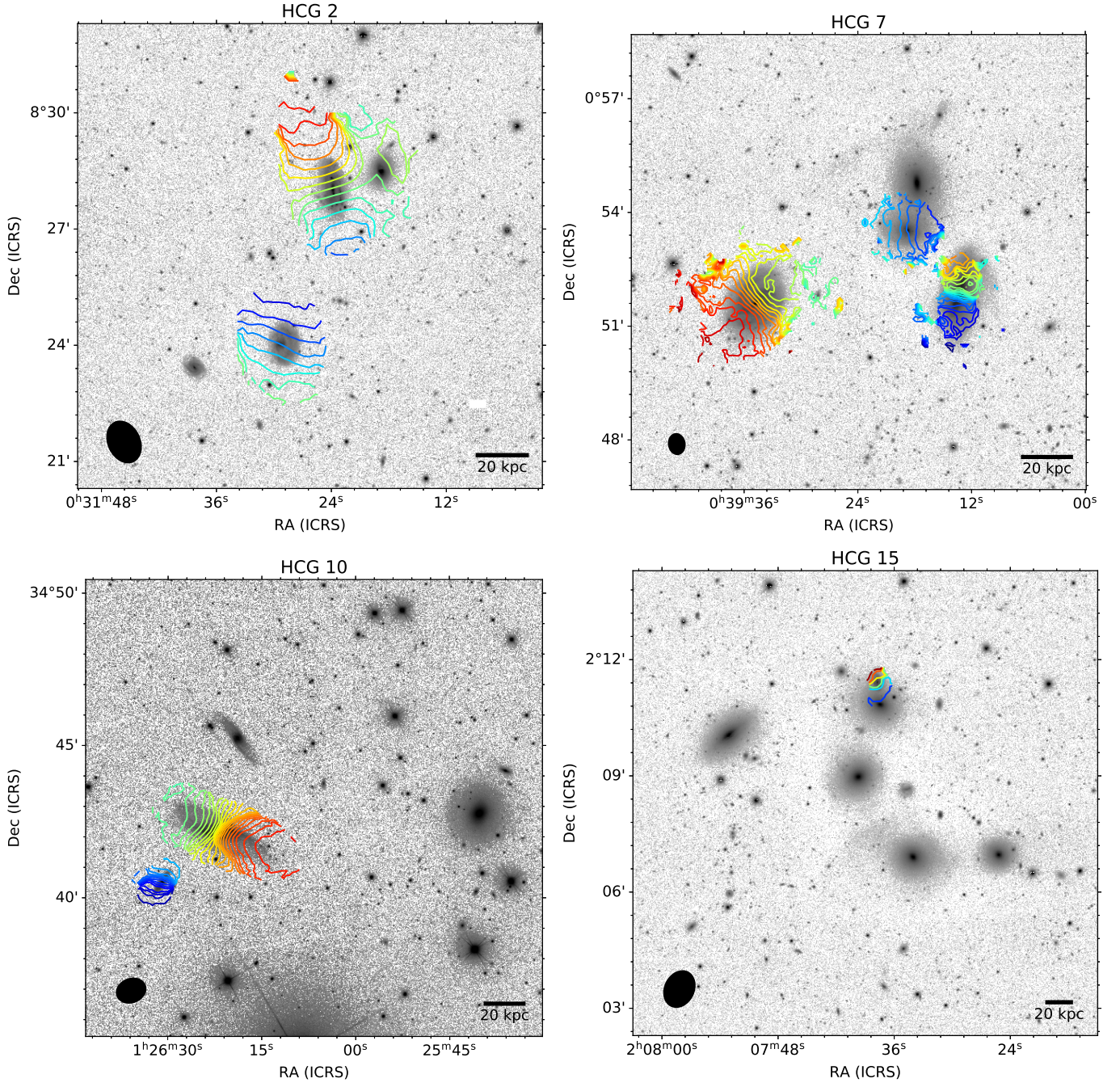


Fig. D.1. Iso-velocity contours (separated by 20 km s^{-1}) overlaid on DECaLS, SDSS, or POSS images depending on the group. Contours follow a rainbow colour scheme with high velocities corresponding to redder colours and lower velocities to bluer colours (note that the velocity range varies in each panel, but contours are always separated by 20 km s^{-1}).

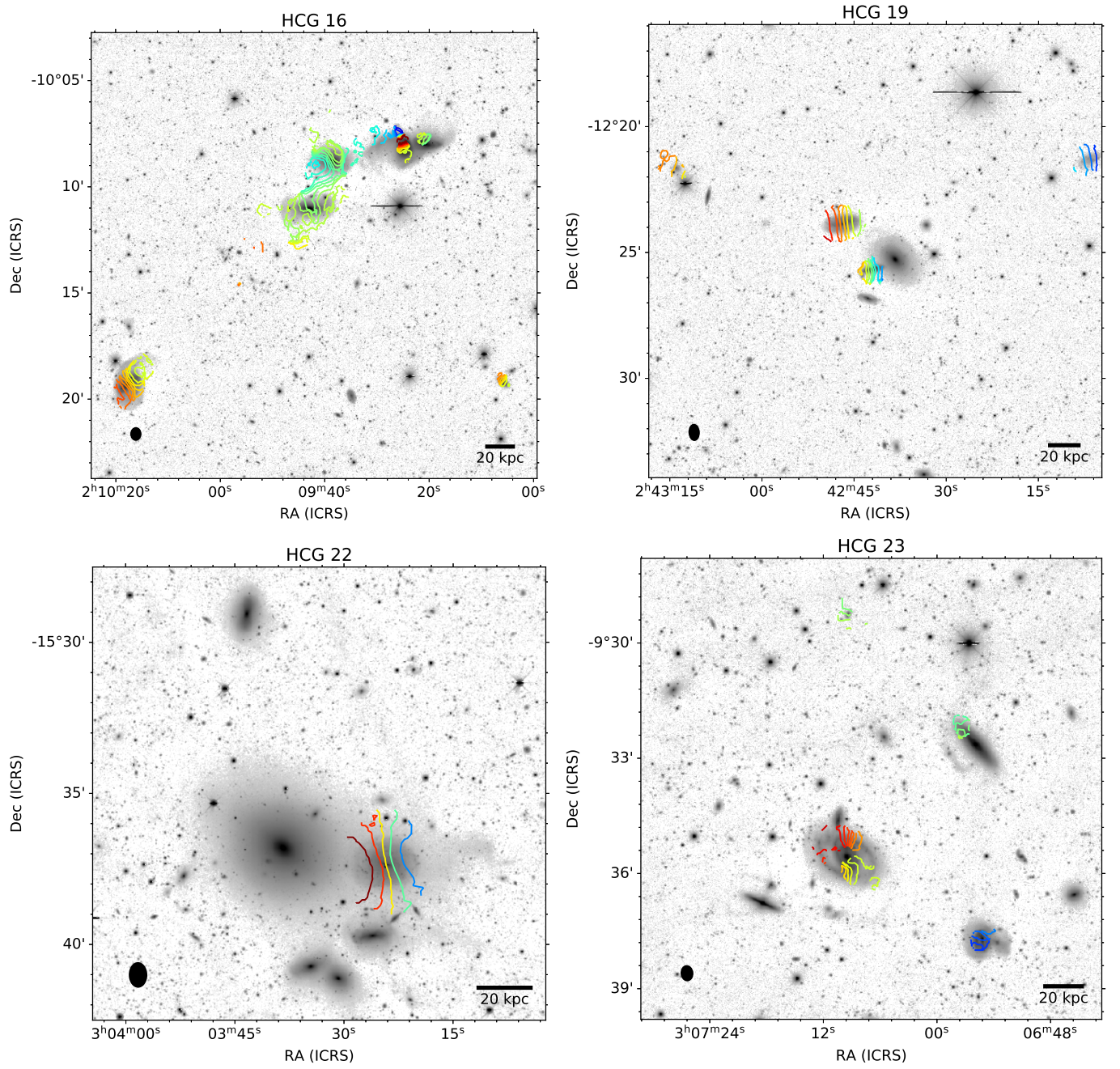


Figure D.1 continued.

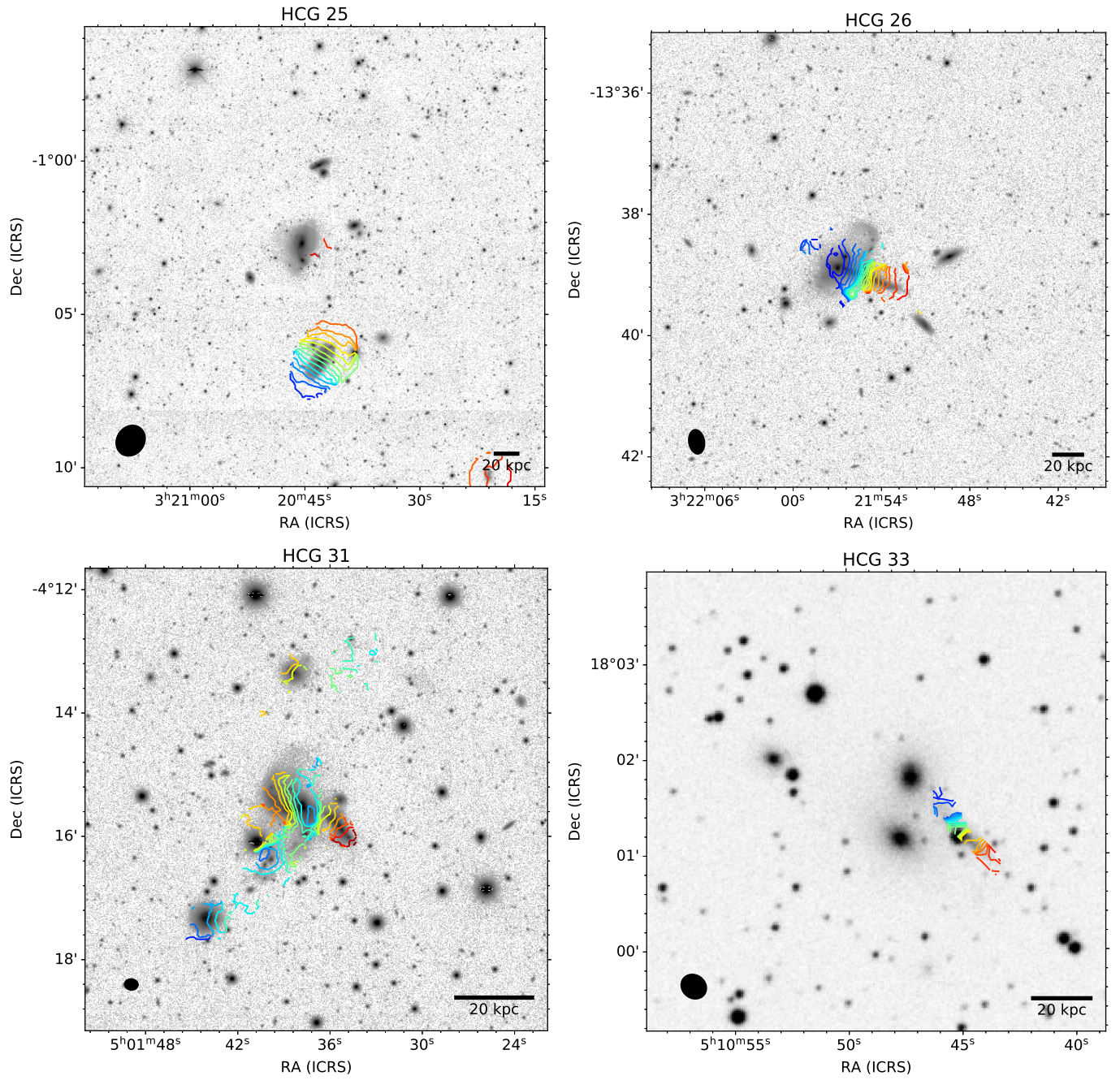


Figure D.1 continued.

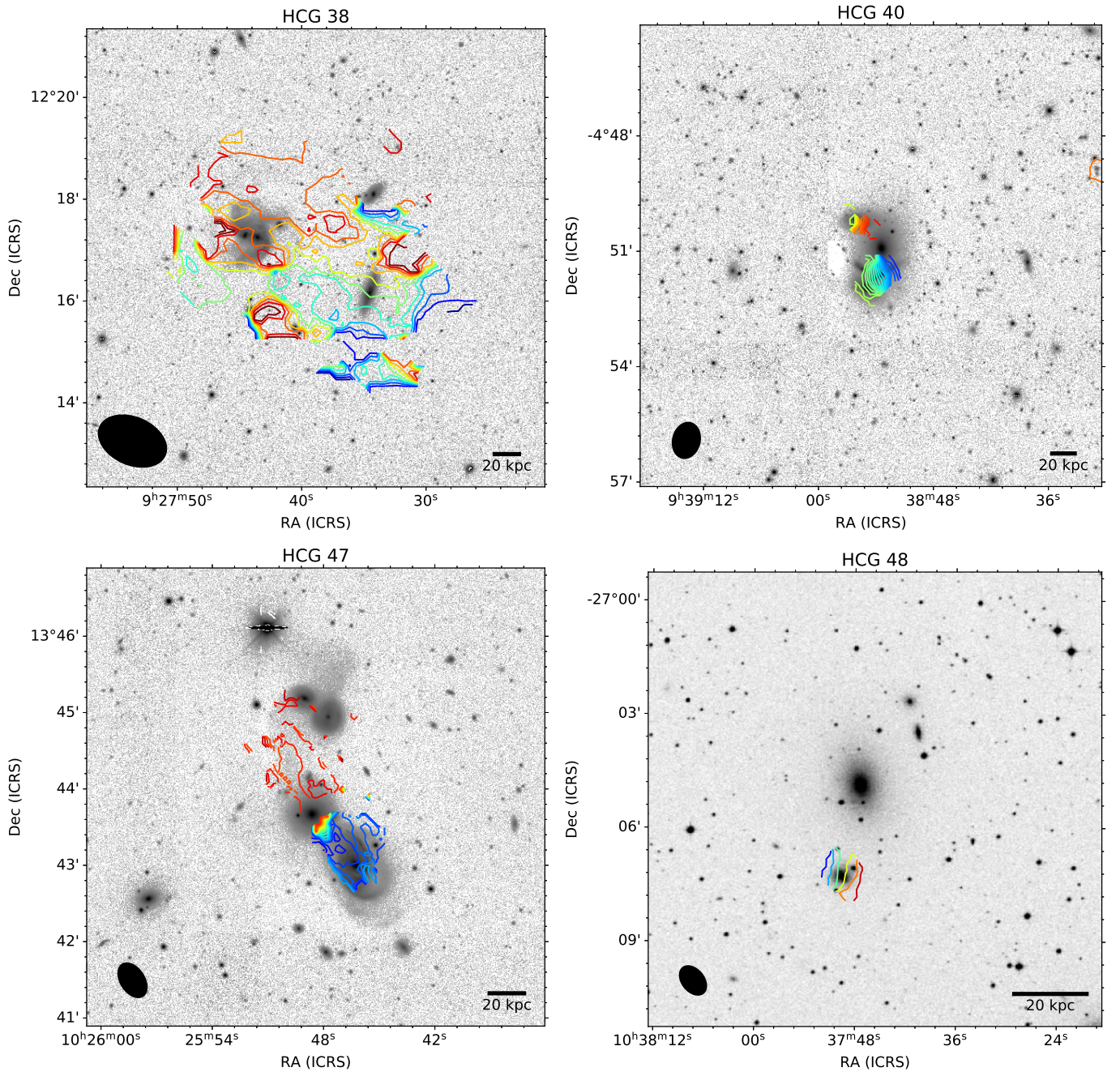


Figure D.1 continued.

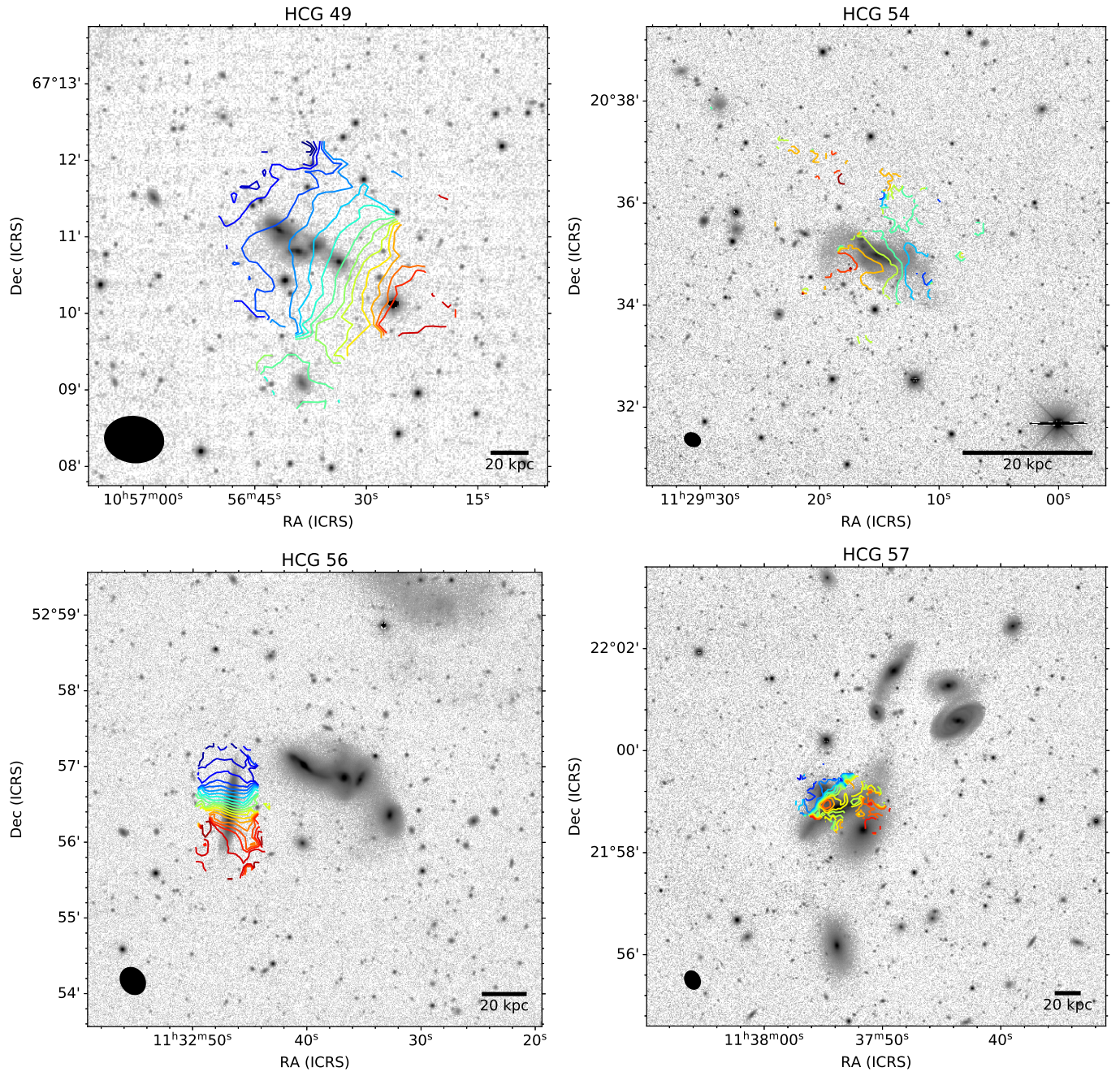


Figure D.1 continued.

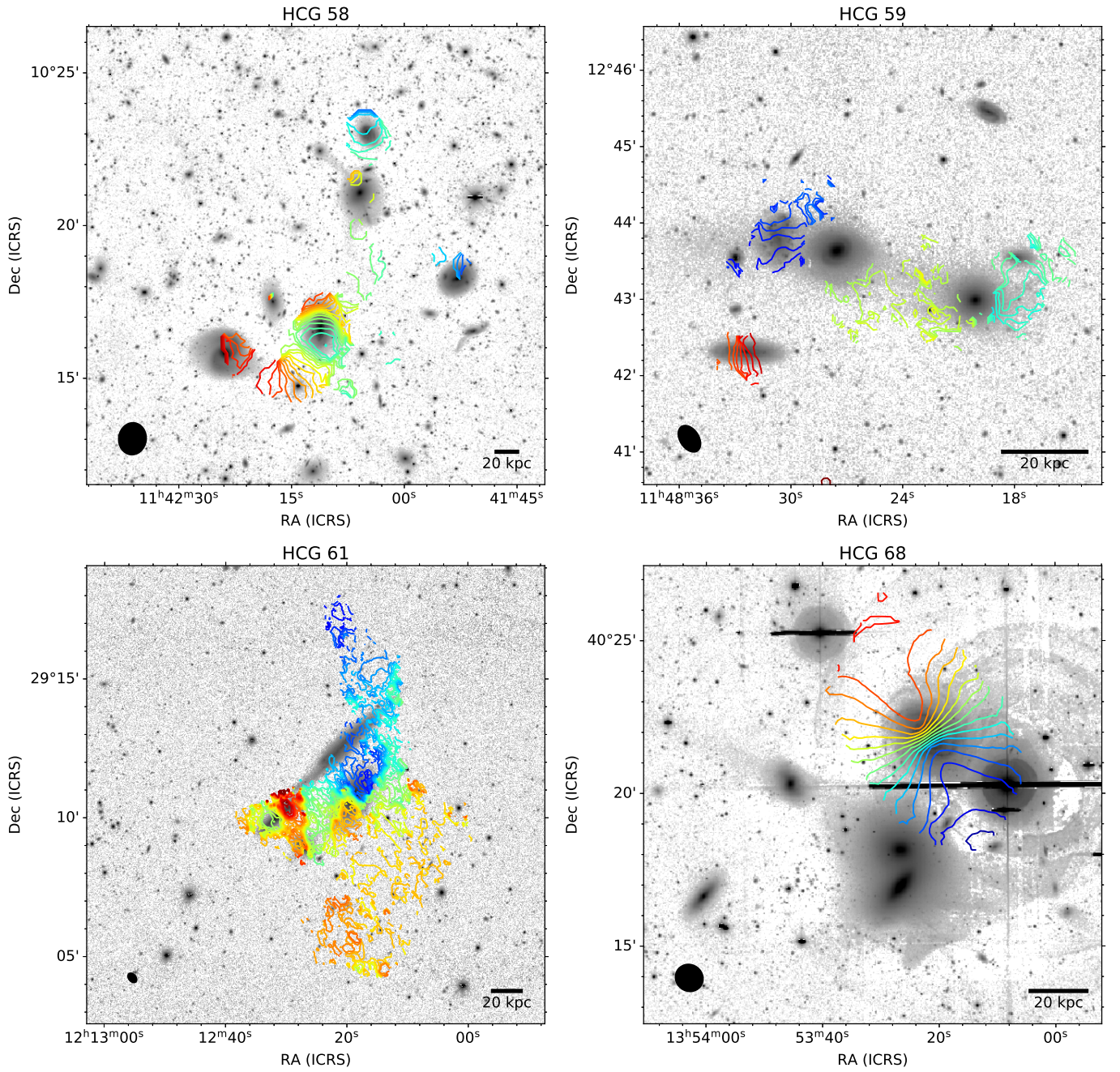


Figure D.1 continued.

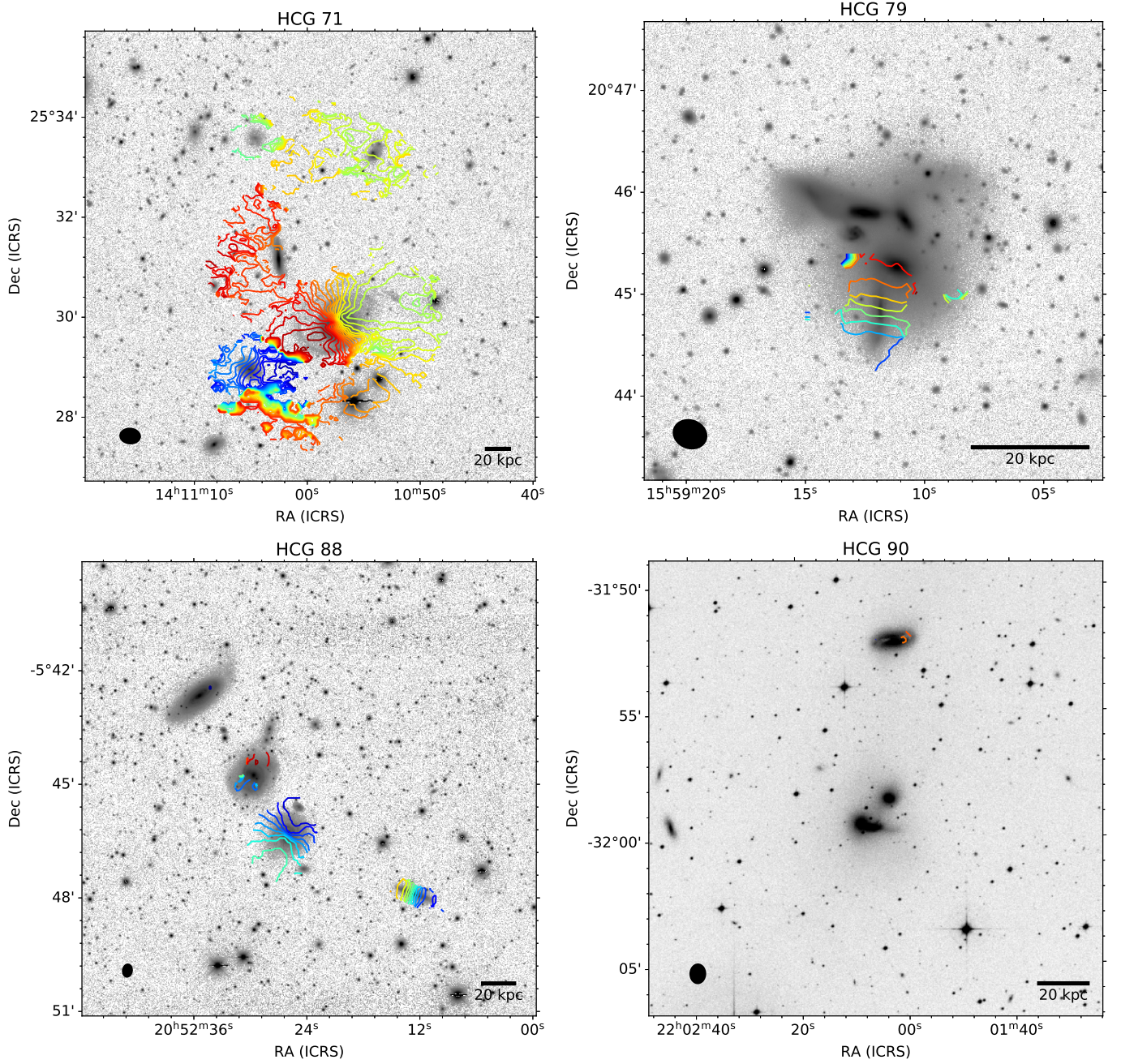


Figure D.1 continued.

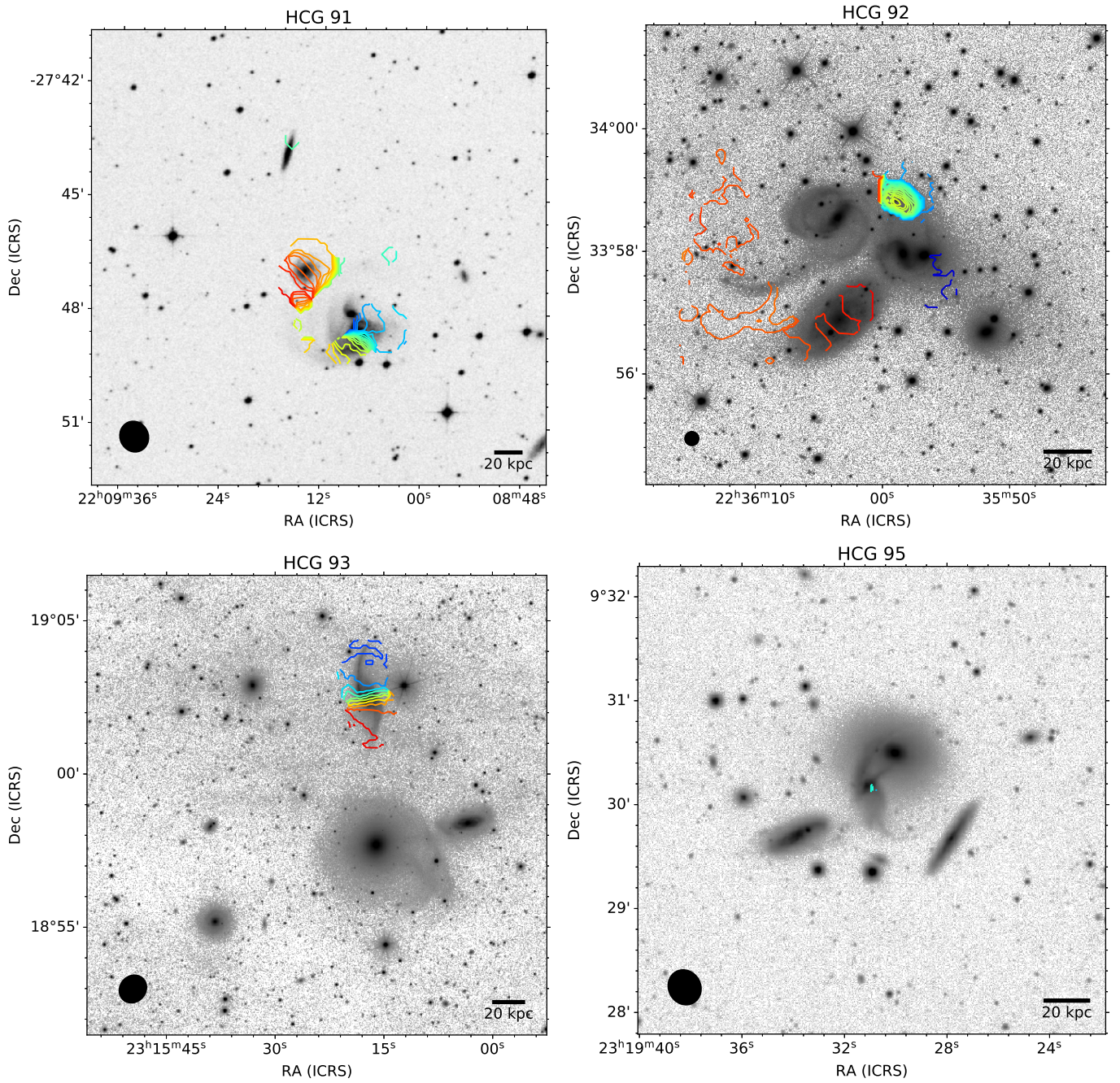


Figure D.1 continued.

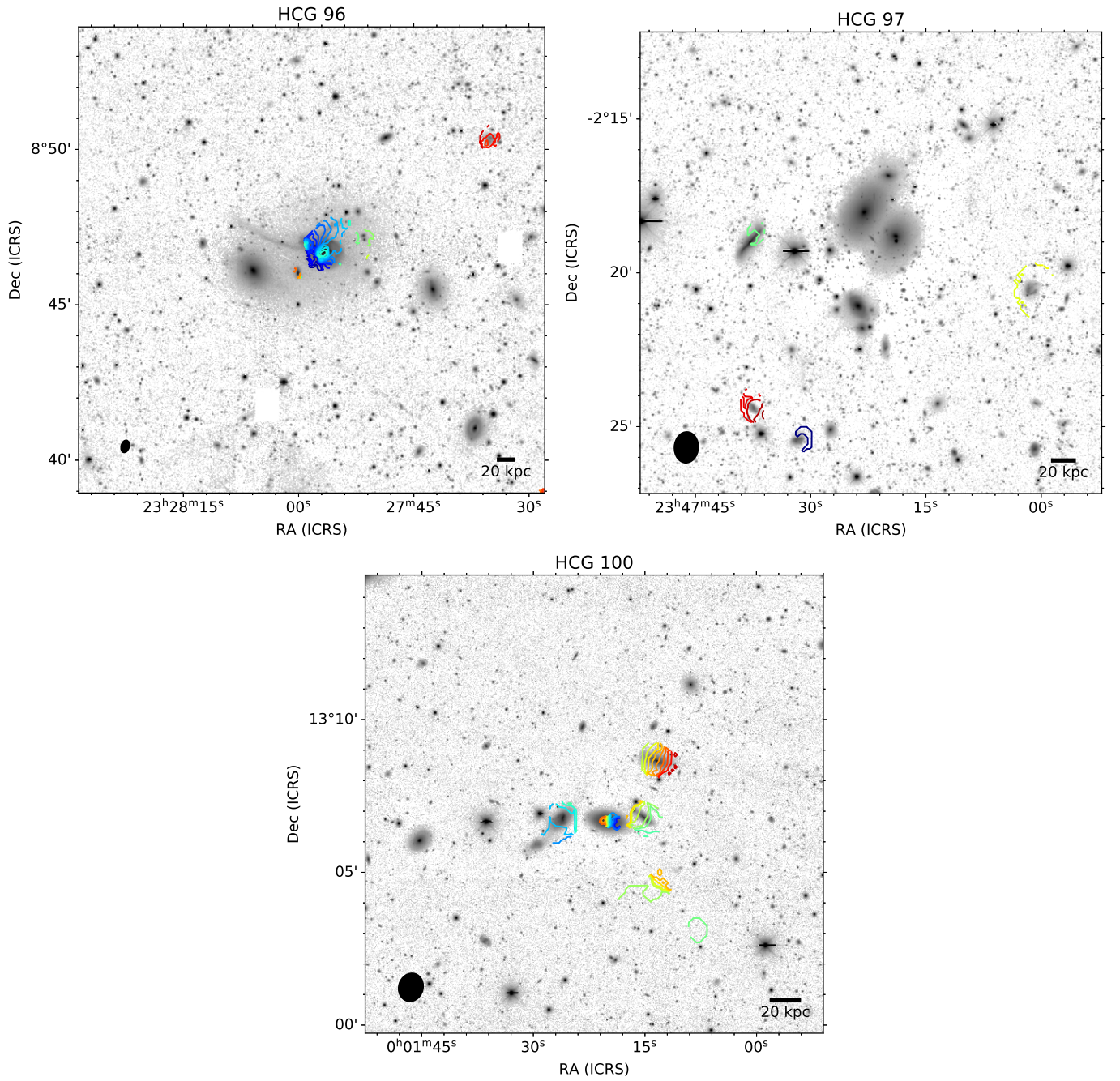


Figure D.1 continued.